

**Advances in modeling complex materials: The rise of neuroevolution potentials**

Penghua Ying,<sup>1,2, a)</sup> Cheng Qian,<sup>3, a)</sup> Rui Zhao,<sup>4, a)</sup> Yanzhou Wang,<sup>5</sup> Ke Xu,<sup>1</sup> Feng Ding,<sup>3</sup> Shunda Chen,<sup>6, b)</sup> and Zheyong Fan<sup>1, c)</sup>

<sup>1)</sup> *College of Physical Science and Technology, Bohai University, Jinzhou, P. R. China*

<sup>2)</sup> *Department of Physical Chemistry, School of Chemistry, Tel Aviv University, Tel Aviv, 6997801, Israel*

<sup>3)</sup> *Suzhou Laboratory, Suzhou, 215123, P. R. China*

<sup>4)</sup> *School of Mechanical and Electrical Engineering, Xinyu University, Xinyu, 338004, P. R. China*

<sup>5)</sup> *QTF Center of Excellence, Department of Applied Physics, Aalto University, FIN-00076 Aalto, Espoo, Finland*

<sup>6)</sup> *Department of Civil and Environmental Engineering, George Washington University, Washington, DC 20052, USA*

(Dated: 22 January 2025)

Interatomic potentials are essential for driving molecular dynamics (MD) simulations, directly impacting the reliability of predictions regarding the physical and chemical properties of materials. In recent years, machine-learned potentials (MLPs), trained against first-principles calculations, have become a new paradigm in materials modeling as they provide a desirable balance between accuracy and computational cost. The neuroevolution potential (NEP) approach, implemented in the open-source GPUMD software, has emerged as a promising machine-learned potential, exhibiting impressive accuracy and exceptional computational efficiency. This review provides a comprehensive discussion on the methodological and practical aspects of the NEP approach, along with a detailed comparison with other representative state-of-the-art MLP approaches in terms of training accuracy, property prediction, and computational efficiency. We also demonstrate the application of the NEP approach to perform accurate and efficient MD simulations, addressing complex challenges that traditional force fields typically can not tackle. Key examples include structural properties of liquid and amorphous materials, chemical order in complex alloy systems, phase transitions, surface reconstruction, material growth, primary radiation damage, fracture in two-dimensional materials, nanoscale tribology, and mechanical behavior of compositionally complex alloys under various mechanical loadings. This review concludes with a summary and perspectives on future extensions to further advance this rapidly evolving field.

**CONTENTS****I. Introduction**

2

**II. Overview of machine-learned potentials and the NEP approach**

4

- A. General introduction to machine-learned potentials (MLPs) 4
- B. Neuroevolution potential (NEP) approach 4
  - 1. Neural network model 4
  - 2. Descriptor vector 5
  - 3. Derived quantities 6
  - 4. Loss function 7
  - 5. Hyperparameters in the NEP approach 7
  - 6. Auxiliary tools and scripts for NEP models 8
  - 7. Case study: Constructing a NEP model for bilayer hexagonal boron nitride 8

**III. Performance and capability assessment of NEP and various representative MLPs**

8

- A. Representative MLPs for comparison: DP, GAP, MACE, NEP, and NequIP 8
- B. Performance evaluation 10
  - 1. Training accuracy 10
  - 2. Case study I: Binding and sliding energies in bilayer graphene 10
  - 3. Case study II: Bonding statistics in amorphous carbon 10
  - 4. Computational speed 11
- C. Summary 13

**IV. Structural properties**

13

- A. Structural properties of disordered carbon and liquid water 13
  - 1. Disordered carbon 14
  - 2. Liquid water 14
- B. Chemical order in complex alloy systems 16
  - 1. Chemical short-range order in GeSn alloys 16
  - 2. Compositionally complex alloys 18
- C. Summary 21

**V. Phase transitions and related processes**

21

<sup>a)</sup>These authors contributed equally to this work.

<sup>b)</sup>Electronic mail: [phychensd@gmail.com](mailto:phychensd@gmail.com)

<sup>c)</sup>Electronic mail: [brucenju@gmail.com](mailto:brucenju@gmail.com)

A. Phase transitions of materials	21
B. Case study: Surface reconstruction	23
C. Case study: Theory-guided synthesis and growth of materials	24
D. Primary radiation damage	26
E. Summary	27
<b>VI. Mechanical properties</b>	27
A. Mechanical properties of 2D materials	27
B. Case study: Nanoscale tribology	28
C. Case study: Mechanical properties of compositionally complex alloys	29
1. Uniaxial compression	30
2. Impact compression	30
3. Uniaxial fatigue	31
D. Summary	31
<b>VII. Summary and Perspectives</b>	32
<b>Acknowledgments</b>	33
<b>Declaration of Conflict of Interest</b>	33
<b>References</b>	33

## I. INTRODUCTION

With the continuous advancement of computational methods and the growing computational power of modern computers, particularly graphics processing units (GPUs), computer simulations are playing an increasingly important role in studying the physical and chemical properties of complex materials. Among the various computational methods, atomistic simulations are of particular importance. Molecular dynamics (MD) and Monte Carlo (MC) simulations, and their hybrid ones, are among the most popular atomistic simulation methods, because they can describe physical and chemical processes at atomic resolution with detailed time-evolution information.

A crucial input to MD simulation is the interatomic potential for the system under consideration. Empirical potentials (also known as force fields to emphasize the determined parameters) for various materials have been extensively developed over the past decades,<sup>1</sup> including the Lenard-Jones potential, the embedded-atom method potential,<sup>2,3</sup> the Stillinger-Weber potential<sup>4</sup>, the Tersoff potential,<sup>5</sup> the reactive empirical bond order potential<sup>6</sup>, and the ReaxFF potential.<sup>7</sup> These potentials rely on physically and chemically inspired mathematical functions, which are relatively fast to evaluate but are generally not accurate enough. On the other hand, MD simulations driven by quantum-mechanical calculations such as density-functional theory (DFT), known as *ab initio* MD simulations, essentially do not rely on empirical parameters and have played an important role in materials calculations. A downside of the *ab initio* MD approach

is its high-order scaling of computational cost with respect to the system size. Therefore, there is a dilemma between speed and accuracy: MD simulations based on conventional empirical potentials are fast but usually not accurate, while *ab initio* MD is more accurate but typically too expensive.

In recent years, modern machine-learned potentials (MLPs), especially high-dimensional neural networks potentials first introduced by Behler and Parrinello,<sup>8</sup> trained on first-principles calculations, have provided a desirable balance between accuracy and computational cost. As a result, MLP-driven MD simulations have emerged as a new paradigm in the reliable modeling of the structural, thermal, and mechanical properties of various solids and liquids, especially those involving complex reactive dynamics. The high computational accuracy of MLPs is further enhanced by advanced atom-environment descriptors and flexible machine-learning frameworks, which are free from the limitations of restricted mathematical forms and the limited number of fitting parameters in traditional empirical potentials. Importantly, while MLPs are usually trained against abundant quantum-mechanical data, their evaluation is of orders of magnitude faster than quantum-mechanical calculations, making MLP-based MD simulations powerful tools.

With ongoing advancements in the field, there is an increasing need for an updated review of the existing literature covering practical aspects. Our aim with this review is to offer researchers valuable insights into state-of-the-art methodologies that can significantly enhance the accuracy and efficiency of MD simulations, particularly for studies on structural properties and mechanical behavior. To accomplish this goal, we will use the promising machine-learned neuroevolution potential (NEP) method,<sup>9</sup> implemented in the open-source GPUMD software,<sup>10</sup> as a representative approach. This framework will serve as a basis for discussing recent progress and, more importantly, best practices in the development and application of MLP models. We will demonstrate how the developed MLPs can be effectively applied to perform accurate and efficient MD simulations to address complex problems typically beyond the scope of MD simulations based on traditional force fields as well as *ab initio* MD simulations.

This review is not a comprehensive survey of all MLP approaches. We refer readers to recent reviews on some other popular MLP approaches.<sup>47–58</sup> Even for the NEP approach, this article does not attempt to cover all the existing applications enabled by this approach. In particular, the NEP approach has been extensively used in thermal transport studies, and this topic has been thoroughly reviewed recently.<sup>59</sup> Extensions of the NEP approach to tensorial properties<sup>60</sup> such as electric dipole and polarizability are also out of the scope of this review. Instead, this review focuses on applications of NEP approach to understand the structural and mechanical properties of complex materials. Notably, this review article not only

TABLE I. Applications of the neuroevolution potential approach for investigating structural properties and mechanical behavior of materials, up to January 17, 2025.

Year	Reference	Material(s)	Processes and properties
2023	Fransson <sup>11</sup>	CsPbBr <sub>3</sub>	Phase transition
2023	Fransson <sup>12</sup>	CsPbBr <sub>3</sub> and MAPbI <sub>3</sub>	Phase transition
2023	Fransson <sup>13</sup>	CsPbX <sub>3</sub> (X = Cl, Br, and I)	Phase transition
2023	Li <sup>14</sup>	Carbon systems	Structural properties, phase transition
2023	Liu <sup>15</sup>	Tungsten	Primary radiation damage
2023	Shi <sup>16</sup>	Diamond	Shock compression, phase transition
2023	Shi <sup>17</sup>	InGeX <sub>3</sub> (X = S, Se and Te)	Mechanical properties
2023	Shi <sup>18</sup>	CsPbCl <sub>3</sub> and CsPbBr <sub>3</sub>	Phase transition, mechanical properties
2023	Wang <sup>19</sup>	Amorphous Si	Phase transition, short- and medium-range orders
2023	Wiktor <sup>20</sup>	CsMX <sub>3</sub> (M = S, Pb and X = Cl, Br, I)	Short-range order, phase transition
2023	Ying <sup>21</sup>	Quasi-hexagonal-phase fullerene	Mechanical properties
2023	Zhao <sup>22</sup>	Pd-Cu-Ni-P alloys	Glass transition, short range order, mechanical properties
2024	Chen <sup>23</sup>	GeSn alloy	Chemical short-range order
2024	Fransson <sup>24</sup>	MAPbI <sub>3</sub>	Phase transition
2024	Huang <sup>25</sup>	Carbon Kagome lattice	Phase transition, ductility
2024	Huang <sup>26</sup>	Mg <sub>3</sub> (Sb, Bi) <sub>2</sub>	Segregation, chemical order
2024	Li <sup>27</sup>	Sb-Te phase change materials	Phase transition, crystallization
2024	Liu <sup>28</sup>	High-entropy ceramics	Mechanical properties
2024	Lyu <sup>29</sup>	PbSeTeS	Local chemical order
2024	Pan <sup>30</sup>	Silica	Shock compression, phase transition
2024	Qi <sup>31</sup>	AlN/Diamond heterostructures	Mechanical properties
2024	Ru <sup>32</sup>	2D heterostructures	Interlayer friction
2024	Song <sup>33</sup>	Compositionally complex alloys	Chemical order, phase transition, mechanical properties
2024	Timalsina <sup>34</sup>	High-entropy oxide	Mechanical properties
2024	Wang <sup>35</sup>	Covalent organic frameworks	Thermoelastic properties
2024	Yu <sup>36</sup>	Hexagonal boron nitride	Mechanical properties
2024	Yu <sup>37</sup>	Janus graphene	Phase transition
2024	Zhao <sup>38</sup>	Ti-Al-Nb alloys	Elastic and mechanical properties
2025	Liu <sup>39</sup>	BN	Phase transition, crystallization, mechanical properties
Preprint	Ahlawat <sup>40</sup>	CsPbI <sub>3</sub>	Phase transition
Preprint	Liu <sup>41</sup>	Si-Ge-Sn alloys	Chemical short-range order
Preprint	Liu <sup>42</sup>	Mo-Nb-Ta-V-W alloy	Primary radiation damage
Preprint	Song <sup>43</sup>	Many binary alloys	Segregation, chemical order, mechanical properties
Preprint	Wang <sup>44</sup>	Porous and amorphous carbon	Phase transition, structural properties
Preprint	Xu <sup>45</sup>	Liquid water	Structural properties
Preprint	Zhang <sup>46</sup>	Aluminas (Aluminum oxides)	Structural properties, phase transition

reviews existing results in literature but also introduces new case studies and findings. Particularly, we have developed several new NEP models in this work, which were employed to generate fresh results and gain insights.

Table I provides a comprehensive list of publications employing the NEP approach for studying structural properties and mechanical behavior of materials, up to January 17, 2025. These applications cover a wide range of structural and mechanical phenomena, processes and properties, including structural order and disorder, segre-

gation, chemical order, elastic properties, ductility, fracture dynamics, friction, phase transition, shock compression, radiation damage, crystallization, material growth, and so on. While these processes and properties often overlap and are interconnected, for the sake of clarity, we categorize them into three main themes: structural properties, phase transition and material growth, and mechanical properties. This categorization is also reflected in the structure of this review article, which we briefly introduce below.

This article is organized as follows: In Sec. II, we review the general concepts and principles of MLPs (Sec. II A) and the mathematical formalism of the NEP approach.<sup>9,33,61,62</sup> (Sec. II B) This is followed by Sec. III for a detailed performance evaluation of the NEP approach compared to a few other state-of-the-art MLP approaches, including Gaussian approximation potential (GAP),<sup>63</sup> deep potential (DP),<sup>64</sup> neural equivariant interatomic potential (NequIP),<sup>65</sup> and MACE,<sup>66</sup> using a public carbon dataset that has been used to construct a general-purpose GAP model for carbon systems.<sup>67</sup> The performance evaluation includes not only accuracy metrics in the training dataset, but also predictions for physical quantities and computational efficiency. Subsequent sections demonstrate example applications of the NEP approach in studying structural properties (Sec. IV), phase transition and related processes (Sec. V), and mechanical properties (Sec. VI). Finally, summary and perspectives are discussed in Sec. VII.

## II. OVERVIEW OF MACHINE-LEARNED POTENTIALS AND THE NEP APPROACH

### A. General introduction to machine-learned potentials (MLPs)

The overall framework of MLPs suitable for extended systems was first proposed by Behler and Parrinello in 2007,<sup>8</sup> known as high-dimensional neural network potential, or simply Behler-Parinello neural network potential. Here, “high-dimensional” refers to the capability of the neural network model to represent complex potential energy surfaces that depend on the positions of many atoms in a system. A crucial construction to achieve this is to express the total potential energy  $U$  of an  $N$ -atom system as the sum of the individual site energies of the atoms  $U_i$ ,  $U = \sum_i^N U_i$ . The site energy of an atom is totally determined by its local chemical environment.

Mathematically, the local chemical environment of an atom  $i$  is expressed as a set of functions that are invariant with respect to a set of symmetry operations, including translation and rotation of the system, and permutation of atoms of the same kind in the system. These functions are referred to as atom-centered symmetry functions<sup>8,68</sup> in the Behler-Parinello approach. More generally, they are known as features or descriptors for a neural network potential. The descriptors constitute an abstract vector  $\mathbf{q}$ , known as the descriptor vector, which serves as the input layer of the neural network. The neural network model itself represents a (typically nonlinear) function  $\mathcal{N}$  of the input descriptor vector, which can be expressed as  $U_i = \mathcal{N}(\mathbf{q}^i)$  for a given atom  $i$ . The function  $\mathcal{N}$  is universal for all the atoms in a system, but could be dependent on the species of the atom  $i$ . We will discuss this dependence in the context of the NEP approach.

Later developments have introduced various descriptors  $\mathbf{q}$  and regression models  $\mathcal{N}$ . Regarding de-

scriptors, several systematically improvable approaches were proposed in more recent MLPs, including the GAP<sup>63</sup> based on smooth overlap of atomic positions,<sup>69,70</sup> the spectral neighbor analysis potential,<sup>71</sup> the moment tensor potential,<sup>72</sup> and the atomic cluster expansion approach.<sup>73</sup> In these approaches, the completeness of the descriptors can be systematically improved by tuning hyperparameters such as  $n_{\max}$  (related to radial space) and  $l_{\max}$  (related to angular space), or similar ones. Descriptors can also be constructed using deep learning techniques from simple geometric inputs, as demonstrated by the DP method.<sup>64</sup> All these descriptors can be regarded as atom-centered descriptors, which are constructed based on the neighboring atoms within a cutoff radius around the central atom. Recent developments to extend the interaction range include the fourth-generation of the neural network potential<sup>74</sup> and methods involving message passing, such as SchNet,<sup>75</sup> recursively embedded atom neural network potential,<sup>76</sup> NequIP,<sup>65</sup> MACE,<sup>66</sup> high-order tensor message passing interatomic potential,<sup>77</sup> Cartesian atomic cluster expansion potential,<sup>78</sup> and graph atomic cluster expansion potential.<sup>79</sup> For a more comprehensive review on the descriptors used in MLPs, we refer readers to previous review papers.<sup>80,81</sup>

Regarding the regression models  $\mathcal{N}$ , most current MLPs adopt neural networks, while some approaches prefer alternatives such as linear regression<sup>71,72</sup> or Gaussian regression.<sup>63</sup> For more detailed discussions on the regression models used in constructing MLPs, we refer readers to previous review papers.<sup>47,48,50–58</sup>

### B. Neuroevolution potential (NEP) approach

#### 1. Neural network model

The MLP we focus on reviewing was introduced in 2021,<sup>9</sup> and it is called NEP. This method has undergone several refinements,<sup>33,61,62</sup> and we will focus on the latest versions, NEP3<sup>62</sup> and NEP4.<sup>33</sup> A distinguishing feature of NEP is its training algorithm, which utilizes a separable natural evolution strategy.<sup>82</sup> The term “neuroevolution” reflects the combination of the neural network model and the evolutionary training algorithm. The machine-learning model used in NEP is a feed-forward neural network with a single hidden layer. In terms of the neural network model, the site energy can be explicitly expressed as:

$$U_i = \sum_{\mu=1}^{N_{\text{neu}}} w_{\mu}^{(1)} \tanh \left( \sum_{\nu=1}^{N_{\text{des}}} w_{\mu\nu}^{(0)} q_{\nu}^i - b_{\mu}^{(0)} \right) - b^{(1)}, \quad (1)$$

where  $\tanh(x)$  is the activation function,  $w^{(0)}$  are the weight parameters connecting the input layer (with dimension  $N_{\text{des}}$ ) and the hidden layer (with dimension  $N_{\text{neu}}$ ),  $w^{(1)}$  represents the weight parameters connecting



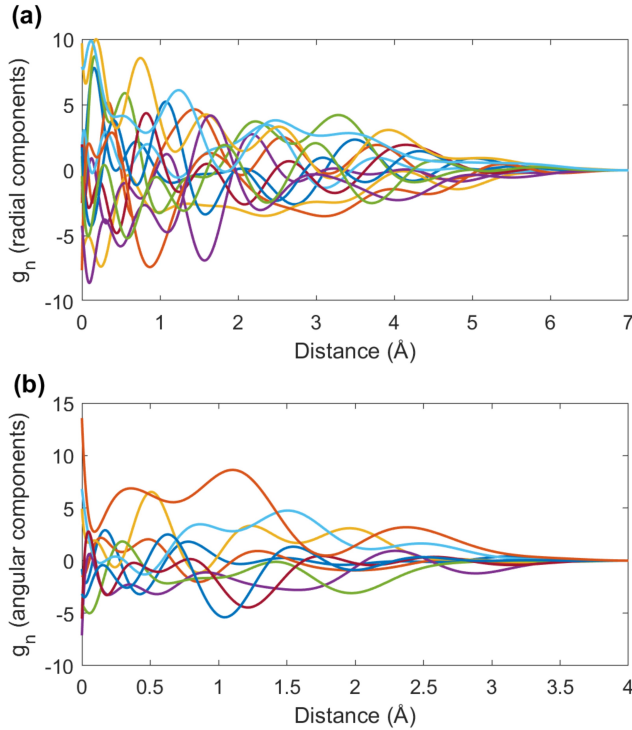


FIG. 1. Illustration of the radial functions in the neuroevolution potential (NEP) approach. The radial functions  $g_n(r_{ij})$  as a function of the atom-pair distance  $r_{ij}$  for (a) the radial descriptor components (cutoff radius: 7 Å) and (b) the angular descriptor components (cutoff radius: 4 Å) in the carbon NEP model as used in Sec. III.

the hidden layer and the output layer (the site energy),  $b^{(0)}$  represent the bias parameters in the hidden layer, and  $b^{(1)}$  is the bias parameter in the output layer. All these parameters are trainable.

## 2. Descriptor vector

The input layer corresponds to the descriptor vector  $\mathbf{q}^i$  (of dimension  $N_{\text{des}}$ ) for a given atom  $i$ , with its components denoted as  $q_\nu^i$  in Eq. (1). Similar to the symmetry functions in the Behler-Parrinello approach,<sup>8,68</sup> the descriptor components in NEP are classified into radial and angular ones.

As the name suggests, radial descriptor components depend solely on radial distances  $r_{ij}$ . To ensure permutation invariance, a radial descriptor is constructed as a sum over neighboring atoms:

$$q_n^i = \sum_{j \neq i} g_n(r_{ij}), \quad (2)$$

where  $g_n(r_{ij})$  is a specific function of the distance  $r_{ij}$  between atoms  $i$  and  $j$ . The radial descriptor components are labeled by the index  $n$ , which can take on  $n_{\text{max}}^{\text{R}} + 1$  values, ranging from 0 to  $n_{\text{max}}^{\text{R}}$ .

For the radial functions  $g_n(r_{ij})$ , Behler and Parrinello devised a set of Gaussian functions with different centers and widths.<sup>8,68</sup> In NEP, each radial function is a linear combination of a number of basis functions:

$$g_n(r_{ij}) = \sum_{k=0}^{N_{\text{bas}}^{\text{R}}} c_{nk}^{IJ} f_k(r_{ij}), \quad (3)$$

Here the basis functions are indexed by  $k$ , which can take on  $N_{\text{bas}}^{\text{R}} + 1$  values, ranging from 0 to  $N_{\text{bas}}^{\text{R}}$ . The basis function  $f_k(r_{ij})$  is chosen to be the following form:<sup>62</sup>

$$f_k(r_{ij}) = \frac{1}{2} \left[ T_k \left( 2 \left( r_{ij}/r_c^{\text{R}} - 1 \right)^2 - 1 \right) + 1 \right] f_c(r_{ij}),$$

where  $T_k(x)$  is the  $k$ -th order Chebyshev polynomial of the first kind. The function  $f_c(r_{ij})$  is a smoothing function defined as

$$f_c(r_{ij}) = \begin{cases} \frac{1}{2} \left[ 1 + \cos \left( \pi \frac{r_{ij}}{r_c^{\text{R}}} \right) \right] & r_{ij} \leq r_c^{\text{R}} \\ 0 & r_{ij} > r_c^{\text{R}}. \end{cases}$$

where  $r_c^{\text{R}}$  is a cutoff radius beyond which the basis functions are zero. Due to the use of a smoothing function, the summation over  $j$  in Eq. (2) is not for all the atoms in a system, but only those within a distance of  $r_c^{\text{R}}$  from the central atom  $i$ . The argument  $x = 2 \left( r_{ij}/r_c^{\text{R}} - 1 \right)^2 - 1$  for the Chebyshev polynomials takes values from  $-1$  (when  $r_{ij} = r_c^{\text{R}}$ ) to approaching  $1$  (when  $r_{ij} = 0$ , which should never happen), as required by the definition of Chebyshev polynomials.

The expansion coefficients  $c_{nk}^{IJ}$  in Eq. (3) depend on both the type  $I$  of the central atom  $i$  and the type  $J$  of the neighboring atom  $j$ . Moreover, these coefficients are trainable parameters, similar to the weight and bias parameters in the neural network. This construction maintains invariance with respect to exchanging atom pairs of the same kind while providing a mechanism for distinguishing different atom types (species). Most importantly, the computational performance of a NEP model is nearly independent of the number of species in the system. In other words, a NEP model trained for the entire periodic table is nearly as fast as a NEP model for a single element.

Figure 1(a) shows the radial functions  $g_n(r_{ij})$  in the radial descriptor components for the carbon NEP model, as used in Sec. III. The relevant hyperparameters are  $n_{\text{max}}^{\text{R}} = 12$ ,  $N_{\text{bas}}^{\text{R}} = 16$ , and  $r_c^{\text{R}} = 7$  Å. We observe that in NEP, the radial functions are not handcrafted but are instead learned automatically based on specific training data.

In contrast to the radial descriptor components, the angular components depend not only on the radial distances  $r_{ij}$ , but also on angles such as  $\theta_{ijk}$  formed by the  $\mathbf{r}_{ij}$  and  $\mathbf{r}_{ik}$  vectors,

$$\cos \theta_{ijk} = \frac{\mathbf{r}_{ij} \cdot \mathbf{r}_{ik}}{r_{ij} r_{ik}}.$$

Here and elsewhere, we define  $\mathbf{r}_{ij} \equiv \mathbf{r}_j - \mathbf{r}_i$ . The simplest angular descriptor components are the so-called three-body ones, which are expressed in terms of the Legendre polynomials  $P_l(x)$  in NEP:

$$q_{nl}^i = \frac{2l+1}{4\pi} \sum_{j \neq i} \sum_{k \neq i} g_n(r_{ij}) g_n(r_{ik}) P_l(\cos \theta_{ijk}). \quad (4)$$

Here, each three-body angular descriptor component is labeled by two indices,  $n$ , and  $l$ , where  $n$  takes on  $n_{\max}^A + 1$  values ranging from 0 to  $n_{\max}^A$ , and  $l$  takes on  $l_{\max}$  values ranging from 1 to  $l_{\max}$ . Therefore, there are  $(n_{\max}^A + 1)l_{\max}$  three-body angular descriptor components. The definition of the angular descriptor components also involves the radial functions, which are defined similarly to Eq. (3), but with a potentially different cutoff radius  $r_c^A$  and expansion order  $N_{\text{bas}}^A$ . Due to the use of a smoothing function, the summations over  $j$  and  $k$  in Eq. (4) are not for all the atoms in a system, but the atoms that are within a distance of  $r_c^A$  from the central atom  $i$ .

Figure 1(b) shows the radial functions  $g_n(r_{ij})$  in the angular descriptor components for the carbon NEP model, as used in Sec. III. The relevant hyperparameters are  $n_{\max}^A = 8$ ,  $N_{\text{bas}}^A = 12$ , and  $r_c^A = 4 \text{ \AA}$ . Again, these radial functions are not handcrafted but are instead learned automatically based on specific training data.

A direct implementation of Eq. (4) involves double summation over neighboring atoms, which scales quadratically with respect to the average number of neighbors. This is also the case for the angular descriptor components in the Behler-Parrinello approach.<sup>8,68</sup> The computational complexity can be reduced by using the addition theorem of spherical harmonics  $Y_{lm}(\theta_{ij}, \phi_{ij})$ , transforming Eq. (4) into a mathematically equivalent form:

$$q_{nl}^i = \sum_{m=-l}^l (-1)^m A_{nlm}^i A_{nl(-m)}^i,$$

where

$$A_{nlm}^i = \sum_{j \neq i} g_n(r_{ij}) Y_{lm}(\theta_{ij}, \phi_{ij}).$$

Using the relation for the spherical harmonics,

$$Y_{l(-m)}(\theta_{ij}, \phi_{ij}) = (-1)^m Y_{lm}^*(\theta_{ij}, \phi_{ij}),$$

we have

$$A_{nl(-m)}^i = (-1)^m (A_{nlm}^i)^*.$$

Therefore, we can express the three-body angular descriptor components as

$$q_{nl}^i = \sum_{m=0}^l (2 - \delta_{0m}) |A_{nlm}^i|^2,$$

which are clearly real-valued. Here,  $\delta_{m0}$  is the Kronecker  $\delta$  symbol, which is 1 for  $m = 0$  and 0 for all other values of  $m$ . The expression  $A_{nlm}^i$  is the basic ingredient for building higher-order angular descriptor components within the atomic cluster expansion formalism.<sup>73</sup> In NEP, there are  $n_{\max}^A + 1$  four-body and  $n_{\max}^A + 1$  five-body angular descriptor components; explicit expressions can be found in previous work.<sup>62</sup>

Returning to the neural network model of NEP, we previously discussed that the site energy can be formally expressed as  $U_i = \mathcal{N}(\mathbf{q}^i)$ . To emphasize the dependence of the model on the various trainable parameters, we can express the site energy as  $U_i = \mathcal{N}(\mathbf{w}^I; \mathbf{q}^i(\{\mathbf{c}^{IJ}\}))$ , where the neural network parameters are collectively denoted as  $\mathbf{w}$ , and the expansion coefficient parameters as  $\mathbf{c}$ . The superscript  $I$  in  $\mathbf{w}^I$  indicates that each species has a distinct set of neural network parameters, while the superscript  $IJ$  in  $\mathbf{c}^{IJ}$  indicates that each pair of species has a distinct set of expansion coefficient parameters.

### 3. Derived quantities

Starting from the site energy  $U_i$  as the output of the neural network, we can derive the other microscopic quantities, such as force, virial, and heat current. NEP is a many-body potential, and general expressions for these quantities have been discussed for general many-body potentials.<sup>83</sup> A crucial result is that Newton's third law (the weak form in general) still applies for many-body potentials. That is, the force on atom  $i$ ,  $\mathbf{F}_i$ , can be expressed as a summation,  $\mathbf{F}_i = \sum_{j \neq i} \mathbf{F}_{ij}$ , where  $\mathbf{F}_{ij}$  is the force acting on atom  $i$  due to atom  $j$ , which is opposite to the force acting on atom  $j$  due to atom  $i$ ,  $\mathbf{F}_{ij} = -\mathbf{F}_{ji}$ . The "pairwise" force  $\mathbf{F}_{ij}$  has a simple expression:<sup>83</sup>

$$\mathbf{F}_{ij} = \frac{\partial U_i}{\partial \mathbf{r}_{ij}} - \frac{\partial U_j}{\partial \mathbf{r}_{ji}},$$

where  $\partial U_i / \partial \mathbf{r}_{ij}$  can be understood as a "partial force". In terms of the descriptor vector, the partial force can be written as

$$\frac{\partial U_i}{\partial \mathbf{r}_{ij}} = \sum_{\nu=1}^{N_{\text{des}}} \frac{\partial U_i}{\partial q_{\nu}^i} \frac{\partial q_{\nu}^i}{\partial \mathbf{r}_{ij}}.$$

Further derivations are straightforward based on the expressions of the descriptor components discussed above. In terms of the partial force, the per-atom virial  $\mathbf{W}_i$  can be expressed as

$$\mathbf{W}_i = \sum_{j \neq i} \mathbf{r}_{ij} \otimes \frac{\partial U_j}{\partial \mathbf{r}_{ji}}.$$

The total virial of a system is the sum of the per-atom virials  $\mathbf{W} = \sum_i \mathbf{W}_i$ . Moreover, the potential part of the heat current can be conveniently expressed in term of this particular form of virial:

$$\mathbf{J}^{\text{pot}} = \sum_i \mathbf{W}_i \cdot \mathbf{v}_i,$$

where  $\mathbf{v}_i$  is the velocity of atom  $i$ . Although thermal properties, including heat transport, are interesting topics, they are not the focus of the present review. For a review on the applications of MLPs in MD simulations of heat transport, readers are referred to the work by Dong *et al.*<sup>59</sup>

#### 4. Loss function

For any MLP, there are a number of hyper-parameters and a number of trainable parameters. The number of trainable parameters is determined by the values of the hyper-parameters. For NEP, there are two sets of trainable parameters, the weight and bias parameters in the neural network model [Eq. (1)], and the expansion coefficients for the radial functions [Eq. (3)]. The relevant hyper-parameters include  $N_{\text{neu}}$ ,  $n_{\text{max}}^{\text{R}}$ ,  $n_{\text{max}}^{\text{A}}$ ,  $N_{\text{bas}}^{\text{R}}$ ,  $N_{\text{bas}}^{\text{A}}$ ,  $l_{\text{max}}$ , and the number of atom types  $N_{\text{typ}}$ . If both four-body and five-body angular descriptor components are considered, the dimension of the descriptor vector is

$$N_{\text{des}} = (n_{\text{max}}^{\text{R}} + 1) + (l_{\text{max}} + 2)(n_{\text{max}}^{\text{A}} + 1).$$

Then the number of weight and bias parameters is  $(N_{\text{des}} + 2)N_{\text{neu}} + 1$  in NEP3<sup>62</sup> and  $N_{\text{typ}}(N_{\text{des}} + 2)N_{\text{neu}} + 1$  in NEP4.<sup>33</sup> According to Eq. (3), the number of expansion coefficients for the radial descriptor components is  $N_{\text{typ}}^2(n_{\text{max}}^{\text{R}} + 1)(N_{\text{bas}}^{\text{R}} + 1)$ . Similarly, the number of expansion coefficients for the angular descriptor components is  $N_{\text{typ}}^2(n_{\text{max}}^{\text{A}} + 1)(N_{\text{bas}}^{\text{A}} + 1)$ . The total number of trainable parameters  $N_{\text{par}}$  is the sum of the above three numbers.

The training for a NEP model refers to the optimization of the  $N_{\text{par}}$  parameters, which form an abstract vector  $\mathbf{z}$ . The optimization is guided by a loss function, which is to be minimized. The loss function is defined as a weighted sum of the root-mean-square error (RMSE) values for energy, force, and virial, along with regularization terms:

$$L(\mathbf{z}) = L_e(\mathbf{z}) + L_f(\mathbf{z}) + L_v(\mathbf{z}) + L_1(\mathbf{z}) + L_2(\mathbf{z}).$$

Here,  $L_e(\mathbf{z})$  is the multiplication of a weight  $\lambda_e$  and the energy RMSE,  $L_f(\mathbf{z})$  is the multiplication of a weight  $\lambda_f$  and the force RMSE, and  $L_v(\mathbf{z})$  is the multiplication of a weight  $\lambda_v$  and the virial RMSE. To prevent overfitting, both  $\mathcal{L}_1$  regularization and  $\mathcal{L}_2$  regularization are considered, with the following explicit expressions for the loss terms:

$$L_1(\mathbf{z}) = \lambda_1 \frac{1}{N_{\text{par}}} \sum_{n=1}^{N_{\text{par}}} |z_n|,$$

$$L_2(\mathbf{z}) = \lambda_2 \left( \frac{1}{N_{\text{par}}} \sum_{n=1}^{N_{\text{par}}} z_n^2 \right)^{1/2}.$$

The use of both  $\mathcal{L}_1$  regularization and  $\mathcal{L}_2$  regularization and the use of RMSE instead of mean-square error in the

loss function reflects a special property of the separable natural evolution strategy<sup>82</sup> used for training NEP models: it is a derivative-free black-box real-value optimizer.

#### 5. Hyperparameters in the NEP approach

For each NEP model, there are a number of hyper-parameters that need to be specified. In the graphics processing units molecular dynamics (GPUMD) package, these hyperparameters are specified in a text input file named `nep.in`. This file contains lines in the format of “keyword value(s)”. Using PbTe as an example, the frequently used keywords and default parameter values are listed below:

<code>type</code>	2 Pb Te	
<code>version</code>	4	# default
<code>cutoff</code>	8 4	# default
<code>n_max</code>	4 4	# default
<code>basis_size</code>	8 8	# default
<code>l_max</code>	4 2 0	# default
<code>neuron</code>	30	# default
<code>lambda_e</code>	1.0	# default
<code>lambda_f</code>	1.0	# default
<code>lambda_v</code>	0.1	# default
<code>batch</code>	1000	# default
<code>population</code>	50	# default
<code>generation</code>	100000	# default

The `type` keyword is followed by the number of atom types and the corresponding element names. The `version` keyword has a default value of 4, indicating the NEP4 version.<sup>33</sup> It can also take the value of 3, corresponding to the NEP3 version.<sup>62</sup> Older versions have not been widely used and have been deprecated. The `cutoff` keyword specifies the radial and angular cutoff radii,  $r_c^{\text{R}}$  and  $r_c^{\text{A}}$ , with default values of 8 Å and 4 Å, respectively. The `n_max` keyword specifies the  $n_{\text{max}}^{\text{R}}$  and  $n_{\text{max}}^{\text{A}}$  values, both with a default value of 4. The `basis_size` keyword specifies the  $N_{\text{bas}}^{\text{R}}$  and  $N_{\text{bas}}^{\text{A}}$  values, both with a default value of 8. The `l_max` keyword specifies the  $l_{\text{max}}$  values for the three-body, four-body, and five-body angular descriptor components, with default values of 4, 2, and 0, respectively. This means that four-body angular descriptor components are included by default, but five-body ones are not. The `neuron` keyword specifies the number of neurons  $N_{\text{neu}}$  in the hidden layer of the neural network model, with a default value of 30. The keywords `lambda_e`, `lambda_f`, and `lambda_v` specify the energy, force, and virial weights  $\lambda_e$ ,  $\lambda_f$ , and  $\lambda_v$  in the loss function, with default values of 1, 1, and 0.1, respectively. The keyword `batch` specifies the batch size (number of structures used for updating the trainable parameters across one step) for training, with a default value of 1000. The keyword `population` specifies the population size in the natural evolution strategy, with a default value of 50. The keyword `generation` specifies

the number of training generations (steps) in the natural evolution strategy, with a default value of  $10^5$ .

## 6. Auxiliary tools and scripts for NEP models

The NEP approach is implemented in the open-source GPUMD package.<sup>10</sup> A distinguishing feature of NEP is that both the training and inference are enabled within the GPUMD package. Additionally, the inference of NEP can be performed using the large-scale atomic/molecular massively parallel simulator (LAMMPS) package<sup>85</sup> and other Python-based packages. Table II lists auxiliary tools for constructing and evaluating NEP models.

The inference of NEP in GPUMD is based on GPU computing, which attains high performance in large systems. However, some calculations, such as MD simulations during active learning, do not require large-scale systems, and the GPU version of NEP may not effectively utilize the computational resources in a typical GPU. To this end, a CPU-based NEP calculator has been developed as released in the NEP\_CPU repository (Table II). This repository serves two major purposes. First, it provides an interface to the LAMMPS<sup>85</sup> package, enabling large-scale MD simulations using CPUs parallelized via message-passing interface. Second, it serves as an engine for several auxiliary Python-based tools (Table II), which integrate seamlessly with other useful Python-based packages such as the atomic simulation environment package.<sup>86</sup> These auxiliary Python-based tools support various active-learning workflows for constructing NEP models and facilitate model evaluation through high-throughput calculations of various physical properties, such as various energetics, elastic constants, phonon dispersions, etc.

In addition to these packages, the `tools` folder within the GPUMD package, contains a variety of useful scripts, particularly for generating datasets from quantum-mechanical calculation outputs.

## 7. Case study: Constructing a NEP model for bilayer hexagonal boron nitride

As an illustrative example, we construct a NEP model for bilayer hexagonal boron here, which will be used for studying interlayer friction in Sec. VI B.

To train a NEP model, one has to prepare a training dataset. A training dataset should have a sufficient diversity to fully covers the application scenarios. The structures (configurations) in the training dataset can be generated by many means. A common approach is to perform realistic MD simulations using relatively small cells. The MD simulations can be driven by ab initio methods, but in our case, it is computationally cheaper to drive the MD simulations using available empirical potentials. We used the reactive empirical bond order potential<sup>6</sup> for intralayer interactions and the interlayer potential<sup>87</sup> for

interlayer interactions, to perform sliding simulations of bilayer structures consisting of 64 atoms at temperatures of 300, 600, 900, and 1200 K. We sample a total of 200 structures from these MD simulations. Besides these, we also constructed approximately 800 eight-atom bilayer structures with varying interlayer spacings and in-plane shifts relative to the AA-stacking mode. We selected 90% structures to form the training dataset, and the remaining 10% structures were taken as the test dataset.

Reference values for energy, force, and virial were calculated using DFT calculations as implemented in the VASP package,<sup>88,89</sup> employing the Perdew-Burke-Ernzerhof<sup>90</sup> functional, with a plan-wave energy cutoff of 650 eV, and energy convergence threshold of  $10^{-7}$  eV, and a  $\Gamma$ -centered  $k$ -point grid with a density of  $0.2 \text{ \AA}^{-1}$ . The D3 dispersion correction with the Becke-Johnson damping<sup>91</sup> is also included.

We used the following inputs in the `nep.in` file:

```

type          2 B N
version       3
cutoff        6 4.5
n_max         8 8
basis_size    12 12
l_max         4 2 0
neuron        50
lambda_1      0.05
lambda_2      0.05
lambda_e      1.0
lambda_f      1.0
lambda_v      0.1
batch         10000
population    50
generation    300000

```

The parity plots for energy, force, and stress comparing NEP and DFT results are shown in Fig. 2, which demonstrates good correlation between the NEP predictions and the DFT reference results. To quantify the accuracy, we calculated the RMSE values for energy, force, and virial, which are  $0.4 \text{ meV atom}^{-1}$ ,  $23.8 \text{ meV \AA}^{-1}$ , and  $0.3 \text{ GPa}$  for the training dataset, and  $0.4 \text{ meV atom}^{-1}$ ,  $22.5 \text{ meV \AA}^{-1}$ , and  $0.3 \text{ GPa}$  for the test dataset. The comparable RMSE values between the training and test datasets indicate that there is no over-fitting. We also note that there are only about 900 structures and 18000 atoms in the training dataset, indicating the high data efficiency of the NEP approach.

## III. PERFORMANCE AND CAPABILITY ASSESSMENT OF NEP AND VARIOUS REPRESENTATIVE MLPs

### A. Representative MLPs for comparison: DP, GAP, MACE, NEP, and NequIP

Before delving into the various applications of the NEP approach, we benchmark its performance against several



TABLE II. Auxiliary C++ and Python tools for constructing and evaluating neuroevolution potential (NEP) models.

Package	Code repository
NEP_CPU	<a href="https://github.com/brucefan1983/NEP_CPU">https://github.com/brucefan1983/NEP_CPU</a>
calorine <sup>84</sup>	<a href="https://gitlab.com/materials-modeling/calorine">https://gitlab.com/materials-modeling/calorine</a>
GPUMD-Wizard	<a href="https://github.com/Jonsnow-willow/GPUMD-Wizard">https://github.com/Jonsnow-willow/GPUMD-Wizard</a>
mdapy	<a href="https://github.com/mushroomfire/mdapy">https://github.com/mushroomfire/mdapy</a>
NepTrainKit	<a href="https://github.com/aboys-cb/NepTrainKit">https://github.com/aboys-cb/NepTrainKit</a>
NEP_Active	<a href="https://github.com/psn417/NEP_Active">https://github.com/psn417/NEP_Active</a>
PyNEP	<a href="https://github.com/bigd4/PyNEP">https://github.com/bigd4/PyNEP</a>
somd	<a href="https://github.com/initqp/somd">https://github.com/initqp/somd</a>

TABLE III. The machine-learned potential (MLP) approaches benchmarked in this work, along with their respective machine-learning models, molecular dynamics (MD) engines, and code repositories. The MD engines include large-scale atomic/molecular massively parallel simulator (LAMMPS)<sup>85</sup> and graphics process units molecular dynamics (GPUMD).<sup>10</sup>

MLP	Machine-learning model	MD engine (version for benchmark)	Code repository
DP <sup>64</sup>	Neural network	LAMMPS (2 Aug 2023)	<a href="https://github.com/deepmodeling/deepmd-kit">https://github.com/deepmodeling/deepmd-kit</a>
GAP <sup>63</sup>	Gaussian process	LAMMPS (2 Aug 2023)	<a href="https://github.com/libAtoms/QUIP">https://github.com/libAtoms/QUIP</a>
MACE <sup>66</sup>	Neural network	LAMMPS (28 Mar 2023)	<a href="https://github.com/ACEsuit/mace">https://github.com/ACEsuit/mace</a>
NEP <sup>9</sup>	Neural network	GPUMD (18 Aug 2024, v3.9.5)	<a href="https://github.com/brucefan1983/GPUMD">https://github.com/brucefan1983/GPUMD</a>
NequIP <sup>65</sup>	Neural network	LAMMPS (29 Sep 2021)	<a href="https://github.com/mir-group/nequip">https://github.com/mir-group/nequip</a>

representative MLP methods, including GAP,<sup>63</sup> DP,<sup>64</sup> NequIP,<sup>65</sup> and MACE.<sup>66</sup> Among these, GAP and DP, like NEP, are based on local atom-centered descriptors, whereas NequIP and MACE employ message passing or graph neural network constructions. Table III lists the MD engines (including version numbers used for evaluating computational speed), machine-learning models, and code repositories for these MLP methods. These MLP methods are representative, and a systematic comparison of their computational accuracy and speed will provide valuable insights into the relative strengths and limitations of the NEP approach. Importantly, our evaluations include not only traditional metrics such as energy and force RMSEs, but also physical properties like the distribution of bond motifs.

To ensure consistency, we adopted a general-purpose dataset for carbon systems constructed by Rowe *et al.*<sup>67</sup> in our benchmark study. This dataset is highly diverse, encompassing structures for sp<sup>2</sup>-bonded crystals, sp<sup>3</sup>-bonded crystals, crystal surfaces, defective structures, amorphous phases, and liquid phases. It contains a total of 6088 structures and 400 275 atoms. The reference data (energy, force, and virial) are computed using the optB88-vdW DFT functional.

Among the five MLP approaches being compared, a GAP model<sup>67</sup> and a NEP model<sup>92</sup> have already been trained previously. Therefore, we use these pre-trained models directly. For the remaining three MLP approaches, we train models in this work, using the same training data.

For the NEP approach, the `nep.in` input script reads as follows:

```

type          1 C
version       4
cutoff        7 4
n_max         12 8
basis_size    16 12
l_max         4 2 1
neuron        100
lambda_1      0.0
lambda_f      1.0
lambda_v      0.1
batch         8000 # fullbatch
population    100
generation    500000

```

For the GAP approach, a mixture of two-body, three-body, and many-body descriptors are used, with a cutoff of 4.5 Å, 2.5 Å, and 4.5 Å, respectively. The number of sparse points for these parts are 15, 200, and 9000, respectively. For the many-body part,  $n_{\max} = 12$  and  $l_{\max} = 4$ . Apart from these, there is also an extra  $r^{-6}$  dispersion term extending to 10 Å.

For the DP approach, we used a hybrid descriptor consisting of a two-body type (`se_e2_a`) with a cutoff radius of 7 Å and a three-body type (`se_e3`) with a cutoff radius of 4 Å. The embedding nets of the two descriptor types are of sizes (25, 50, 100) and (20, 40, 80), respectively. The fitting net is of size (240, 240, 240). The training process lasts for approximately 1600 epochs, with a



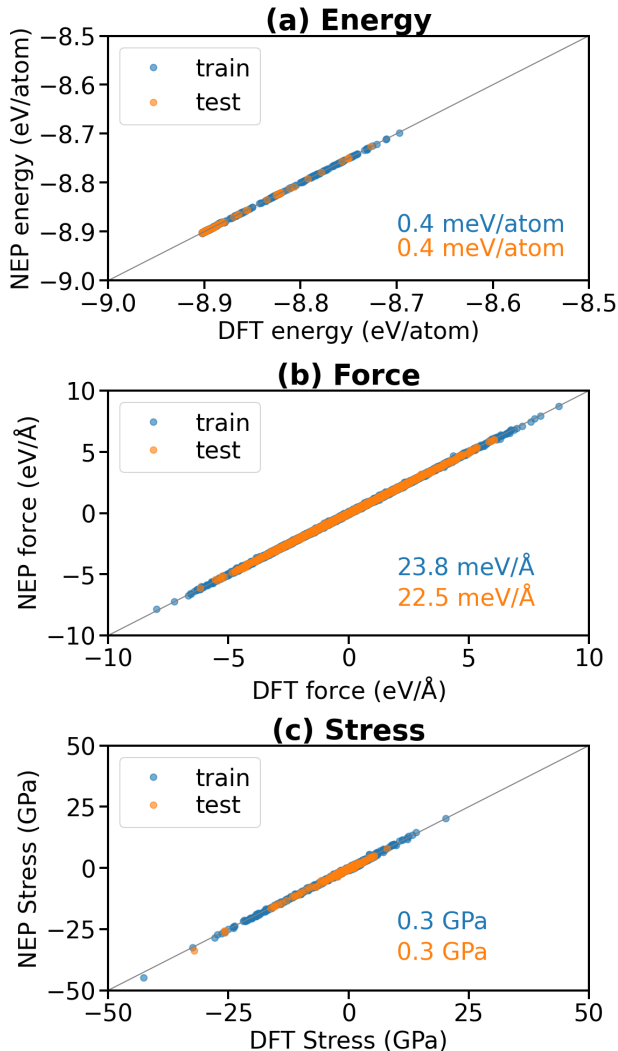


FIG. 2. Parity plots of (a) energy, (b) forces, and (c) stress comparing neuroevolution potential (NEP) predictions and density functional theory (DFT) reference data. The values in the subplots are root-mean-square errors for the training (blue) and test (orange) datasets.

starting learning rate of  $10^{-3}$  and final learning rate of  $10^{-8}$ . DeePMD-kit v2.1.5 was used for training.

For the NequIP approach, we used a total of 4 message passing layers, with a cutoff radius of 7 Å for each layer. The model includes 32 local features, 8 trainable Bessel basis functions and a maximum rotation order of  $l_{\max} = 1$ . The training process lasts for approximately 2500 epochs, with a learning rate of 0.005. NequIP v0.6.1 was used for training.

For the MACE approach, we used a total of 2 message passing layers, with a cutoff radius of 6 Å for each layer. The local features have 8 trainable Bessel basis functions and a correlation level of 3. The training process lasts for approximately 1500 epochs, with a learning rate of 0.01. MACE v0.3.6 was used for training.

## B. Performance evaluation

### 1. Training accuracy

Figure 3 presents the parity plots for all five MLPs using the full training dataset. Each subplot shows the RMSEs for energy, force, or virial, along with the relative errors. The relative error for a given quantity is defined as the ratio between the RMSE and the standard deviation of that quantity in the training dataset.

In addition, Fig. 4 compares the RMSEs across different types of structures within the dataset. It can be observed that MACE achieves the highest accuracy in energy, force, and virial for nearly all types of structures, while GAP typically exhibits the lowest accuracy. NEP and DP demonstrate comparable accuracy, outperforming GAP, but not as well as MACE. NequIP attains the second-highest accuracy for energy and force, but ranks second lowest for virial accuracy.

### 2. Case study I: Binding and sliding energies in bilayer graphene

Beyond RMSE metrics, we further benchmark each MLP for describing the physical properties of typical carbon systems. In Fig. 5 and Fig. 6, we evaluate the performance of the MLPs in describing the binding and sliding energies for bilayer graphene, comparing them to the DFT results obtained with optB88-vdW functional, which was used to generate the reference dataset.<sup>67</sup> None of the MLPs accurately locate the global minimum of the binding energy and the corresponding equilibrium interlayer spacing for AB-stacked bilayer graphene. While the NEP model significantly overestimates the equilibrium interlayer spacing, it is the only MLP model that produces a binding energy curve with a single minimum. In contrast, all other MLP models exhibit double minima in the binding energy curve. The inability of the GAP model to correctly describe the binding energy has also been observed in previous studies.<sup>93,94</sup> For the sliding case, the DP and GAP models fail to reproduce the sliding energy landscape even qualitatively, and the MACE model significantly overestimates the sliding energy corrugation. In contrast, the NEP and NequIP models show reasonable agreement with the DFT results.

### 3. Case study II: Bonding statistics in amorphous carbon

Next, we go beyond static energetics to explore the crystal-to-amorphous transition using MD simulations. For NEP, the GPUMD package<sup>10</sup> is used; for the other MLPs, the LAMMPS package<sup>85</sup> is used.

As shown in Fig. 7, a well-established melt-quench-anneal protocol<sup>44,62</sup> was used to generate amorphous car-

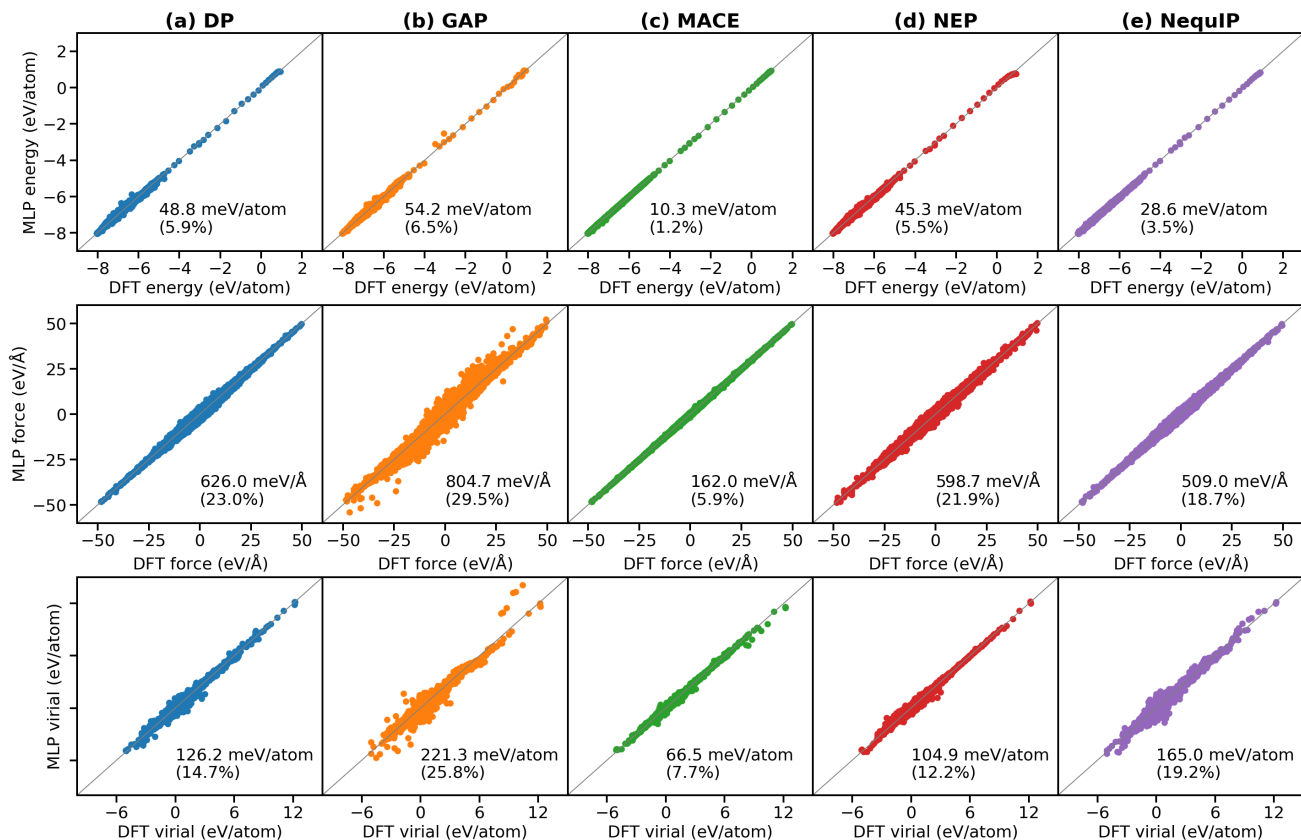


FIG. 3. Energies (top), forces (middle), and virials (bottom) from different machine-learned potential models (including DP,<sup>64</sup> GAP,<sup>63</sup> MACE,<sup>66</sup> NEP,<sup>9</sup> and NequIP<sup>65</sup>) against the target density-functional theory (DFT) values for the training dataset for carbon.<sup>67</sup> The root-mean-square error and relative error for each model are indicated in the respective subplot. The GAP model is from Ref. 67 and the NEP model is from Ref. 92. All other models were trained in the present work.

bon, starting from a 2744-atom diamond structure with a density of  $3.0 \text{ g cm}^{-3}$ . The system undergoes an initial rapid melting process at 9000 K for 30 ps, followed by a relaxation at 5000 K for another 30 ps. This is followed by a rapid quenching from 5000 K down to 1000 K in 0.5 ps, with further relaxation stages at 1000 K for 30 ps and subsequently at 300 K for 30 ps. Temperature control throughout these stages is achieved by using a Langevin thermostat,<sup>99</sup> with a time parameter of 100 fs. The time step for integration is 1 fs for all the MLPs.

For each MLP, three independent simulations were conducted. Figure 7(b) shows the time evolution of the fraction of  $\text{sp}^3$ -bonded atoms, with the shaded areas indicating the statistical error bounds calculated based on the standard error of the mean. The statistical errors are typically smaller than 1%. Figure 7(c) presents the  $\text{sp}^3$  fractions in the final configurations generated using the various MLPs. Results from other MLPs<sup>95,96</sup> and DFT calculations,<sup>95</sup> as well as experimental measurements<sup>97,98</sup> are also presented for comparison.

Among all the MLPs, NEP, DP, and MACE predict consistent  $\text{sp}^3$  fractions that are close to the DFT calculation results. In contrast, the NequIP model gives noticeably smaller  $\text{sp}^3$  fractions, while the predictions by

the GAP model are in between. Our results for the GAP model are also consistent with previous ones using the GAP approach but with different training data.<sup>95,96</sup> This means that it is the MLP approach that plays a crucial role here in determining the results. Although the predicted  $\text{sp}^3$  fractions from the NEP, DP, and MACE models are closer to the experimental data, there is still slight underestimation, which probably depends on the MD simulation protocol.<sup>100</sup>

#### 4. Computational speed

In addition to accuracy, computational speed is also a crucial feature for MLPs. To evaluate the computational performance of the various MLP models, we conducted MD simulations using diamond as the test system. We considered  $n \times n \times n$  supercells, with  $n$  ranging from 2 to 9 in increments of 1, and from 10 to 100 in increments of 10. For each MLP, simulations consisting of 100 steps were run, starting from the smallest system until memory limitations were reached.

Figure 8 compares the computational speed of these MLPs as a function of system size. Except for GAP, the

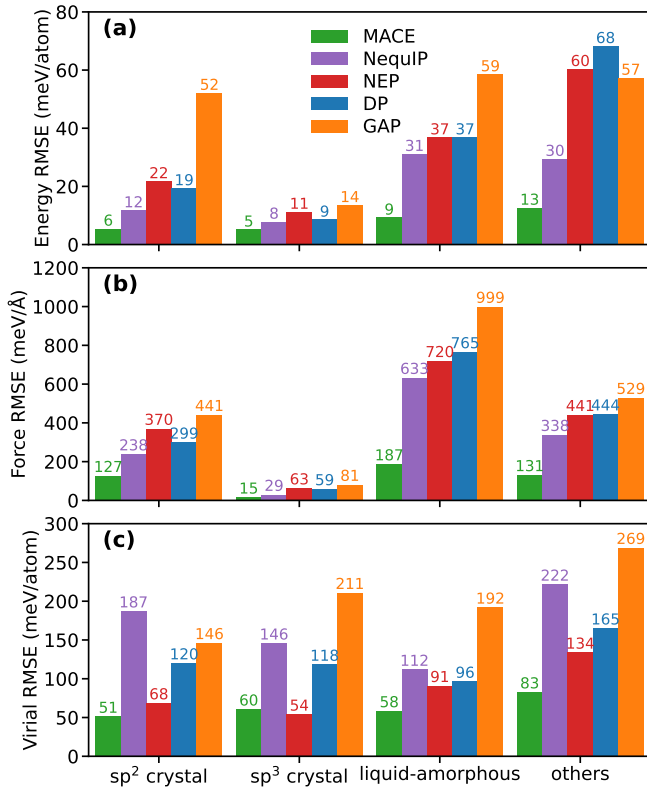


FIG. 4. Root-mean-square errors (RMSEs) for (a) energy, (b) force, and (c) virial across different sets of structures in the training dataset<sup>67</sup>, including sp<sup>2</sup>-bonded crystals, sp<sup>3</sup>-bonded crystals, liquid and amorphous structures, and others. Results are shown for various machine-learned potential models: DP,<sup>64</sup> GAP,<sup>63</sup> MACE,<sup>66</sup> NEP,<sup>9</sup> and NequIP.<sup>65</sup> The GAP model is from Ref. 67 and the NEP model is from Ref. 92. All other models were trained in the present work.

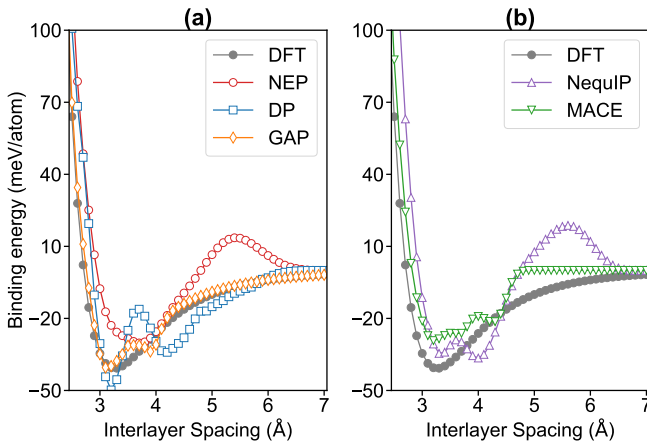


FIG. 5. Binding energy of AB-stacked bilayer graphene as a function of the interlayer spacing, as predicted by density functional theory (DFT) using the optB88-vdW functional and various machine-learned potential models: DP,<sup>64</sup> GAP,<sup>63</sup> MACE,<sup>66</sup> NEP,<sup>9</sup> and NequIP.<sup>65</sup> The DFT data are shown in both panels (a) and (b). The GAP model is from Ref. 67 and the NEP model is from Ref. 92. All other models were trained in this work.

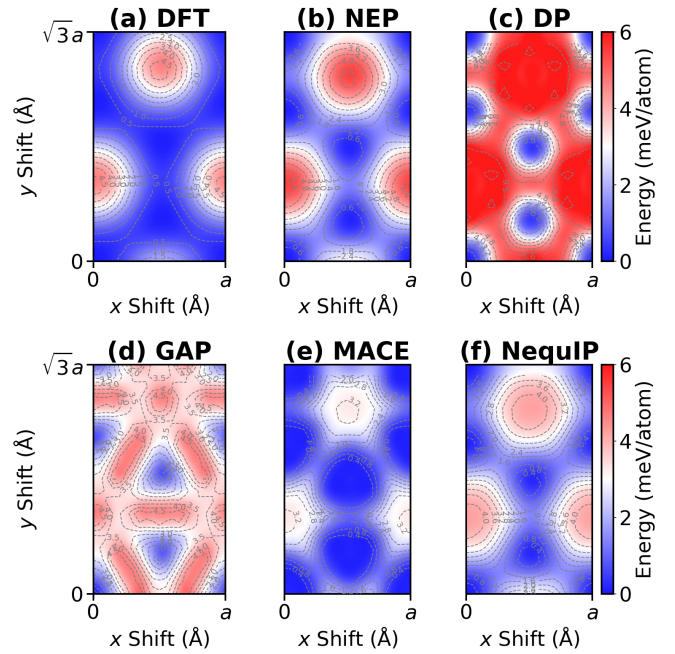


FIG. 6. Sliding energy profiles for bilayer graphene predicted by (a) density functional theory (DFT) using the optB88-vdW functional and (b-f) various machine-learned potential models: NEP,<sup>9</sup> DP,<sup>64</sup> GAP,<sup>63</sup> MACE,<sup>66</sup> and NequIP.<sup>65</sup> In each subplot, the energy origin is set to the total energy of the AB-stacked bilayer. The lateral lattice parameter is  $a = 2.46$  Å and the interlayer spacing is fixed at 3.4 Å. The GAP model is from Ref. 67 and the NEP model is from Ref. 92. All other models were trained in this work.

other MLP models all have GPU implementations and were tested using a single V100 GPU (32 GB of memory). For the GPU-based models, MACE and NequIP are the slowest and NEP is the fastest, while DP is in between. The speed of GAP with 64 CPU cores (256 GB of memory) is comparable to that of DP with one V100 GPU.

The NEP model achieves significantly higher computational speeds compared to the other MLP models, especially for large systems. The NEP model is also memory efficient, capable of simulating up to approximately six million atoms on a single V100 GPU. Thanks to its high memory efficiency, the NEP model has been used to simulate heat transport in polycrystalline graphene with over 1.4 million atoms<sup>101</sup> using a single consumer desktop RTX4090 GPU (24 GB of memory). The GPUMD package also supports multi-GPU parallelism, enabling simulations of systems with up to 100 million atoms. For example, a system size of 100 million atoms has been achieved using eight A100 GPUs (each with 80 GB of memory) with a recent NEP model for metal alloys.<sup>33</sup> Further evaluations of the computational speeds of NEP models, in comparison with other MLP approaches, can be found in several other studies.<sup>9,33,59,61,62,101,102</sup>

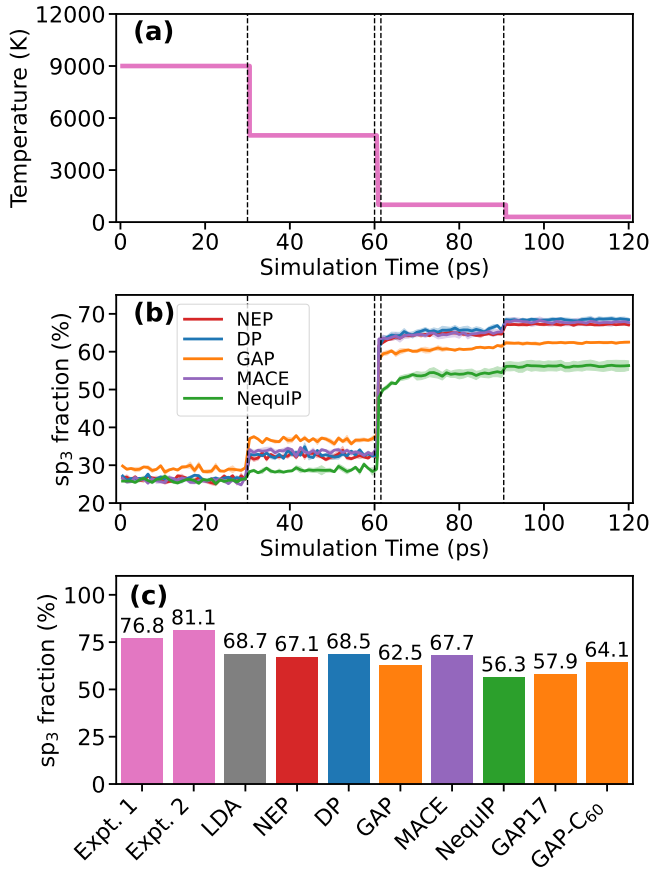


FIG. 7. (a) Temperature protocol used to generate 2744-atom amorphous carbon of density  $3.0 \text{ g cm}^{-3}$  in molecular dynamics simulations. (b) Time-evolution of the  $sp^3$  fraction as predicted by density functional theory (DFT) with the LDA functional<sup>95</sup> and various machine-learned potential models, including NEP,<sup>9</sup> DP,<sup>64</sup> GAP,<sup>63</sup> MACE,<sup>66</sup> and NequIP.<sup>65</sup> Standard error bounds are depicted as shaded areas. (c) Comparison of the final  $sp^3$  fraction after quenching among different calculations (including two extra ones, GAP17<sup>95</sup> and GAP-C<sub>60</sub><sup>96</sup>) and experimental results (“Expt. 1”<sup>97</sup> for a sample with density  $2.9 \text{ g cm}^{-3}$  and “Expt. 2”<sup>98</sup> for a sample with  $3.0 \text{ g cm}^{-3}$ ).

### C. Summary

The performance evaluation results presented above highlight the NEP approach’s standout computational speed. While some approaches achieve higher training accuracy, the NEP approach delivers reasonable results for static energetics and structural properties in complex dynamics. Carbon is one of the most versatile elements in the periodic table, and the capability of obtaining a well-behaved general-purpose model for carbon systems demonstrates that the NEP approach is a promising tool in modeling structural, mechanical, and phase-changing properties in complex materials, which we will discuss starting from the next section.

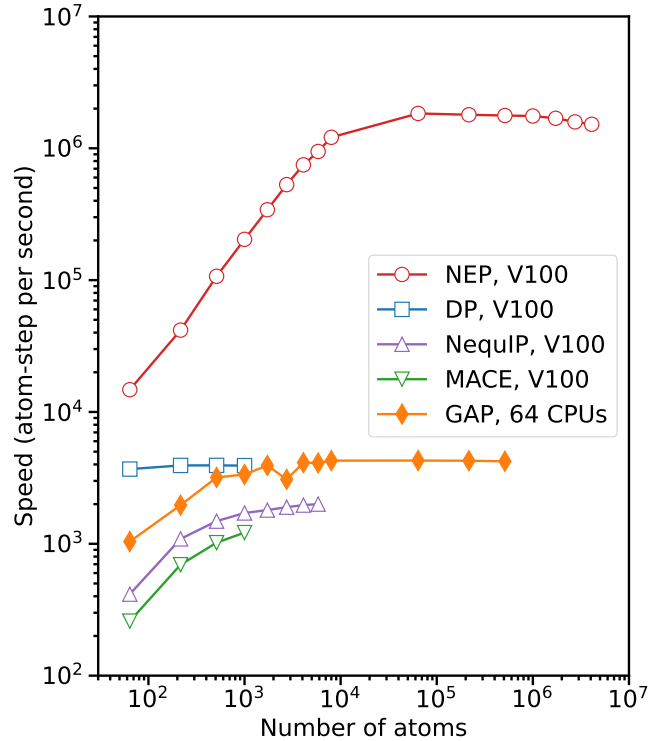


FIG. 8. Computational speeds as a function of the number of atoms (in diamond structure) for various machine-learned potential models: DP,<sup>64</sup> GAP,<sup>63</sup> MACE,<sup>66</sup> NEP,<sup>9</sup> and NequIP.<sup>65</sup> The GAP model was tested using 64 Xeon Platinum 9242 CPU cores with 256 GB of memory, while the other models were tested using a single V100 GPU with 32 GB of memory. The GAP model is from Ref. 67 and the NEP model is from Ref. 92. All other models were trained in the present work.

## IV. STRUCTURAL PROPERTIES

In this section, we examine how the NEP approach contributes to understanding the structural properties of complex materials. Here, “complex” refers to materials with either nontrivial atomic spatial distributions or diverse forms of intricate chemical order.

### A. Structural properties of disordered carbon and liquid water

Both disordered carbon and liquid water are representative examples of complex non-crystalline materials. Recent studies<sup>44,45</sup> have employed NEP-driven MD simulations to investigate their structure properties.

The structural complexity of disordered carbon arises from its diverse  $sp^3/sp^2$  bonding ratios and variable mass densities.<sup>103–105</sup> Disordered carbon can generally be categorized into  $sp^2$ -dominated graphene-based networks with lower density and  $sp^3$ -dominated amorphous carbon with higher density.<sup>44</sup> Liquid water exhibits a different form of structural complexity due to the interplay of co-

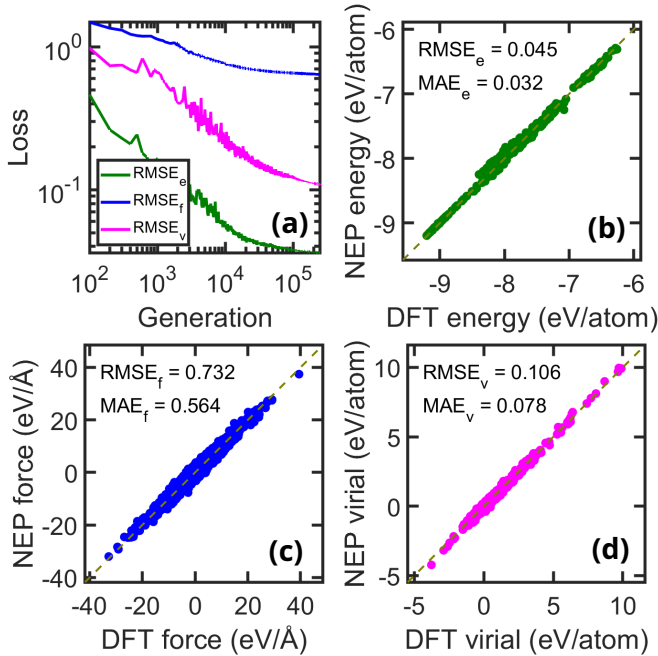


FIG. 9. The neuroevolution potential (NEP) model trained by Wang *et al.*<sup>44</sup> (a) Evolution of the training root-mean-square errors (RMSEs) for energy ( $\text{eV atom}^{-1}$ ), force ( $\text{eV \AA}^{-1}$ ) and virial ( $\text{eV atom}^{-1}$ ) as a function of the training generation (step). (b–d) Parity plots for (b) energy, (c) force, and (d) virial comparing NEP calculations with density function theory (DFT) calculations using the PBE functional, evaluated on a test set. The RMSEs and mean absolute errors (MAEs) are shown in the subplots. Adapted from Wang *et al.*<sup>44</sup>, arXiv:2408.12390 (2024).

valent bonds, hydrogen bonds, and van der Waals dispersion forces. This complexity is further amplified by significant nuclear quantum effects, especially in hydrogen bonding. Therefore, accurately describing the structural properties of these materials is fundamentally important for understanding their physical and chemical behaviors.

### 1. Disordered carbon

In a recent work, Wang *et al.*<sup>44</sup> developed a NEP model and systematically studied the structures and heat transport properties of disordered carbon with varying densities. The `nep.in` script they used reads as follows:

```

version      3
type         1 C
cutoff       4.2 3.7
n_max       8 6
l_max       4 2
basis_size   8 8
neuron      100
lambda_1    0.05
lambda_2    0.05
lambda_e    1.0

```

```

lambda_f    1.0
lambda_v    0.1
batch       6738
population   50
generation  250000

```

The evolution of the training RMSEs for energy, force, and virial are presented in Fig. 9(a), which are essentially converged at a step of 250 000. The trained NEP model was evaluated on an independent test dataset from Ref. 95. Parity plots in Fig. 9(b–d) for the test dataset confirm the robustness of the trained NEP model.

They considered a wide range of densities, from 0.3 to  $3.5 \text{ g cm}^{-3}$ . At relatively high density, a melt-quench-anneal MD protocol can produce amorphous carbon, as demonstrated in Fig. 7. At relatively low density, a melt-graphitization-quench protocol<sup>44</sup> can produce nanoporous carbon. Typical nanoporous carbon structures consist of entangled and curved graphene fragments assembled into a three-dimensional network with a high  $\text{sp}^2$  fraction.<sup>44,104,106</sup>

Figure 10 illustrates the morphologies of both nanoporous and amorphous carbon structures with varying densities. With increasing density, the nanoporous carbon structures display a monotonic decrease in the typical pore size but a nearly unchanged  $\text{sp}^2$  fraction that is over 98%. There is a small portion of  $\text{sp}$  atoms at the edges of the graphene fragments. In contrast, for amorphous carbon structures, the different bonding motifs are uniformly distributed, and the  $\text{sp}^3$  fraction gradually increases from 2% to 93% as the density increases from 1.5 to  $3.5 \text{ g cm}^{-3}$ . These structural characteristics are found to strongly correlate with other physical properties such as the thermal conductivity.<sup>44</sup>

### 2. Liquid water

Liquid water’s hydrogen-bonding network and anomalous properties present significant challenges for accurately modeling its structural, thermodynamic, and transport behavior across a wide range of conditions. While previous studies using MLPs,<sup>109–113</sup> including several employing the NEP approach,<sup>114–117</sup> have made progresses in predicting individual properties, achieving a unified computational framework capable of simultaneously capturing water’s complex and subtle properties with high accuracy has remained elusive. The precision of the quantum-mechanical method used to generate the training data, alongside the consideration of nuclear quantum effects, is vital for accurate atomistic modeling of water properties. To address this challenge, in a recent work, Xu *et al.*<sup>45</sup> trained a NEP model, denoted NEP-MB-pol, using reference data<sup>118</sup> from the coupled-cluster-level MB-pol approach.<sup>119–121</sup> The `nep.in` file reads:

```

version      4
type         2 0 H

```



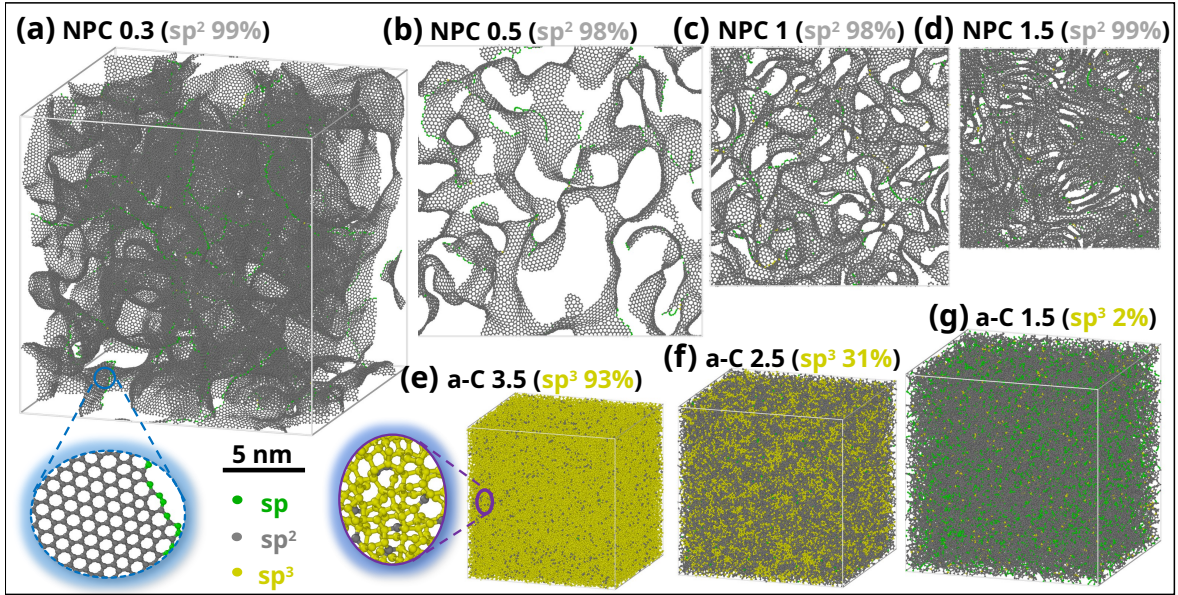


FIG. 10. Visualizations of disordered carbon structures. (a-d) nanoporous carbon (NPC) and (e-g) amorphous carbon (a-C). The numbers before the parentheses represent mass densities in units of  $\text{g cm}^{-3}$ , while those inside the parentheses indicate  $\text{sp}^2$  or  $\text{sp}^3$  ratios. Atoms with  $\text{sp}$ ,  $\text{sp}^2$  and  $\text{sp}^3$  bonding motifs are shown in green, gray and blue, respectively. Adapted from Wang *et al.*<sup>44</sup>, arXiv:2408.12390 (2024).

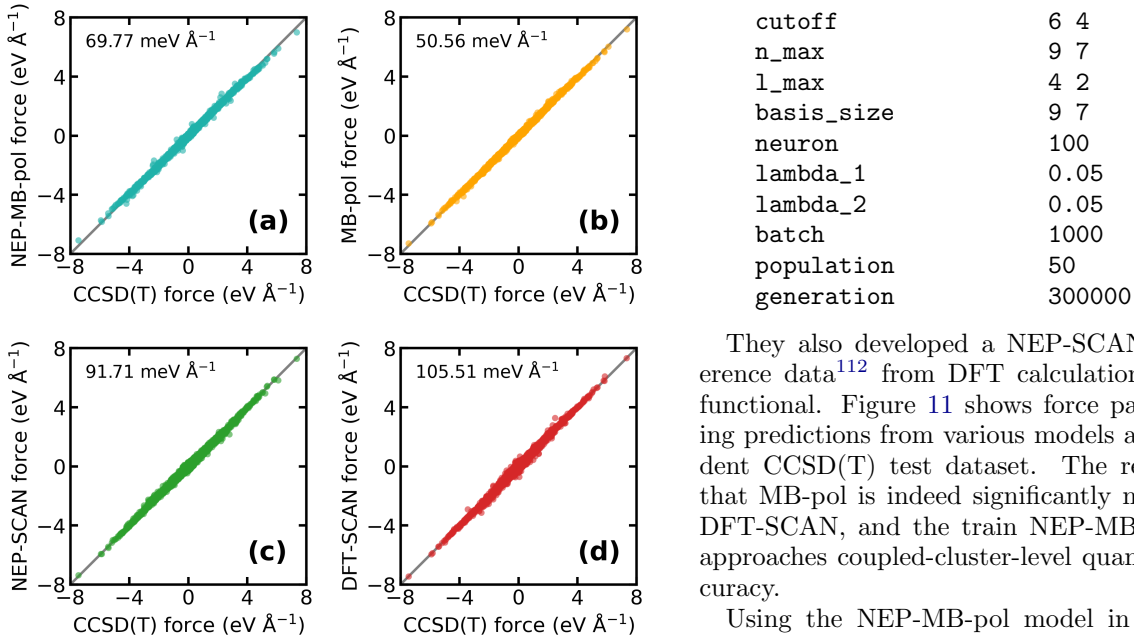


FIG. 11. Evaluation of force accuracies of a few water models. Parity plots comparing reference forces from coupled-cluster theory with single, double, and perturbative triple excitations [CCSD(T)] to forces predicted by: (a) neuroevolution potential (NEP) model trained on MB-pol dataset (NEP-MB-pol), (b) MB-pol model, (c) NEP model trained on the strongly constrained and appropriately normed (SCAN) dataset (NEP-SCAN), and (d) density functional theory (DFT) calculation with the SCAN functional. The root-mean-square error (RMSE) of force for each model is provided. Adapted from Xu *et al.*<sup>45</sup>, arXiv:2411.09631 (2024).

They also developed a NEP-SCAN model using reference data<sup>112</sup> from DFT calculations with the SCAN functional. Figure 11 shows force parity plots comparing predictions from various models against an independent CCSD(T) test dataset. The results demonstrate that MB-pol is indeed significantly more accurate than DFT-SCAN, and the train NEP-MB-pol model closely approaches coupled-cluster-level quantum chemistry accuracy.

Using the NEP-MB-pol model in path-integral MD simulations, radial distribution functions for water can be accurately calculated. For O-O pairs (Fig. 12(a)), the NEP-MB-pol model accurately reproduces experimental data even at the classical MD level, with path-integral MD introducing minimal changes, indicating negligible nuclear quantum effects for oxygen. In contrast, NEP-SCAN overshoots the first and second peaks in the O-O distribution.

Strong nuclear quantum effects significantly influence the distribution of O-H pairs (Fig. 12(b)) and H-H pairs (Fig. 12(c)). Classical MD simulations with both NEP-MB-pol and NEP-SCAN underestimate the peak widths

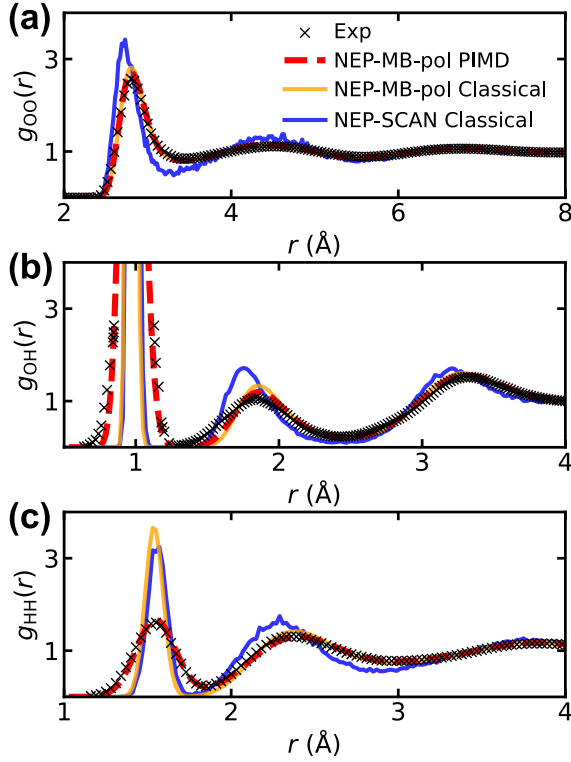


FIG. 12. Radial distribution functions of water: (a) O-O, (b) O-H, and (c) H-H atom pairs. Results from path-integral molecular dynamics (PIMD) simulations with NEP-MB-pol using 32 beads at 300 K (NEP-MB-pol PIMD, red dashed line) agree well with experimental data for O-O (295.1 K),<sup>107</sup> O-H (300 K)<sup>108</sup> and H-H (300 K)<sup>108</sup> atom pairs. For comparison, results from classical molecular dynamics (MD) simulations with NEP-MP-pol (orange line) and NEP-SCAN (blue line) are also shown. Adapted from Xu *et al.*<sup>45</sup>, arXiv:2411.09631 (2024).

in  $g_{OH}$  and  $g_{HH}$ , reflecting the absence of zero-point motion. Path-integral MD corrects this for NEP-MB-pol, aligning results closely with experimental data,<sup>122</sup> particularly for  $g_{HH}$ . This underscores the model’s high accuracy and the importance of nuclear quantum effects in describing O-H and H-H bonds.

The strength of NEP-MB-pol lies not only in its ability to accurately predict the structural properties of liquid water, but also in its capability to capture other thermodynamic properties, including density, heat capacity, transport coefficients, etc.<sup>45</sup>

## B. Chemical order in complex alloy systems

### 1. Chemical short-range order in GeSn alloys

Alloying plays a critical role in enhancing the properties and functionalities of various materials, including semiconductor alloys, medium-entropy, high-entropy and complex concentrated alloys, high-entropy ox-

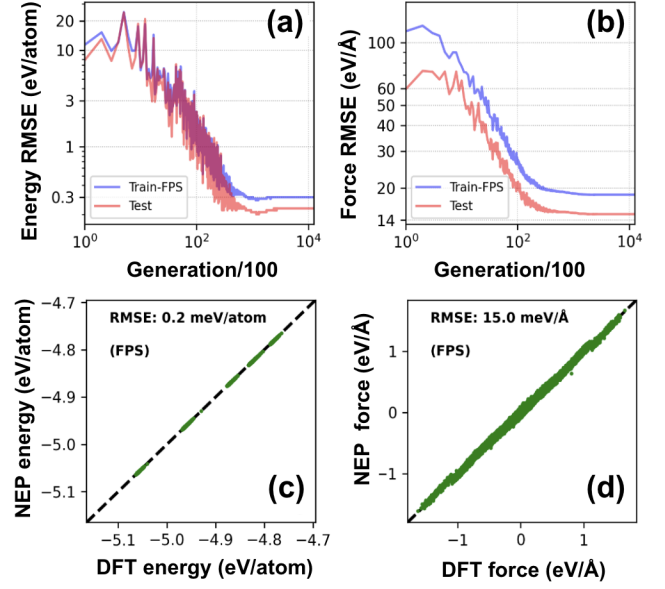


FIG. 13. Root mean square errors (RMSEs) for energy (a) and force (b) during neuroevolution potential (NEP) training with a farthest point sampling (FPS) reduced dataset and a testing dataset for GeSn alloys, plotted as a function of the number of generations in the evolutionary algorithm. Panels (c) and (d) show comparisons between NEP predictions and density functional theory (DFT) reference values for energy and force, respectively, on the test dataset. The use of the FPS dataset enhances predictive accuracy, achieving RMSEs of 0.2 meV atom<sup>-1</sup> for energy and 15.0 meV Å<sup>-1</sup> for force. Adapted with permission from Chen *et al.*<sup>23</sup>, Phys. Rev. Materials **8**, 043805 (2024).

ides/nitrides, and high-entropy metallic glasses. However, understanding the complex chemical order of these alloy systems, particularly their short-range order (SRO), poses significant challenges.

Group-IV alloys, known for their silicon compatibility, hold promise for electronic, photonic, and topological quantum applications.<sup>123–126</sup> Although group IV alloys have been long conceived as random solid solutions, recent DFT studies predicted complex SRO behavior in (Si)GeSn and GePb alloy systems.<sup>127–131</sup> Recent experimental studies also support the predicted structural complexity of GeSn alloys. For instance, atom probe tomography measurements, enhanced by an improved statistical method, reveal spatial fluctuations of atomic ordering in GeSn alloys.<sup>132</sup> The extended x-ray absorption fine structure technique<sup>133</sup> demonstrates a noticeable reduction in the Sn-Sn first coordination number (CN) compared to a random distribution. Polarization-dependent Raman spectroscopy detects the spectral characteristics of Ge and Sn atoms reflecting the effects of atomic ordering.<sup>134</sup>

Although advanced characterization techniques such as atom probe tomography<sup>132</sup> and energy-filtered transmission electron microscopy<sup>135</sup> are capable of probing atomic

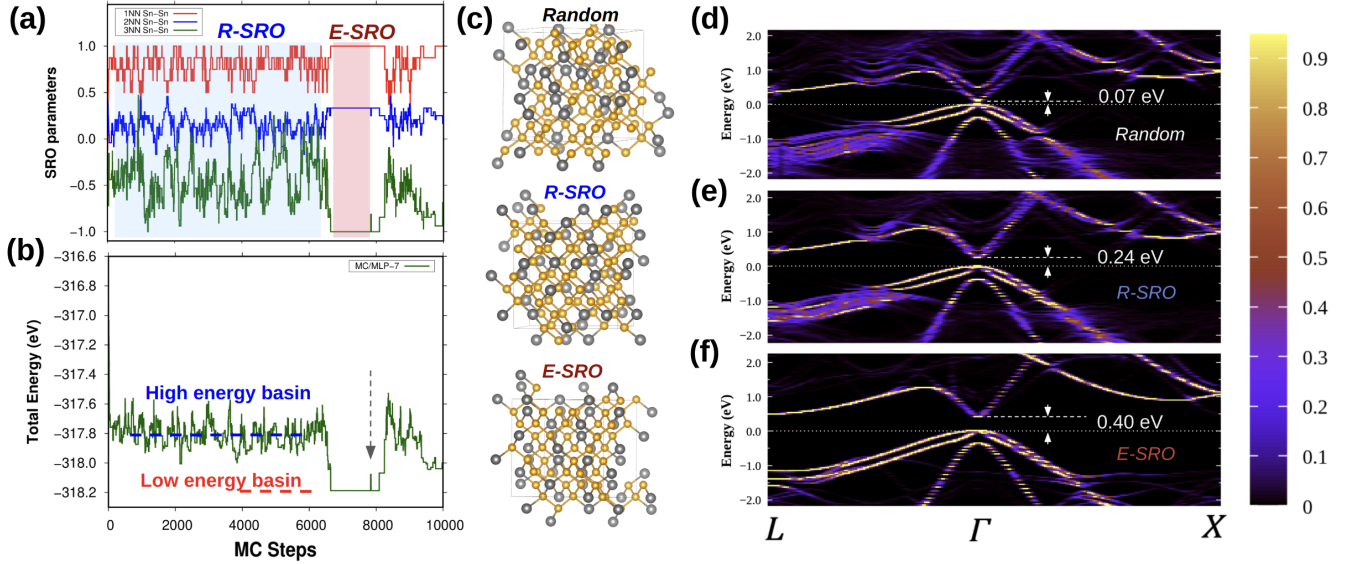


FIG. 14. Energy and structural variations arising from different types of short-range orders (SROs) in  $\text{Ge}_{0.75}\text{Sn}_{0.25}$  alloys. (a) illustrates the variation in the Sn-Sn SRO parameters for first-nearest neighbors (1NN) ( $\alpha_{\text{SnSn}}^1$ , red), second-nearest neighbors (2NN) ( $\alpha_{\text{SnSn}}^2$ , blue), and third-nearest neighbors 3NN ( $\alpha_{\text{SnSn}}^3$ , green). Regular SRO (R-SRO) exhibits a strong 1NN Sn-Sn depletion, a mild 2NN Sn-Sn repulsion, and a moderate 3NN Sn-Sn enhancement. Enhanced SRO (E-SRO) features a complete 1NN Sn-Sn depletion, a substantial 2NN Sn-Sn repulsion, and a significant 3NN Sn-Sn enhancement. (b) shows that the total energy fluctuates around the two distinct energy levels: the high-energy basin (blue dashed line) and the low-energy basin (red dashed line), separated by  $\sim 0.4$  eV. (c) depicts atomic configurations of random (special quasi-random structure), R-SRO, and E-SRO structures obtained from Monte Carlo trajectory.<sup>23</sup> Ge and Sn atoms are represented by gold and gray, respectively. (d) A random distribution results in a direct band gap at  $\Gamma$  of 0.07 eV. (e) R-SRO increases the direct band gap to 0.24 eV. (f) E-SRO leads to a further increase of direct band gap to 0.40 eV. The corresponding Bloch spectral weight is color-coded in the bar on the right. Adapted with permission from Chen *et al.*<sup>23</sup>, Phys. Rev. Materials **8**, 043805 (2024).

ordering at the scale of  $\sim 10$  nm, this is much larger than the length scales accessible via DFT sampling, leaving a significant gap between theoretical modeling and experimental characterizations.

To address this challenge, Chen *et al.*<sup>23</sup> recently developed a highly accurate and efficient NEP model tailored for GeSn alloys, utilizing a comprehensive dataset and farthest-point sampling, achieving remarkable accuracy with an energy RMSEs of  $0.2 \text{ meV atom}^{-1}$  and a force RMSEs of  $15.0 \text{ meV \AA}^{-1}$ . The comparisons between NEP predictions and DFT reference values are shown in Fig. 13.

Specifically, the original reference data for the structures were generated through DFT calculations using the Vienna *ab initio* simulation package,<sup>136</sup> based on the projector augmented wave method.<sup>88,89,137</sup> The local density approximation<sup>138</sup> was employed for the exchange-correlation functional, known for yielding the best agreement with experimental results for geometry optimization in pure Ge and Sn.<sup>139–142</sup> A simulation cell containing 64 atoms, obtained by replicating a conventional diamond cubic cell containing eight atoms twice along each dimension, was chosen to ensure sufficient sampling at the DFT level. The system size was demonstrated to be adequate for describing the SRO structures in Si-Ge-Sn alloy systems.<sup>127,129</sup> A  $2 \times 2 \times 2$  Monkhorst-Pack

$k$ -points grid<sup>143</sup> with a plane-wave cutoff energy of 300 eV is used. The conjugate-gradient algorithm is applied for structural relaxation during each energy calculation, with convergence criteria set at  $10^{-4}$  eV and  $10^{-3}$  eV for electronic and ionic relaxations, respectively. MC-DFT samplings are conducted to sample the configurational space of GeSn alloys, covering a broad range of compositions, including Sn concentrations of 3.125%, 4.6875%, 6.25%, 9.375%, 12.5%, 18.75%, 25%, 31.25%, 37.5%, 43.75%, 50%, 62.5%, 75%, 87.5%, 93.75%, 95.3125%, and 96.875%. The total DFT reference dataset consists of 306 677 structures, totaling 19 627 328 atoms, for GeSn alloys, covering the full range of compositions. The broad range of composition of the initial training dataset ensures a robust NEP model capable of effectively sampling configurations in GeSn alloys. Although the original DFT calculations for these structures require approximately one million CPU hours,<sup>127</sup> it was demonstrated in the same work<sup>23</sup> that the size of the most essential data for achieving the required level of accuracy, thus the required computational cost, could be significantly smaller. Particularly, they performed farthest point sampling (FPS) with a minimum Euclidean distance of 0.02 to sample the descriptor space of the original full training dataset. FPS involves selecting data points that are farthest apart from each other, allowing us to capture



the essential geometric structure of the entire dataset while avoiding redundancy. The resulting dataset from FPS sampling comprises only 137 structures, representing a three-order-of-magnitude reduction from the original training dataset. This dataset is referred as the FPS dataset. FPS aids in capturing diverse and representative samples, and can be further used for constructing an efficient and representative training dataset for MLPs under various conditions. The descriptor space for both the original full dataset and the FPS dataset was visualized using principal component analysis, showing that the FPS dataset effectively covers the original full dataset in the two-dimensional reduced descriptor space.<sup>23</sup> Utilizing this FPS dataset, the predictive accuracy of this NEP model on the same testing dataset shows a further improvement, achieving RMSEs of 0.2 meV atom<sup>-1</sup> for energy (Fig. 13c) and 15.0 meV Å<sup>-1</sup> for force (Fig. 13(d)), respectively. This improvement may be attributed to more weighted training on representative configurations, suggesting the importance of considering the weight of representative configurations under different conditions when developing MLPs for diverse applications. The enhanced accuracy also highlights the significant data efficiency of the NEP approach.

The relevant input hyperparameters for training the GeSn NEP model<sup>23</sup> specified in the `nep.in` input file are provided below.

```

type          2 Ge Sn
version       4
cutoff        7 5
n_max        4 4
basis_size    12 8
neuron        30
lambda_1      0.1
lambda_2      0.1
lambda_e      1.0
lambda_f      1.0
lambda_v      0.1
force_delta   1.0
batch         2000
population    100
generation    1250000

```

The keyword `force_delta` specifies a parameter  $\delta = 1$  eV Å<sup>-1</sup> used for modifying the force loss function in the following way:

$$L_f = \sqrt{\frac{1}{3N} \sum_{i=1}^N (\mathbf{F}_i^{\text{NEP}} - \mathbf{F}_i^{\text{ref}})^2 \frac{1}{1 + \|\mathbf{F}_i^{\text{ref}}\|/\delta}}.$$

Here,  $N$  is the number of atoms in a training batch,  $\mathbf{F}_i^{\text{NEP}}$  and  $\mathbf{F}_i^{\text{ref}}$  are NEP-predicted and DFT reference forces acting on atom  $i$ , respectively. Without the introduction of  $\delta$  (equivalent to the limit  $\delta \rightarrow \infty$ ), the above expression is just the RMSE of force. With a value of  $\delta = 1$  eV Å<sup>-1</sup>, the above expression emphasizes more on the target forces with smaller magnitudes. This is particularly beneficial for minimization applications, where

small forces are crucial in determining the local minima of the potential energy landscape.

The exceptional computational efficiency of NEP extends the spatiotemporal scale of MC sampling at first-principles accuracy, enabling new discoveries of SRO behavior in GeSn alloys, which were hidden from computationally demanding DFT-based sampling.

Through extensive NEP-based MC sampling, as shown in Fig. 14, they identify a new type of local ordering, enhanced-SRO, that is featured by a complete depletion of 1NN Sn-Sn, a mild depletion of 2NN Sn-Sn, and a significant enhancement of 3NN Sn-Sn, exhibiting a greater degree of SRO than the regular-SRO previously predicted based on DFT sampling.<sup>127</sup> And the 1NN, 2NN, and 3NN Sn-Sn SRO parameters (Fig. 14(a)) show strong correlation with the total energy (Fig. 14(b)). The structure variations caused by SRO are demonstrated to significantly impact the band structures of GeSn alloys. As illustrated in Fig. 14(d-f), significant distinctions emerge among the three structural types (Figure 14(c)). The band structure of the random alloy shows a small direct band gap at  $\Gamma$  ( $\sim 0.07$  eV). Regular-SRO increases the gap to  $\sim 0.24$  eV. Remarkably, enhanced-SRO further increases the direct gap at  $\Gamma$  to  $\sim 0.40$  eV.

The coexistence of two types of SRO in GeSn alloys is further confirmed through large-scale MC-NEP sampling, utilizing supercells of  $11.7 \times 11.7 \times 11.7$  nm<sup>3</sup>, matching the effective size measured by atom probe tomography.<sup>132</sup> The large-scale modeling clearly reveals the structural heterogeneity of GeSn alloy, demonstrating the presence of nano-sized SRO domains with various degrees of local ordering.<sup>23</sup> Notably, these domains could form nanohomojunctions with distinct band gaps, potentially enabling novel optoelectronic applications.<sup>144</sup>

The developed NEP model for GeSn alloys<sup>23</sup> effectively bridges the gap between modeling and experimental characterization,<sup>145</sup> enabling more definitive understanding of SRO. This study sets an example and benchmark for investigating SRO in other complex alloy systems. Recently, the NEP model for GeSn alloys has been extended to Si-Ge-Sn alloys, enabling side-by-side comparisons with experimental characterizations.<sup>41,146</sup>

## 2. Compositionally complex alloys

In a recent study, Song *et al.*<sup>33</sup> developed a general-purpose machine-learned potential for 16 elemental metals and their alloys, known as the UNEP-v1 model. They demonstrated that UNEP-v1 model achieves excellent accuracy, efficiency, and generalization capabilities for complex materials such as high-entropy alloys and compositionally complex alloys.<sup>33</sup>

Specifically, they presented a promising approach for constructing a unified general-purpose MLP for numerous elements and showcase its capability by developing a model (UNEP-v1) for 16 elemental metals (Ag, Al, Au, Cr, Cu, Mg, Mo, Ni, Pb, Pd, Pt, Ta, Ti, V, W, Zr) and

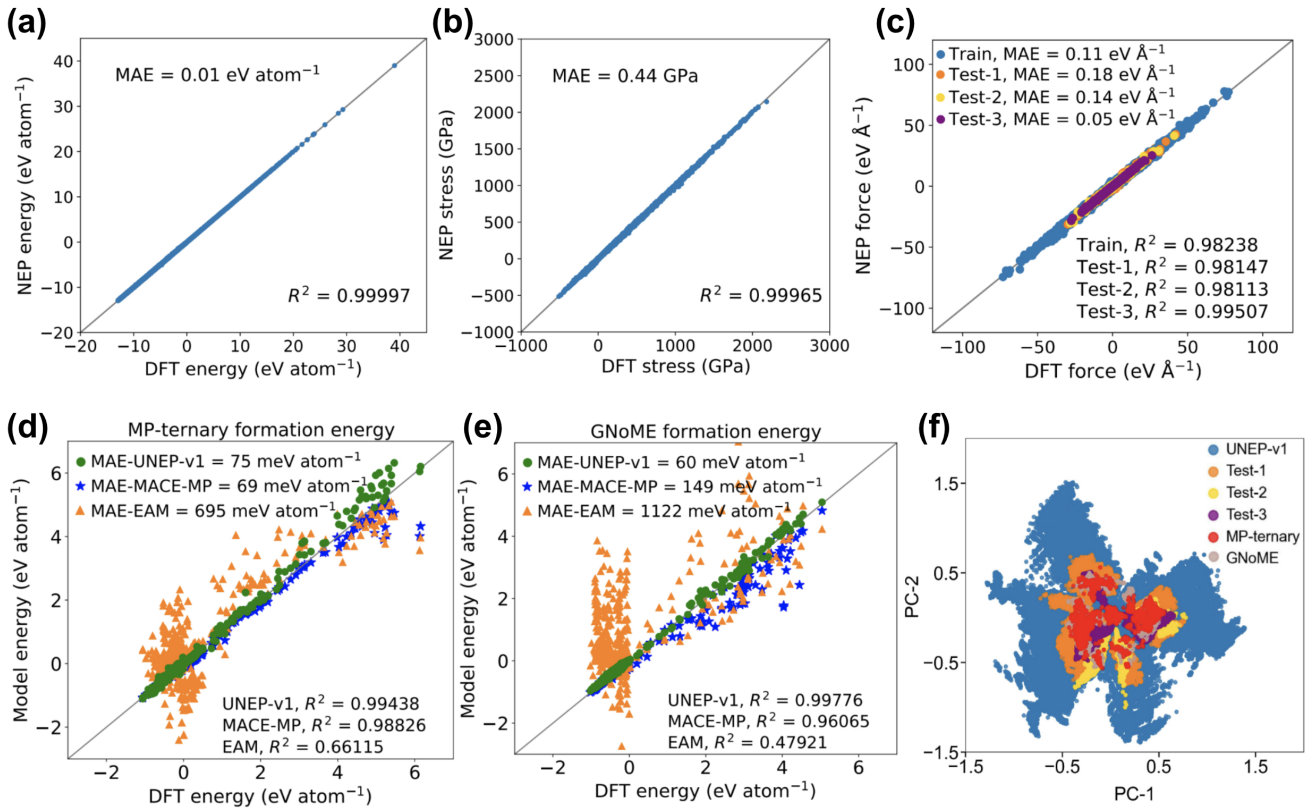


FIG. 15. Performance evaluation of UNEP-v1 using the training and test datasets. (a–c) Parity plots for energy, stress, and force comparing density functional theory (DFT) reference data and the first version of unified neuroevolution potential (UNEP-v1) predictions for the whole training dataset. In (c), there are three test datasets containing  $n \geq 3$  structures, including one with up to 13 components (Ag, Au, Cr, Cu, Mo, Ni, Pd, Pt, Ta, Ti, V, W, Zr) taken from Lopanitsyna *et al.*<sup>147</sup> (labeled Test-1), one with up to four components (Mo, Ta, V, W) from Byggmästar *et al.*<sup>148</sup> (labeled Test-2), and one with up to three components (Pd, Cu, Ni) from Zhao *et al.*<sup>22</sup> (labeled Test-3). (d–e) Parity plots for formation energies comparing DFT reference data and predictions from UNEP-v1 (green circles), MACE-MP-0 (medium model, blue stars),<sup>149</sup> and embedded-atom method (EAM) (orange triangles),<sup>150</sup> for structures from the Materials Project (MP-ternary)<sup>151</sup> and the GNoME paper.<sup>152</sup> Mean absolute error (MAE) and  $R^2$  (coefficient of determination) values are provided for comparison. (f) Distribution of the training dataset (UNEP-v1, comprising 1-component to 2-component systems, blue) and various test datasets, including Test-1 (up to 13-component systems, orange),<sup>147</sup> Test-2 (up to 4-component systems, yellow),<sup>148</sup> Test-3 (up to 3-component systems, purple),<sup>22</sup> MP-ternary alloys (3-component systems, red),<sup>151</sup> and GNoME dataset (2-component to 5-component systems, green),<sup>152</sup> in the 2D principal component (PC) space of the descriptor. Adapted with permission from Song *et al.*<sup>33</sup>, Nat. Commun. **15**, 10208 (2024).

their diverse alloys. To achieve a complete representation of the chemical space, they demonstrated that employing 16 one-component and 120 two-component systems suffices, thereby avoiding the enumeration of all 65535 possible combinations for training data generation. Furthermore, they illustrated that systems with more components can be adequately represented as interpolation points in the descriptor space.

They used the following inputs in the `nep.in` file to train UNEP-v1:

```

type      16 Ag Al Au Cr Cu Mg Mo Ni
          Pb Pd Pt Ta Ti V  W  Zr
version   4
cutoff    6 5
n_max     4 4

```

```

basis_size 8 8
l_max      4 2 1
neuron     80
lambda_1   0
lambda_e   1
lambda_f   1
lambda_v   0.1
batch      10000
population 60
generation 1000000
zbl        2

```

The parity plots for energy, force, and stress affirm the high accuracy of this UNEP-v1 model (Figure 15a–c). Despite the large ranges of the three quantities, their RMSEs are relatively small, at 17.1 meV atom<sup>-1</sup>, 172



meV  $\text{\AA}^{-1}$ , and 1.16 GPa, respectively.

To validate the force accuracy of the UNEP-v1 model, they considered three public datasets. The comparison (Figure 15c) shows that the UNEP-v1 model trained on 1-component and 2-component structures also performs very well for 3-component,<sup>22</sup> 4-component,<sup>148</sup> and 13-component.<sup>147</sup> structures The testing RMSEs of the UNEP-v1 model for these three datasets are respectively 76 meV  $\text{\AA}^{-1}$ , 196 meV  $\text{\AA}^{-1}$ , and 269 meV  $\text{\AA}^{-1}$ , which are comparable to those reported as training RMSEs in the original publications.<sup>22,147,148</sup>

To validate the energy accuracy of the UNEP-v1 model, they utilized two public datasets, including all the relevant 3-component structures in the Materials Project database<sup>151</sup> and the structures predicted using the GNoME approach<sup>152</sup> ranging from 2-component to 5-component systems with force components less than 80 eV  $\text{\AA}^{-1}$ . They calculated the formation energies using DFT, an embedded-atom method potential,<sup>150</sup> a foundation model named MACE-MP-0 (medium version),<sup>149</sup> and the UNEP-v1 model, where the reference energy for each species is based on the most stable allotrope. For the two datasets, the mean absolute error of the UNEP-v1 model compared to DFT calculations are 75 meV atom<sup>-1</sup> and 60 meV atom<sup>-1</sup>, respectively (Figure 15d and Figure 15e). In contrast, the corresponding values from the embedded-atom method potential are 695 meV atom<sup>-1</sup> and 1122 meV atom<sup>-1</sup>, respectively, about one order of magnitude larger. For the Materials Project dataset, which MACE-MP-0 has been trained on while UNEP-v1 has not, MACE-MP-0 is slightly more accurate. However, for the GNoME dataset, on which neither model has been trained, UNEP-v1 demonstrates notably better accuracy.

The results altogether clearly demonstrate the superior accuracy of UNEP-v1 over embedded-atom method and confirm the excellent generalizability of our UNEP-v1 model from the 1- and 2-component structures included in the training dataset to unseen multi-component structures.

As a further test, they trained a NEP model by including relevant  $n$ -component ( $n \geq 3$ ) structures from the Open Quantum Materials Database database.<sup>153</sup> The RMSEs for the three public datasets<sup>22,147,148</sup> obtained using this NEP model are only marginally improved compared to UNEP-v1, which demonstrates that the training dataset with  $n$ -component ( $n \leq 2$ ) structures is already sufficient for training a general-purpose NEP model for all the considered elements and their alloys.

A pivotal insight driving the success of their approach to training data generation is the recognition that chemical (species) information can be embedded in the trainable expansion coefficients of radial functions, dependent only on atom pairs and basis functions. As a result, the 1-component and 2-component structures delineate an outer boundary in descriptor space, while  $n$ -component structures with  $n \geq 3$  represent interpolation points in this space. This feature is illustrated by a principal

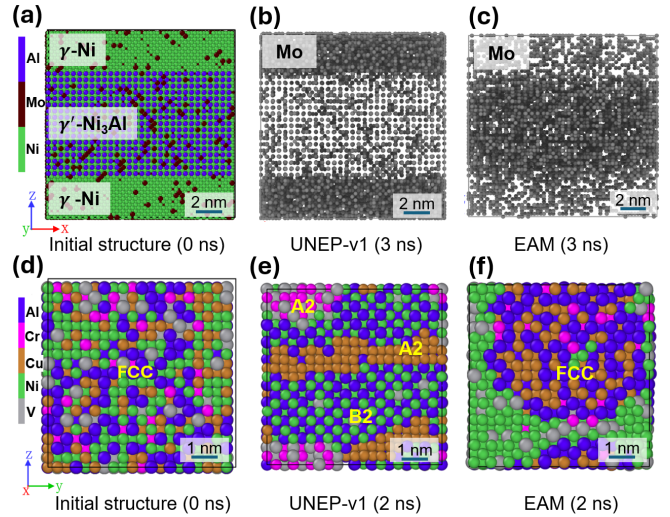


FIG. 16. Comparisons between the first version of unified neuroevolution potential (UNEP-v1) by Song *et al.*<sup>33</sup> and the embedded-atom method (EAM) by Zhou *et al.*<sup>150</sup> in hybrid Monte Carlo and molecular dynamics (MCMD) simulations. (a) Initial structure of a  $\gamma$ -Ni and  $\gamma'$ -Ni<sub>3</sub>Al superlattice with a random Mo distribution. (b-c) Snapshots of the final equilibrium Mo distributions from MCMD simulations using UNEP-v1 and EAM models.<sup>150</sup> (d) Initial face-centered cubic (FCC) structure of Al<sub>0.31</sub>Cr<sub>0.06</sub>Cu<sub>0.22</sub>Ni<sub>0.32</sub>V<sub>0.09</sub>. (e-f) Snapshots of the final equilibrium structures from MCMD simulations using UNEP-v1 and EAM models.<sup>150</sup> UNEP-v1 successfully produces both disordered (A2) and ordered (B2) body-centered cubic (BCC) structures in full agreement with experiments.<sup>156</sup> In contrast, EAM potential by Zhou *et al.*<sup>150</sup> keeps the system in the FCC structure, unable to reproduce the experimentally expected BCC structure. Adapted with permission from Song *et al.*<sup>33</sup>, Nat. Commun. **15**, 10208 (2024).

component analysis of the descriptor space (Figure 15f), which shows that the various  $n$ -component ( $n \geq 3$ ) structures fall comfortably within the space spanned by the 1-component and 2-component training structures.

Utilizing highly efficient hybrid MC and MD simulations<sup>43</sup> with the UNEP-v1 model, they investigated Mo distribution in a superlattice structure formed by  $\gamma$ -Ni and  $\gamma'$ -Ni<sub>3</sub>Al. Starting from a uniform Mo distribution with an overall concentration of 8.1% (Figure 16a), the UNEP-v1 model predicted a final Mo concentration ratio of  $K^{\gamma'}/\gamma = 0.667$  (Fig. 16(b)). This aligns with experimental findings that suggest  $K^{\gamma'}/\gamma < 1$  for initial Mo concentrations above approximately 6%.<sup>154,155</sup> In contrast, the embedded-atom method potential by Zhou *et al.*<sup>150</sup> produced a significantly overestimated value of  $K^{\gamma'}/\gamma = 4.981$  (Fig. 16(c)), inconsistent with experimental trends.

Furthermore, the UNEP-v1 model was applied to study the phase stability of an Al-rich intermetallic alloy, Al<sub>0.31</sub>Cr<sub>0.06</sub>Cu<sub>0.22</sub>Ni<sub>0.32</sub>V<sub>0.09</sub>, with the presence of a large fraction of face-centered cubic metals. Starting from an initial face-centered cubic structure (Fig-

ure 16(d)), the hybrid MC and MD simulations with the UNEP-v1 model accurately reproduced the experimentally observed body-centered cubic structure, including both disordered (A2) and ordered (B2) phases (Fig. 16(e)), in agreement with experimental data.<sup>156</sup> By contrast, the embedded-atom method potential by Zhou *et al.* failed to capture this phase transition, retaining the system in the face-centered cubic structure (Fig. 16(f)). These results demonstrate the ability of the UNEP-v1 model<sup>33</sup> to accurately capture phase transitions and chemical order in complex alloy systems.

### C. Summary

In this section, we have highlighted successful applications of the NEP approach in investigating structural properties across a wide range of complex materials systems, including disordered carbon, liquid water, GeSn alloys, and compositionally complex alloys. The developed NEP models demonstrate impressive predictive capability and exceptional computational efficiency, enabling the accurate description of the structural properties of these complex materials.

For disordered carbon,<sup>44</sup> nanoporous carbon structures exhibit a monotonic decrease in typical pore size with increasing density while maintaining an  $sp^2$  fraction over 98%. In amorphous carbon structures, bonding motifs are uniformly distributed, with the  $sp^3$  fraction gradually increasing as density rises.

For liquid water,<sup>45</sup> the developed NEP-MB-Pol model demonstrates quantum chemistry-level accuracy and reproduces experimentally measured structural properties of water such as radial distribution functions for all atom pairs, with quantum-correction techniques to incorporate nuclear quantum effects. NEP-MB-pol model outperforms DFT-SCAN and other MLP models, representing a versatile and scalable approach with promising applications for exploring the unique properties and phenomena of water and related systems across multiple fields.

For GeSn alloys,<sup>23</sup> the developed NEP model enables large-scale atomistic simulations that bridge the spatiotemporal gap between modeling and advanced characterization techniques. It facilitates the discovery of structural intricacies in GeSn alloys, setting an example and benchmark for investigating short-range order in broader alloy systems. Furthermore, it suggests the significance of weighting representative configurations under various conditions for developing MLP models and highlights the remarkable data efficiency of the NEP approach.

For compositionally complex alloys,<sup>33</sup> the developed UNEP-v1 model achieves excellent accuracy, efficiency, and generalization capabilities in predicting complex chemical order in these alloys. This study demonstrates a promising approach that leverages the embedded chemical generalizability and the neuron network interpolation capabilities of NEP model, paving the way for constructing of a unified general-purpose MLP encompassing the

periodic table.

As emphasized in the introduction, the processes and properties discussed in this review often overlap and are interconnected. In particular, the study of structural properties usually requires the generation of particular phases of a material. Therefore, the capability of generating different phases and describing the phase transitions is an important aspect of a MLP approach, which will be explored in the next section.

## V. PHASE TRANSITIONS AND RELATED PROCESSES

In this section, we discuss applications of the NEP approach in studying phase transitions and related topics such as surface reconstruction, material growth, and radiation damage.

### A. Phase transitions of materials

Phase transitions include crystal-to-crystal transformations, crystal-to-liquid (or amorphous) transitions, and their reversals, typically driven by external stimuli such as temperature, pressure, mechanical deformation, or shock compression. With its high efficiency and near *ab initio* accuracy, the NEP approach has been widely employed in phase transition modeling.

For crystal-to-crystal transitions, perovskite crystals have been the primary focus of many studies.<sup>11–13,18,24,40</sup> Fransson *et al.*<sup>12</sup> employed NEP models to investigate the effects of size and heating/cooling rate on the orthorhombic-tetragonal-cubic phase transitions of halide perovskites. Their findings indicate that achieving convergence of the transition temperature requires system sizes of at least several tens of thousands of atoms, along with heating/cooling rates below approximately 60 K ns<sup>-1</sup>. As shown in Fig. 17, smaller systems with 1,280 atoms yield inconsistent transition temperatures during the heating and cooling processes. However, this discrepancy diminishes as the system size increases, and both transition temperatures fully converge when the system size reaches 23,040 atoms. By analyzing the transition temperatures predicted by ensemble NEP models (trained on part of the full dataset) and a full NEP model (trained on the full dataset), they estimated the prediction error arising from model uncertainty to be around 30 K. Their study demonstrate the efficiency, accuracy, and robustness of NEP models in simulating phase transitions in halide perovskites.

Ahlawat<sup>40</sup> recently conducted extensive solid-solid co-existence simulations between the (110) and (100) perovskite facets. These simulations uncovered a layer-by-layer transformation mechanism underlying the growth process (Fig. 18). To validate phase stability during interfacial dynamics, NEP-driven simulations were performed for up to 2 microseconds. It was found that the

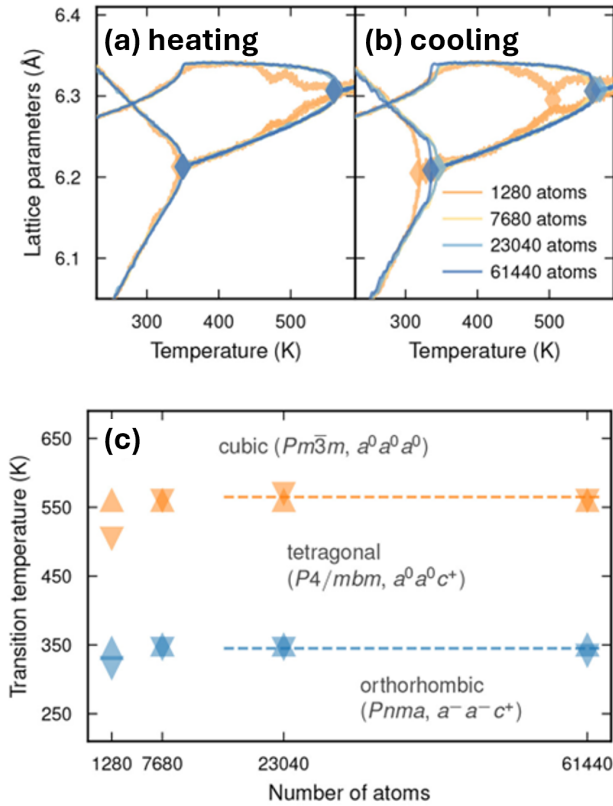


FIG. 17. Phase transition in  $\text{CsPbI}_3$ . Lattice parameters of  $\text{CsPbI}_3$  as a function of temperature from molecular dynamics simulations driven by a neuroevolution potential model during (a) heating and (b) cooling at a rate of  $6 \text{ K ns}^{-1}$  for various simulation sizes. Diamonds indicate the transition temperatures extracted from these data. (c) Transition temperatures as a function of the simulation size. Reproduced with permission from Fransson *et al.*,<sup>12</sup> *J. Phys. Chem. C*, **127**, 13773 (2023). Copyright 2023 American Chemical Society.

(110) facet forms a well-defined and stable boundary with the  $\delta$  phase, while the (100) facet exhibits mobile boundary atoms. Notably, the study also identified that a critical nucleus of at least 5.5 nm is necessary for the formation of a faceted perovskite crystal during solid-solid crystallization. This study demonstrates the capability of the NEP approach to perform large-scale and long-term MD simulations crucial for understanding phase transitions.

Beyond perovskites, NEP-driven MD simulations have also been applied to investigate the crystallization dynamics of Sb-Te phase-change materials<sup>27</sup> and boron nitride.<sup>39</sup>

In addition to temperature variations, solid-solid phase transitions can also be triggered by tension or compression. For instance, Huang *et al.*<sup>25</sup> utilized a NEP model for carbon Kagome lattices to uncover remarkable ductility under uniaxial tension, due to a phase transition occurring during the tension process. Through NEP-driven

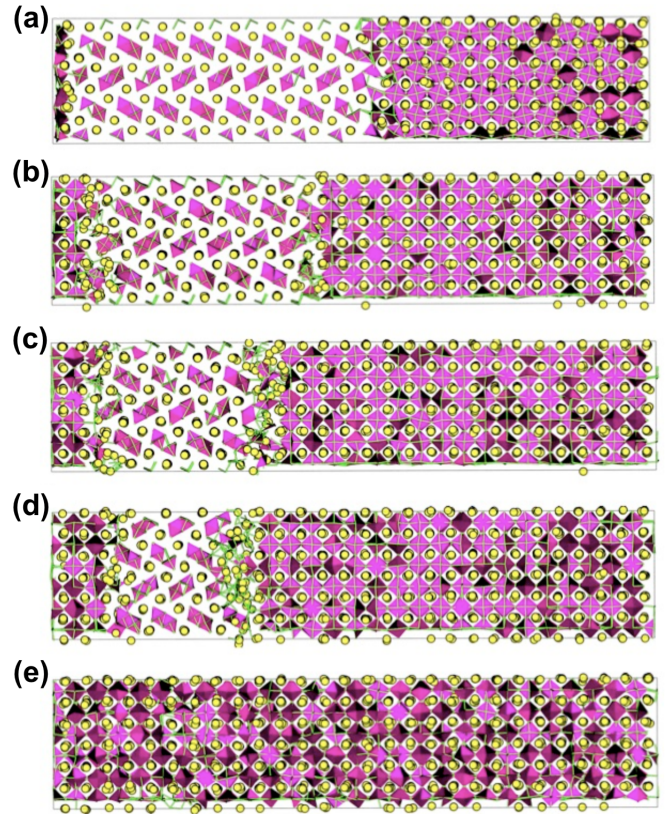


FIG. 18. Solid-solid co-existing simulations of  $\sigma$  and  $\alpha$  phases of (100)-perovskite-facet. Subplots (a) to (e) illustrate the temporal progression of structural changes during co-existing simulations. For clarity, only magenta-colored Pb-I octahedra are displayed alongside yellow cesium atoms. Adapted from Ahlawat<sup>40</sup>, *arXiv:2404.05644* (2024).

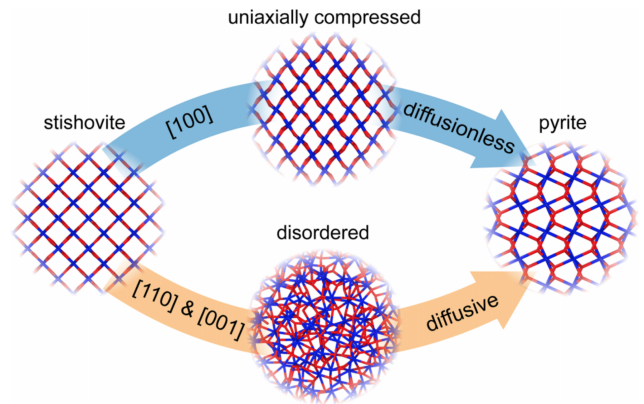


FIG. 19. Schematic illustration of two different phase transformation pathways from stishovite to pyrite phase. Adapted with permission from Pan *et al.*<sup>30</sup>, *Phys. Rev. B* **110**, 224101 (2024).



MD simulations, Yu *et al.*<sup>37</sup> demonstrated that uniaxial strain-induced phase transitions in Janus graphene significantly suppress thermal conductivity and induce strong anisotropy through the formation of a transitional mesophase. Shi *et al.*<sup>16</sup> employed a NEP model for high-pressure carbon systems and designed a thermodynamic pathway to synthesize the elusive BC8 carbon from diamond. Pan *et al.*<sup>30</sup> developed a NEP model for silicon oxide systems and conducted extensive MD simulations with multimillion-atom systems to reveal the compression pathways required to transform stishovite into the pyrite phase (Fig. 19).

At high temperatures and pressures, solid states can transform into liquid or amorphous states. Li and Jiang<sup>14</sup> investigated the phase diagram of carbon peapod arrays under extreme conditions using the NEP approach. They successfully reproduced several experimentally observed carbon structures. Their findings showed that defects facilitate the transition from an ordered crystalline structure to a disordered amorphous structure at low temperatures, while hindering the formation of an ordered diamond structure.

These studies underscore the effectiveness of the NEP approach as a powerful tool to perform extensive simulations across varying temporal and spatial scales under diverse external physical stimuli.

## B. Case study: Surface reconstruction

Since the experimental discovery of the Si(111) ( $7 \times 7$ ) reconstruction, extensive experimental and theoretical efforts have been devoted to elucidating its atomic structure.<sup>157–160</sup> Through these studies, the dimer-adatom-stacking fault model has been established as the dominant reconstruction mode. However, classical force fields, such as Tersoff, modified embedded-atom method, and Stillinger-Weber, fail to predict the Si(111) ( $7 \times 7$ ) reconstruction as the ground state, instead favoring the pristine Si(111) surface.<sup>161</sup> This discrepancy conflicts with both experimental observations and DFT calculations. In contrast, the GAP approach<sup>161</sup> has demonstrated the ability to accurately capture the subtle energy differences between surface configurations, correctly identifying the Si(111) ( $7 \times 7$ ) surface as the most stable structure. Furthermore, by leveraging MLPs,<sup>162,163</sup> potential pathways and kinetic processes governing the Si(111) surface reconstruction have been proposed.

Gold (Au) and Platinum (Pt) are among the  $5d$  transition metals, known for their exceptional stability and robust chemical activity in oxidizing environments. It is well-established that surfaces of  $5d$  transition metals undergo atomic rearrangements driven by surface tension effects, leading to surface reconstructions.<sup>164–168</sup> To elucidate the origin of the Au(111) herringbone reconstruction, which exhibits a remarkably large periodic length ( $\sim 30$  nm), Li and Ding developed a DP model for Au.<sup>169</sup> Their findings revealed that the herringbone

reconstruction remains highly stable at elevated temperatures, while a slight strain of approximately  $\pm 0.2\%$  can induce a transition from the herringbone pattern to a stripe pattern.

Similarly, Qian *et al.* constructed a comprehensive training set for Pt, encompassing diverse structures such as bulk, surfaces, and clusters.<sup>170</sup> Using this high-quality dataset, they trained a DP model with high accuracy, enabling precise simulations of Pt surface reconstruction kinetics and predictions of the morphology of vicinal Pt(100) surfaces.

To demonstrate the capability of the NEP approach in modeling surface reconstruction, here we construct a NEP model based on the existing training dataset.<sup>170</sup> As a hindsight, we augmented the dataset by 300 liquid structures sampled from 3000 K to 8000 K via *ab initio* MD to enhance its structural diversity. The `nep.in` input file reads:

```

type          Pt
version       4
cutoff        6 5
n_max         4 4
basis_size    8 8
l_max         4 2 1
neuron        80
lambda_1      0.0
lambda_e      1.0
lambda_f      1.0
lambda_v      0.1
batch         5000
population    100
generation    200000

```

The parity plots for energy, force, and stress between NEP and DFT results are presented in Fig. 20 (a–c). The energy and force RMSEs on the test dataset are  $7.76$  meV atom<sup>-1</sup> and  $145.46$  meV Å<sup>-1</sup>, respectively. These RMSEs are relatively higher than those reported for the previous DP model,<sup>170</sup> which can be partly attributed to the inclusion of liquid structures in our training dataset, which have relatively large forces and thus lead to higher fitting errors.

Subsequently, we constructed an eight-atom-thick Pt(001) slab with an  $(80 \times 80)$  unit cell (51200 atoms) in the in-plane directions and performed MD simulations at 800 K. The energy profile and in-plane CN of the surface during the simulation are presented in Fig. 20 (d–e). During the initial 1 ns, we observed significant deformations of the surface atoms, accompanied by an increase in energy. During this stage, the four-fold coordinated atoms (CN = 4) remain dominant, and no surface reconstruction occurs. At approximately 2 ns, the ratio of four-fold coordinated atoms start to decrease, while the ratio of six-fold coordinated atoms (CN = 6) start to increase, accompanied by a decrease in energy. This suggests the formation of an irreversible hexagonal structure. Subsequently, the hexagonal pattern rapidly propagates across the entire surface, and subsurface layers are exposed due

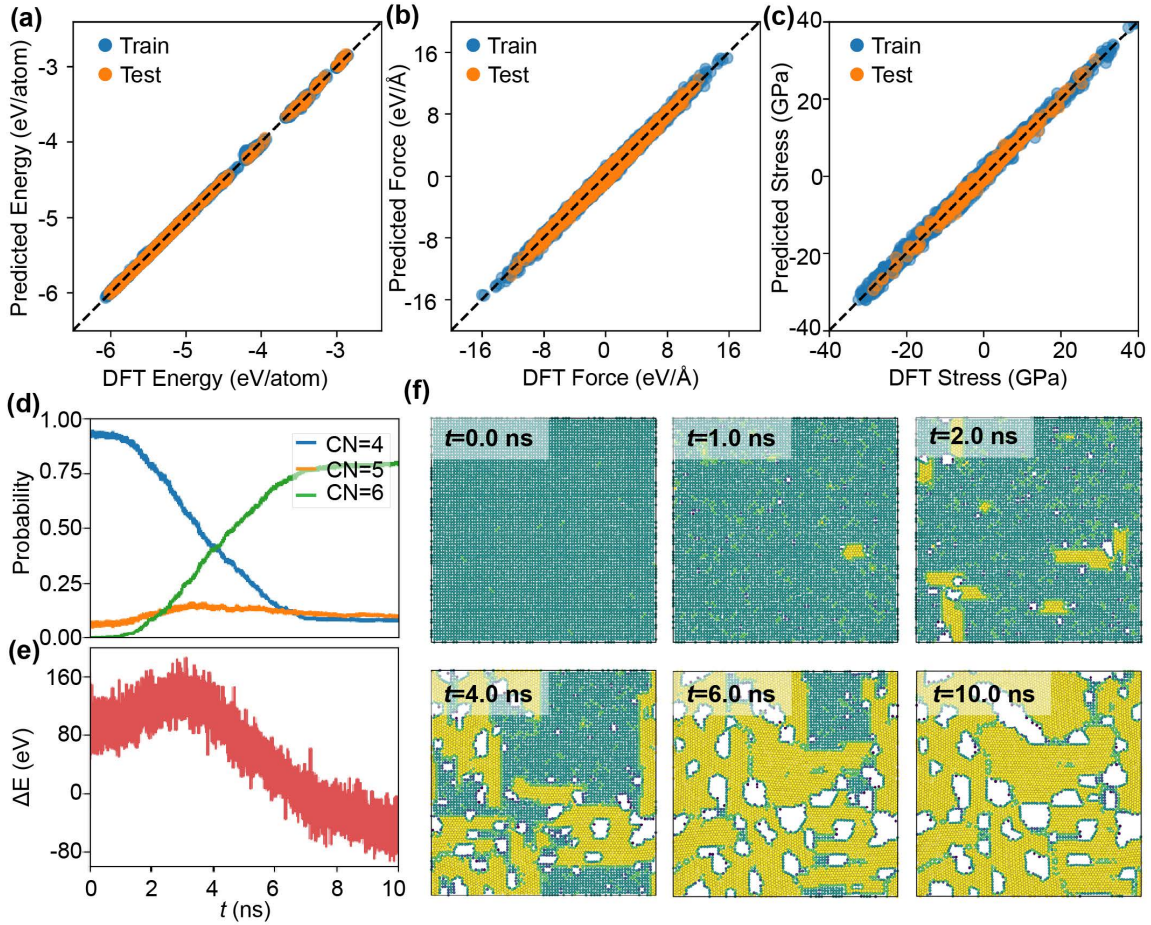


FIG. 20. Training and molecular dynamics simulation results of the neuroevolution potential (NEP) model for simulating the kinetic process of Pt surface reconstruction. (a–c) Parity plots comparing the NEP predictions with density functional theory (DFT) results for (a) energy, (b) atomic forces, and (c) stress. (d–e) Evolution of the in-plane coordination number (CN) for surface atoms and the corresponding energy difference profile of the system during the simulation. (f) Atomic structures of the Pt(100) surface at different stages of the simulation. Green and yellow spheres represent atoms with CNs 4 and 6, respectively, while blank regions indicate vacancies formed due to surface shrinkage during reconstruction.

to surface shrinkage, as illustrated in Fig. 20 (f). These findings are consistent with those obtained using the DP approach.<sup>170</sup>

Notably, the entire 10 ns simulation was completed in just 3.8 hours on a single GeForce RTX 4090 GPU, achieving a processing speed of approximately  $1.9 \times 10^7$  atom step second<sup>-1</sup>. This demonstrates the exceptional computational efficiency of the NEP approach for large-scale simulations of complex surface dynamics, enabling the exploration of phenomena that were previously computationally prohibitive.

### C. Case study: Theory-guided synthesis and growth of materials

The synthesis and growth of materials involve numerous chemical bond-breaking and bond-forming processes. Reliable description of these complex process are usually

beyond the capability of empirical potentials and MLPs have found important applications in modeling materials growth.<sup>93,163,171,172</sup>

Single-walled CNT possess remarkable fundamental properties, rendering them attractive for a broad range of applications.<sup>173,174</sup> CNTs are quasi-one-dimensional  $sp^2$ -hybridized carbon materials that are typically grown on catalyst surfaces at elevated temperatures.<sup>175–179</sup> The growth process of CNT involves complex kinetic phenomena, including the diffusion of carbon atoms on the catalyst surface, nucleation, and the formation and healing of structural defects.<sup>180–182</sup> These defects, which may arise during the growth process, can significantly influence the properties of CNTs, such as their mechanical, electrical, and thermal characteristics. Understanding and controlling these kinetic processes and defect dynamics are crucial for tailoring CNTs with desired properties for specific applications.

In the following, we demonstrate the application of



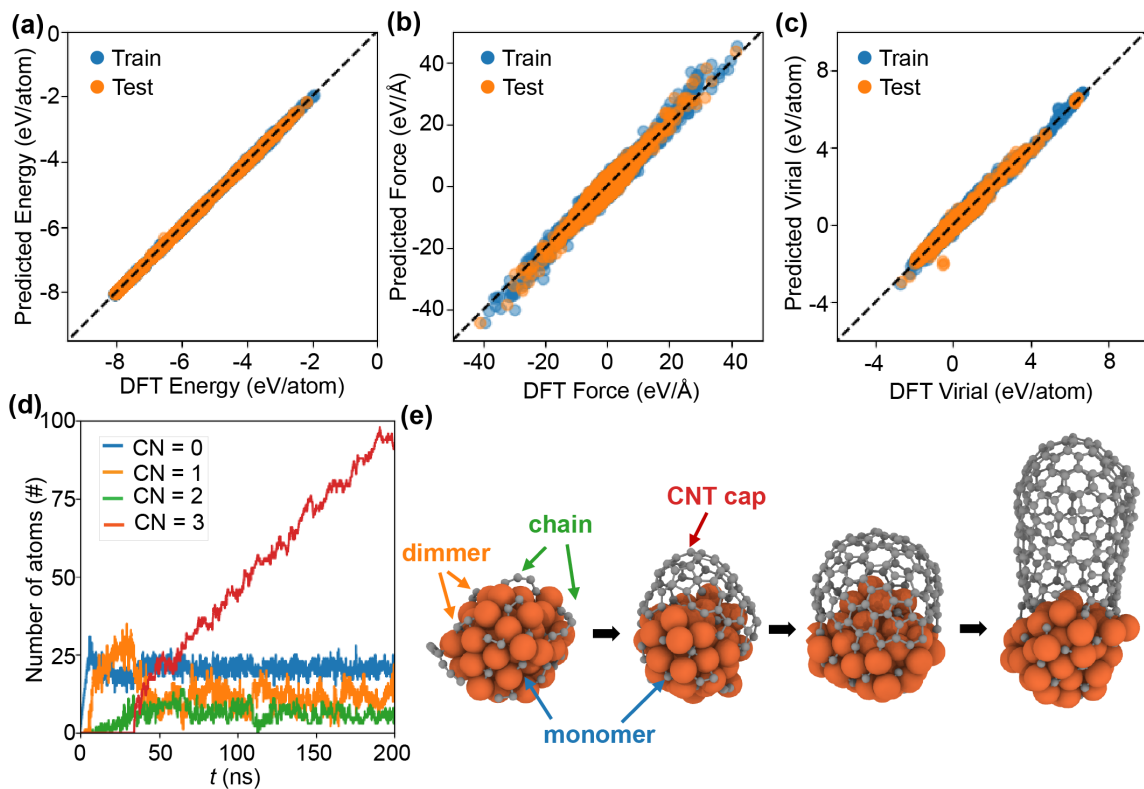


FIG. 21. Training and molecular dynamics simulation results of the NEP model for simulating CNT growth on the  $\text{Fe}_{55}$  catalyst. (a-c) Parity plots comparing the NEP predictions with DFT results for (a) energy, (b) atomic forces, and (c) virial. (d) Statistical distribution of carbon atoms during the CNT growth simulation. (e) Snapshot of the CNT growth process, illustrating the dynamic evolution of carbon structures on the  $\text{Fe}_{55}$  catalyst surface.

NEP approach to simulate the growth kinetics of CNTs on an  $\text{Fe}_{55}$  cluster using LAMMPS<sup>85</sup> interfaced with the NEP\_CPU package (Table II). To achieve this, we trained a NEP model for FeC systems, utilizing the same dataset used by Hedman *et al.*<sup>171</sup> The `nep.in` input file reads:

```

type          Fe C
version       4
cutoff        6 5
n_max         8 8
basis_size    8 8
l_max         4 2 0
neuron        30
lambda_1      0.05
lambda_2      0.05
lambda_e      1.0
lambda_f      1.0
lambda_v      0.1
batch         5000
population    50
generation    200000

```

As shown in the parity plots in Fig. 21 (a-c), the trained FeC NEP model shows good accuracy, achieving RMSEs of  $13.1 \text{ meV atom}^{-1}$  for energy,  $384.8 \text{ meV \AA}^{-1}$  for force, and  $77.2 \text{ meV atom}^{-1}$  for virial.

Throughout the CNT growth simulation, a time step

of 2.0 fs was used (to be consistent with the previous work,<sup>171</sup>) and the temperature was maintained at 1300 K. To simulate the growth of a CNT on the  $\text{Fe}_{55}$  catalyst, carbon atoms were introduced into the center of the  $\text{Fe}_{55}$  cluster at a rate of adding one carbon atom per nanosecond. The C-C coordination was carefully monitored to quantify and analyze the growth dynamics, providing a comprehensive understanding of the atomic-scale processes involved in CNT formation.

As shown in Fig. 21(e), during the initial 25 ns, the primary components on the surface of the  $\text{Fe}_{55}$  catalyst are carbon monomers (CN = 0) and carbon dimers (CN = 1). Starting from 25 ns, as carbon atoms diffuse on the surface of the  $\text{Fe}_{55}$  catalyst, carbon monomers and dimers gradually fuse to form carbon chains (CN = 2) and CNT caps (CN = 3), as illustrated in Fig. 21(f). This process is accompanied by a rapid decrease in the number of carbon monomers and dimers, highlighting the dynamic transformation of small carbon clusters into larger, more stable structures during the initial stages of CNT growth.

Following the formation of the cap, the CNT undergoes continuous growth. During this process, the populations of carbon monomers, dimers, and chains on the Fe catalyst surface maintain a dynamic equilibrium. Additionally, the kinetic process of carbon atoms diffusing

from the distal end of the catalyst to the CNT-Fe<sub>55</sub> interface can be observed. These carbon atoms attach to the CNT edge, enabling further growth. This provides atomic-scale insights into the CNT growth mechanism.

This example demonstrates the applicability of the NEP approach in material synthesis simulations. The NEP model accurately captures the atomic-scale dynamics of CNT growth on the Fe<sub>55</sub> catalyst, reproducing material growth interfaces that closely resembles real-world processes. By capturing key details such as carbon diffusion, cluster formation, and CNT growth, the NEP approach proves to be a powerful tool, enabling the study and prediction of complex material synthesis phenomena with high fidelity.

#### D. Primary radiation damage

Simulating collision cascades and radiation damage has long posed a challenge for existing interatomic potentials, both in terms of accuracy and efficiency. The highly efficient NEP approach offers a promising solution to this challenge. Accurate characterization of short-range repulsive forces is crucial for simulating early-stage primary radiation damage formation processes. The Ziegler-Biersack-Littmark (ZBL) screened nuclear repulsion potential<sup>183</sup> has been extensively validated to accurately describe the short-range interactions. To this end, NEP has been combined with ZBL to form a NEP-ZBL approach.<sup>15</sup> The total site energy  $U_i$  for atom  $i$  in the NEP-ZBL approach is

$$U_i = U_i^{\text{NEP}}(\mathbf{q}^i) + \frac{1}{2} \sum_{j \neq i} U^{\text{ZBL}}(r_{ij}).$$

The pairwise ZBL energy is

$$U^{\text{ZBL}}(r_{ij}) = \frac{1}{4\pi\epsilon_0} \frac{Z_i Z_j e^2}{r_{ij}^2} \phi(r_{ij}/a) f_c(r_{ij}).$$

Here,  $\epsilon_0$  is the vacuum dielectric constant and  $Z_i e$  is the nuclear charge of atom  $i$ . The cutoff function  $f_c(r_{ij})$  is similar to that defined in the Tersoff potential,<sup>5</sup> with the inner cutoff radius being half of the outer one. The outer cutoff is usually shorter than the nearest-neighbor distance in bulk materials. Therefore, all near-equilibrium properties are left to the NEP term while the ZBL term ensures a realistic repulsion when atoms are very close to each other. It is beneficial to include some training structures that contain relatively short interatomic distances, such as dimers, to ensure a smooth and accurate transition from near-equilibrium distances to the ZBL-relevant distances. Another efficient MLP approach, tabGAP,<sup>148</sup> has also been used for performing large-scale radiation damage and related simulations.<sup>184</sup>

Using the NEP-ZBL approach, Liu *et al.*<sup>15</sup> performed large-scale molecular dynamics simulations with up to 8.1 million atoms and 240 ps (using a single 40-GB A100

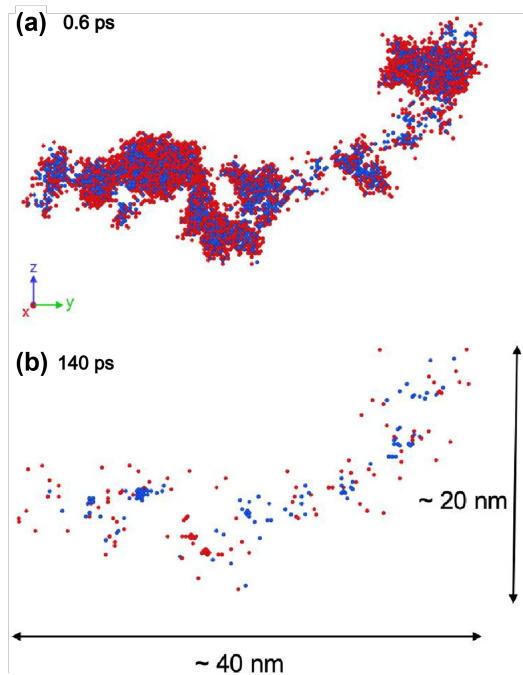


FIG. 22. Defect distributions in MoTaVW alloy during a radiation damage process. Defect snapshots of a cascade in a MoTaVW alloy at (a) the peak damage state (at about 0.6 ps) and (b) the final damage state (at 120 ps). The red and blue dots represent interstitial atoms and vacancies, respectively. Adapted with permission from Song *et al.*<sup>33</sup>, Nat. Commun. **15**, 10208 (2024).

GPU) to study the differences of primary radiation damage in bulk and thin-foil tungsten. Their findings for bulk tungsten are consistent with existing results simulated by embedded-atom method models, but the radiation damage differs significantly from embedded-atom method results in foils, showing that larger and more vacancy clusters as well as smaller and fewer interstitial clusters are produced due to the presence of a free surface, agreeing better with experimental findings.

In a recent application of the NEP-ZBL approach, Song *et al.* performed large-scale MD simulations of primary radiation damage in a MoTaVW alloy system using the UNEP-v1 model. Figure 22(a) shows the defect snapshot of the peak-damage state formed at about 0.6 ps with a primary knock-on atom energy of 100 keV. The defect distribution stabilizes after a few tens of ps. Figure 22(b) shows the stable defect distribution at 140 ps, revealing 121 residual point defects, including vacancies and interstitial atoms. The maximum cluster sizes for vacancies and interstitials are 15 and 11, respectively. In comparison, the previous study<sup>15</sup> on elemental tungsten at similar simulation conditions reported 183 residual point defects with a maximum defect-cluster size exceeding 200 atoms. The MoTaVW alloy thus features fewer defects and smaller defect clusters. The simulation results are consistent with the experimental study of a similar tungsten-based refractory high-entropy alloys,

which exhibits exceptional radiation resistance, negligible radiation hardening, and no evidence of radiation-induced dislocation loops even at a high dose level.<sup>185</sup>

In a more recent study, Liu *et al.*<sup>42</sup> constructed a NEP-ZBL model for the MoNbTaVW quinary system. They performed a series of displacement cascade simulations at primary knock-on atom energies ranging from 10 to 150 keV, revealing significant differences in defect generation and clustering between MoNbTaVW alloy and pure W. In the MoNbTaVW alloy, they observe more surviving Frenkel pairs but fewer and smaller interstitial clusters compared to W, indicating superior radiation tolerance. They proposed extended damage models to quantify the radiation dose in the MoNbTaVW alloy, and suggested that one reason for their enhanced resistance is sub-cascade splitting, which reduces the formation of interstitial clusters.

These studies showcase the capability of the NEP approach to simulate collision cascades and radiation damage, providing critical insights into the fundamental irradiation resistance mechanisms in elemental materials and high-entropy alloys, and offering guidance for the design of future radiation-tolerant materials.

## E. Summary

This section discussed the applications of the NEP approach in simulating various phase transitions and structural evolutions. These include: crystal-to-crystal phase transitions in perovskites,<sup>11–13,40</sup> Sb-Te phase-changing materials,<sup>27</sup> and BN<sup>39</sup> driven by temperature change; crystal-to-crystal phase transitions in carbon systems<sup>14,16,25,30,37</sup> driven by external stress; surface reconstruction in Pt(001) slab, CNT growth on Fe catalyst, and defect creation under primary radiation damage simulation of tungsten<sup>15</sup> and tungsten-based alloys.<sup>42</sup> Among these applications, surface reconstruction in Pt(001) slab and CNT growth on Fe catalyst are new case studies, demonstrating the versatility of the NEP approach.

The phase transitions discussed in this section connect to both the previous and the next sections. Earlier, the nanoporous and amorphous carbon structures were generated from the liquid phase, while some phase transitions mentioned in this section involve external mechanical stimuli. Overall, these results highlight the NEP approach as an efficient and powerful tool for large-scale atomistic simulations under diverse physical conditions. This capability positions it as a valuable method for studying the mechanical properties of various materials, which will be the focus of the next section.

## VI. MECHANICAL PROPERTIES

### A. Mechanical properties of 2D materials

*Ab initio* simulations provide accurate predictions of the mechanical properties of two-dimensional (2D) materials but are constrained by their high computational cost, limiting their application to small systems and short timescales. To address these limitations, MD simulations driven by traditional force fields have been extensively employed to investigate the mechanical behavior of 2D materials.<sup>186</sup> However, developing a reliable traditional force field to accurately describe the fracture properties of 2D materials remains challenging,<sup>93</sup> as it requires careful parametrization to describe the dynamic bond formation and rupture that occur during mechanical loading. Recently, MLP-based MD has emerged as a promising approach, bypassing the need for explicit physical expressions to describe specific interactions by directly translating *ab initio* data into classical interatomic forces.<sup>187</sup>

For instance, Wang *et al.*<sup>35</sup> utilized NEP-based MD to investigate the elastic properties of monolayer covalent organic frameworks at finite temperatures via the strain-fluctuation method.<sup>188</sup> Their extensive MD simulations revealed that all elastic constants of monolayer covalent organic frameworks at room temperature are significantly lower than those at zero temperature, a reduction attributed to thermal softening caused by out-of-plane ripple configurations.

Beyond thermoelastic properties, the NEP-based MD approach has also been employed to study the fracture behaviors of 2D materials, including the recently synthesized quasi-hexagonal-phase fullerene<sup>21</sup> and the widely studied hexagonal boron nitride<sup>36</sup> (Fig. 23). For monolayers of quasi-hexagonal-phase fullerene, simulations revealed a significantly smaller fracture strain compared to other 2D carbon allotropes,<sup>21</sup> attributed to inhomogeneous deformation between the rigid buckyballs and the softer inter-fullerene bonds (Fig. 23(a)). Similarly, NEP-based MD simulations for hexagonal boron nitride demonstrated that strong anisotropy in edge energy favors bifurcated cracks, contributing to intrinsic toughening as observed in experiments<sup>189</sup> (Fig. 23(b)).

In addition to quasi-hexagonal-phase fullerene, several studies have utilized traditional force fields<sup>190–194</sup> or a general-purpose MLP<sup>195</sup> to calculate the mechanical properties of quasi-tetragonal-phase fullerene, another single-crystal fullerene polymer.<sup>196</sup> Although this phase has been shown to be unstable in monolayer form both experimentally<sup>196</sup> and theoretically,<sup>21,197</sup> these studies predicted that it could remain stable at finite temperatures up to thousands of kelvin.<sup>190</sup> This discrepancy highlights the limitations of traditional force fields or general-purpose MLPs in accurately predicting the thermodynamic properties of newly synthesized 2D materials, as these force fields are not specifically parametrized or not accurate enough for fullerene-based carbon materials.

Besides the required accuracy of force fields in cap-



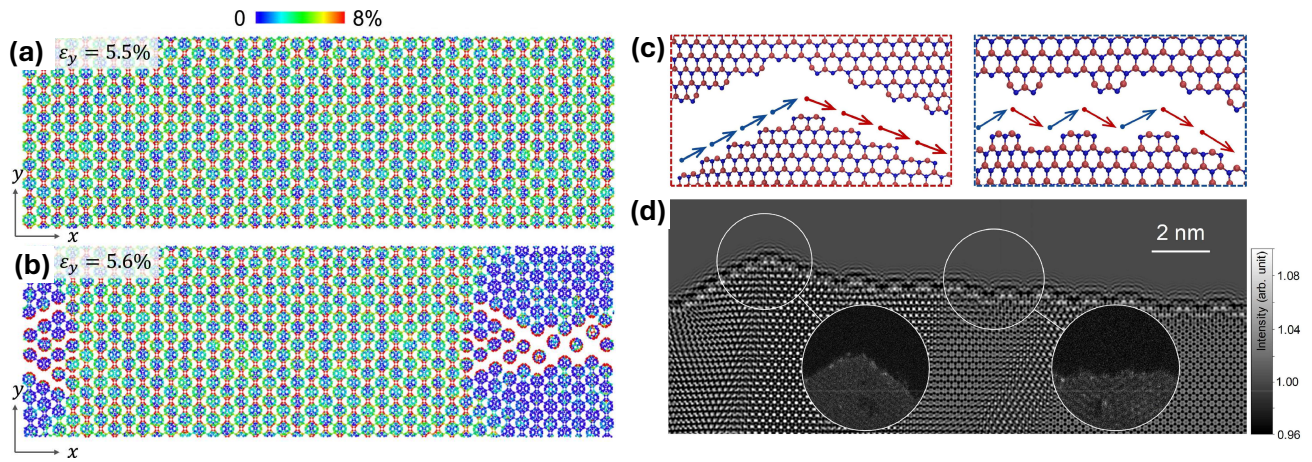


FIG. 23. Mechanical properties two-dimensional materials. (a-b) Atomic snapshots of monolayer quasi-hexagonal-phase fullerene sampled at specific strains (a) before and (b) after fracture under uniaxial tensile simulation at 100 K using a neuroevolution potential (ENP) model<sup>21</sup>. The atoms in the snapshots are colored based on their atomic volumetric strain. Reproduced with permission from Ying *et al.*,<sup>21</sup> *Extreme Mech. Lett.* **58**, 101929 (2023). Copyright 2023 Elsevier. (c) Atomic snapshots in hexagonal BN from molecular dynamics simulations using a NEP model<sup>36</sup> and (d) simulated high-resolution transmission electron microscope image of crack morphologies. Reproduced with permission from Yu *et al.*,<sup>36</sup> *J. Mech. Phys. Solids* **186**, 105579 (2024). Copyright 2024 Elsevier.

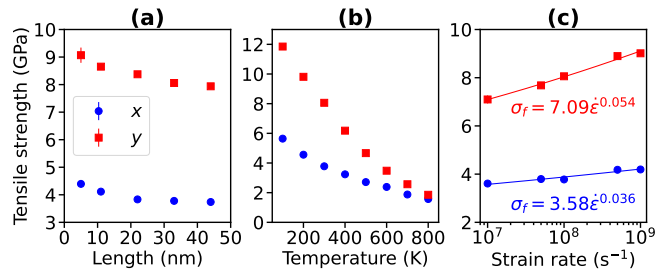


FIG. 24. Tensile strength of monolayer quasi-hexagonal-phase fullerene as a function of (a) system size, (b) temperature, and (c) strain rate. Adapted with permission from Ying *et al.*,<sup>21</sup> *Extreme Mech. Lett.* **58**, 101929 (2023). Copyright 2023 Elsevier.

turing the high-dimensional potential energy surface, the simulation setup is critical for reliably modeling the mechanical properties of 2D materials. The stochastic nature of dynamic bond breaking and formation during complex fracture processes<sup>198,199</sup> necessitates multiple independent simulations to adequately sample the phase space. Typically, several to tens of independent simulations are conducted to average mechanical properties, such as fracture strain and stress, and calculate the corresponding standard error of the mean. The required number of simulations can be determined by ensuring the ratio between the standard error and the average value falls below a specified threshold, such as 5%. Given the inherent limitations of system size and timescale in MD methodology, most studies use periodic boundary conditions to model extended 2D systems under very high strain rates. However, this setup can only pre-

dict mechanical properties under a single, specific condition, which may deviate significantly from real-world scenarios. In a recent study, utilizing the NEP approach, Ying *et al.*<sup>21</sup> comprehensively investigated the dependence of mechanical properties (including Young’s modulus, fracture strain, and fracture stress) of monolayer quasi-hexagonal-phase fullerene on system length, temperature, and strain rate. As shown in Fig. 24, tensile strength decreases with increasing system length, eventually converging when the length exceeds 40 nm (approximately 100,000 atoms). Additionally, as the temperature rises from 100 K to 800 K, tensile strength exhibits a three- to six-fold reduction, depending on the specific tensile direction (Fig. 24(b)). Regarding strain rate, tensile strength demonstrates a logarithmic dependence,<sup>200</sup> which may be extrapolated to quasi-static tensile strength as the strain rate approaches zero. These findings highlight the necessity of accounting for system size, finite temperature, and strain rate effects to achieve reliable predictions on mechanical properties of 2D materials under realistic conditions. The comprehensive investigations also showcase the effectiveness and accuracy of the NEP approach in determining the mechanical properties of 2D materials in realistic situations.

## B. Case study: Nanoscale tribology

When two rigid, weakly interacting, and clean crystalline surfaces are stacked in an incommensurate configuration<sup>201</sup>, the interfacial friction approaches zero, with friction coefficients below  $10^{-3}$ .<sup>202</sup> This phenomenon, known as structural superlubricity, arises from

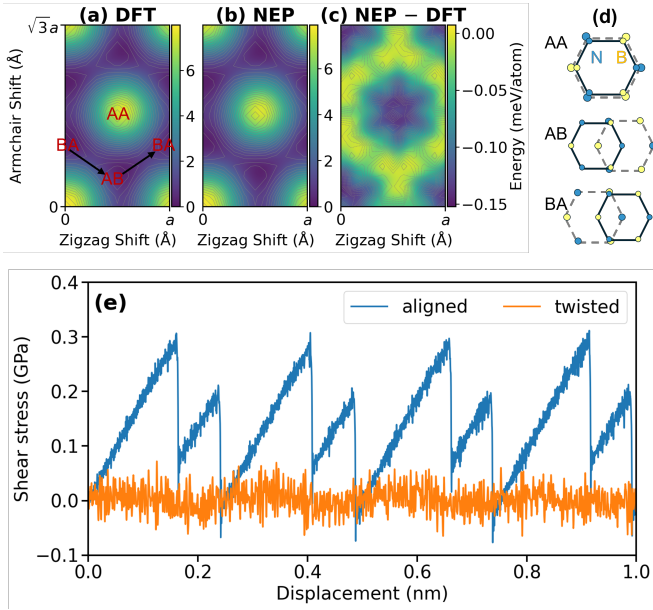


FIG. 25. (a-d) Sliding potential energy surfaces for bilayer hexagonal BN, as predicted by (a) density functional theory (DFT) and (b) neuroevolution potential (NEP) as well as (c) their difference (right). (d) The AA, AB, and BA stacking modes, whose positions are marked on the DFT potential energy surfaces map. (e) Shear stress traces for aligned and twisted hexagonal BN bilayers at a temperature of 300 K.

the effective cancellation of lateral forces.<sup>203</sup> Incommensurate interfaces can be achieved through intrinsic lattice mismatches between the contacting surfaces of heterostructures, such as graphene/hexagonal-BN<sup>204</sup>, or by introducing twists in homogeneous bilayers.<sup>205</sup> From a theoretical perspective, accurately modeling the sliding dynamics of both incommensurate and commensurate interfaces requires the development of a force field capable of capturing the sliding potential energy surfaces. This is particularly challenging, as the energy corrugation for sliding in 2D material interfaces is exceptionally shallow, typically on the order of only a few  $\text{meV atom}^{-1}$ .

Unlike traditional hybrid approaches that use separate potential models to describe interlayer and intralayer interactions,<sup>206</sup> MLP provides a unified framework to capture all interactions. Notably, NEP-driven MD simulations have been employed to compare the friction coefficients of three heterostructures: graphene/MoS<sub>2</sub>, graphene/PdSe<sub>2</sub>, and MoS<sub>2</sub>/PdSe<sub>2</sub>, showing alignment with experimental measurements.<sup>32</sup> Here, we use parallel-stacked bilayer hexagonal BN as an example to demonstrate the workflow for nanoscale tribology simulations, focusing on the sliding dynamics.

We use the NEP model developed in Sec. II B 7 to perform sliding dynamics simulations at a temperature of 300 K. Beyond the RMSE values, we compared the rigid sliding potential energy surface of bilayer hexagonal BN at a fixed interlayer distance of 3.35 Å predicted by NEP with DFT results, as shown in Fig. 25(a-c). For

all stacking configurations, the deviations were found to be smaller than  $0.15 \text{ meV atom}^{-1}$ , demonstrating very high accuracy.

The MD simulations were performed using the LAMMPS package<sup>85</sup> interfaced with the NEP\_CPU package (Table II). We considered aligned (commensurate) and twisted (incommensurate, with a twist angle of  $3.89^\circ$ ) bilayer hexagonal BN. The system sizes for the aligned and twisted bilayers were  $6.5 \times 3.5 \text{ nm}^2$  and  $6.4 \times 3.7 \text{ nm}^2$ , respectively, containing 2496 and 2604 atoms. The atoms in the bottom layer were anchored to their original positions using harmonic springs with a stiffness of  $50 \text{ N m}^{-1}$ , while the top layer atoms were driven laterally along the zigzag direction by a rigid stage (a duplicate of the initial top layer structure) at a velocity of  $10 \text{ m s}^{-1}$  via springs of the same stiffness. Periodic boundary conditions were applied in the lateral directions, whereas free boundary conditions were used in the out-of-plane direction. As shown in Fig. 25(e), the shear stress traces for the aligned interface exhibit typical stick-slip patterns, arising from the corrugation along the BA-AB-BA sliding path (see Fig. 25(a)). In contrast, for the  $3.89^\circ$  twisted bilayer, NEP predicts extremely low shear stresses near zero, indicating the superlubric nature of the incommensurate interface.

### C. Case study: Mechanical properties of compositionally complex alloys

Compositionally complex alloys, which include medium- and high-entropy alloys, feature elements with diverse atomic radii and valence electron concentrations, differing mixing enthalpies, and various types of chemical bonds.<sup>207</sup> These alloys also offer substantial tunability in composition ratios and structural arrangements, presenting extensive potential for property enhancement in a vast design space.<sup>52,208–211</sup> Traditional alloy design relies on iterative experiments and theoretical studies. However, with the exponential growth in computational power and algorithmic advancements, conventional methods are rapidly being replaced by machine-learning-based approaches. Machine-learning models, typically developed using experimental or computational data, follow two main technical routes.

The first route establishes a mapping relationship between composition (or structure) and properties, such as fitting a model to predict mechanical properties like hardness from composition.<sup>212,213</sup> This approach enables efficient and accurate predictions of the mechanical properties of unknown compositions. The second route develops interatomic potential models for alloy systems, which, when combined with MD simulations, can describe diffusion and phase transformation processes, elucidate atomic occupancy and chemical ordering, and calculate stress distributions within structures. These analyses provide insights into the mechanical properties and underlying mechanisms of alloys.



MLP-based alloy computations can follow workflows similar to those of MD simulations using empirical potentials. For instance, tensile and compressive simulations can quantify strength and toughness,<sup>214,215</sup> indentation and scratching can measure friction and wear,<sup>216,217</sup> impact compression can reveal dynamic mechanical responses<sup>218</sup>, and cyclic loading can explore fatigue and fracture behaviors.<sup>219,220</sup>

In this section, we demonstrate the applicability of the NEP approach in studying the mechanical properties a compositionally complex alloy in polycrystalline form, using the UNEP-v1 model.<sup>33</sup>

Utilizing the UNEP-v1 model,<sup>33</sup> we conducted simulations of uniaxial compression, impact compression, and uniaxial fatigue on a polycrystalline random solid-solution alloy  $\text{Cu}_{0.7}\text{Mo}_{25}\text{Ta}_{29.6}\text{V}_{17}\text{W}_{27.7}$ . This compositionally complex alloy was chosen due to its experimentally reported average grain size of approximately 18 nm,<sup>221</sup> which falls within the accessible range for MD simulations. The common settings for these simulations include the following: (i) The lattice constant was set to 3.18 Å. A polycrystalline structure of pure Cu was modeled using the AtomsK software,<sup>222</sup> with elements randomly substituted to match the  $\text{Cu}_{0.7}\text{Mo}_{25}\text{Ta}_{29.6}\text{V}_{17}\text{W}_{27.7}$  composition. (ii) Partially overlapping atoms were removed to ensure a minimum interatomic distance of 1.2 Å, ensuring stability during simulations. (iii) Unless otherwise noted, for the isothermal-isobaric ensemble, we employed the stochastic cell rescaling<sup>223</sup> barostat and the Bussi-Donadio-Parrinello<sup>224</sup> thermostat. For the canonical ensemble, the Bussi-Donadio-Parrinello thermostat was used. Periodic boundary conditions were applied with zero external pressure, and the time step was set to 2 fs. (iv) The structural types of atoms were identified using the common neighbor analysis<sup>225</sup> module in the OVITO package,<sup>226</sup> and defects, dislocation lines, and dislocation density were analyzed using the dislocation analysis module.<sup>227</sup>

### 1. Uniaxial compression

Uniaxial compression is a simple and widely used method to evaluate the mechanical properties of alloys, allowing for the calculation of yield strength and yield strain and the analysis of atomic deformation mechanisms. The initial structure was a cubic cell of  $27.0 \times 27.0 \times 27.0 \text{ nm}^3$ , containing 10 grains with an average size of 12.5 nm and a total of 1 221 240 atoms. This structure was first equilibrated at 300 K for 20 ps under the isothermal-isobaric ensemble to release internal stresses. Subsequently, uniaxial compression was applied along the  $x$ -axis with a strain rate of  $2 \times 10^8 \text{ s}^{-1}$ , up to a maximum strain of 10%.

As shown in Fig. 26(a-b), common neighbor analysis revealed minimal changes in the body-centered cubic structure of the grains and the amorphous grain boundaries during compression. Dislocation analy-

sis in Fig. 26(c-d) similarly indicated that the shape, dislocation density, and distribution of defects remained stable, highlighting the structural stability of the  $\text{Cu}_{0.7}\text{Mo}_{25}\text{Ta}_{29.6}\text{V}_{17}\text{W}_{27.7}$  alloy. From the stress-strain curve in Fig. 26(e), the yield strength was determined to be 10.0 GPa, closely matching the experimental value of  $10.0 \pm 0.8 \text{ GPa}$ . Notably, Table IV demonstrates that the equilibrium lattice constant and Young’s modulus calculated using UNEP-v1 are consistent with both DFT results and experimental values, highlighting the accuracy of UNEP-v1 in describing the mechanical properties of this alloy.

TABLE IV. Comparison of yield strength ( $S$ ), equilibrium lattice constant ( $a$ ), and Young’s modulus values ( $E$ ) obtained from the first version of unified neuroevolution potential (UNEP-v1), experimental measurements, and density functional theory (DFT) calculations.

Methods	$S$ (GPa)	$a$ (Å)	$E$ (GPa)
Experiment	$10.0 \pm 0.8$	3.16	229
DFT	/	3.18	/
UNEP-v1	10.0	3.17	224

### 2. Impact compression

Impact resistance is a critical performance indicator for alloys, but understanding its mechanisms presents significant challenges. Experimental methods often struggle to capture transient phenomena during dynamic mechanical responses or to analyze underlying atomic mechanisms. MD simulations of impact compression can replicate certain experimental processes, offering valuable insights and data.<sup>228–231</sup> Here, we employed the momentum mirror method for impact compression simulations.<sup>232</sup> The initial structure was a rectangular box of  $120.0 \times 12.0 \times 12.0 \text{ nm}^3$ , containing 10 grains with an average size of 12.0 nm and a total of 1 072 311 atoms. The  $x$ -direction was set as a non-periodic boundary, and the system was equilibrated at 300 K for 20 ps under the isothermal-isobaric ensemble. A rectangular region, highlighted in brown in Fig. 27, was designated as a piston, with the atomic masses artificially set to a large value of  $10^{10} \text{ amu}$  to act as a momentum mirror. The piston moved uniformly along the  $x$ -axis at a velocity of  $1 \text{ km s}^{-1}$  for 10 ps.

During compression, as shown in Fig. 27, only a small fraction of the body-centered cubic structure transitioned to an amorphous phase, demonstrating the strong stability of the body-centered cubic structure. Near the piston, dislocations formed and propagated rightward with the piston’s movement, while the distant region remained unaffected. This behavior further confirms the exceptional stability of the  $\text{Cu}_{0.7}\text{Mo}_{25}\text{Ta}_{29.6}\text{V}_{17}\text{W}_{27.7}$  alloy. Among

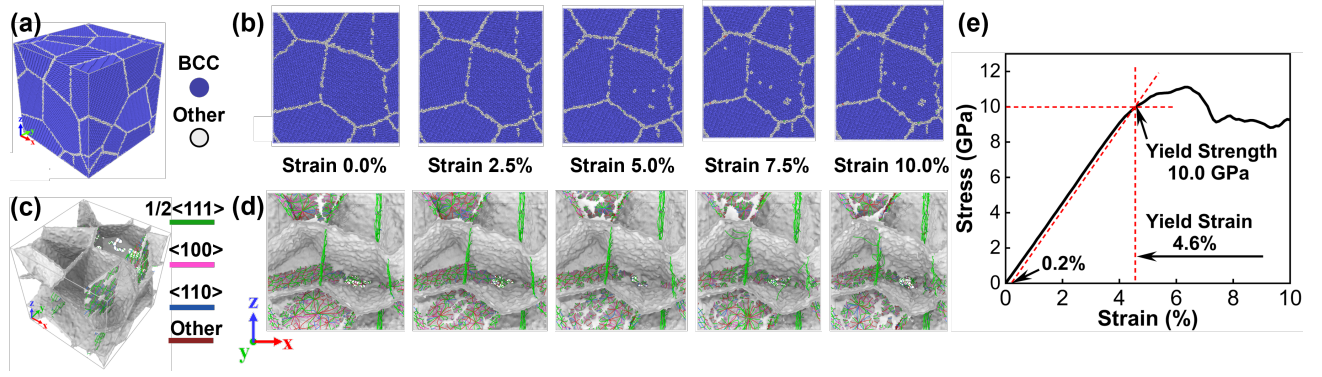


FIG. 26. Mechanical properties of  $\text{Cu}_{0.7}\text{Mo}_{25}\text{Ta}_{29.6}\text{V}_{17}\text{W}_{27.7}$  alloy under uniaxial compression. (a)-(b) Atomic structure types and (c)-(d) defects (gray regions) and dislocation line types in structures with different strain rates. (e) Stress-strain curve during the compression process.

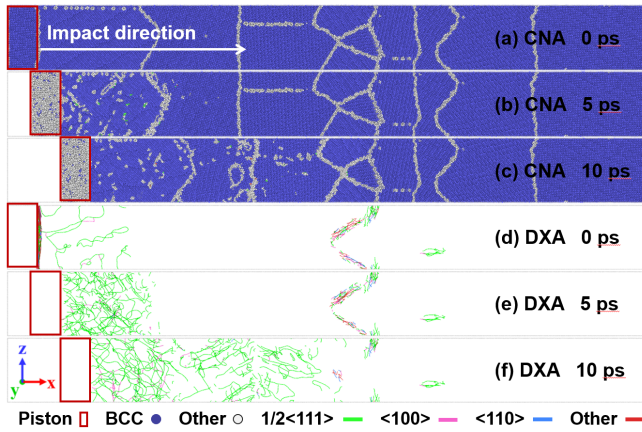


FIG. 27. (a-c) Atomic structure types at 0, 5, and 10 ps, and (d-f) dislocation line types at 0, 5, and 10 ps, obtained from the impact compression simulation of the  $\text{Cu}_{0.7}\text{Mo}_{25}\text{Ta}_{29.6}\text{V}_{17}\text{W}_{27.7}$  alloy.

the dislocations generated, the  $1/2\langle 111 \rangle$  dislocations were dominant, indicating that the primary deformation mechanism in polycrystalline  $\text{Cu}_{0.7}\text{Mo}_{25}\text{Ta}_{29.6}\text{V}_{17}\text{W}_{27.7}$  involves  $1/2\langle 111 \rangle$  dislocation slip.

### 3. Uniaxial fatigue

Fatigue and wear are the leading causes of failure in metal components.<sup>233</sup> The fatigue process includes thermomechanical and isothermal fatigue. Here, cyclic loading simulations were conducted to investigate the deformation behaviors and failure mechanisms of  $\text{Cu}_{0.7}\text{Mo}_{25}\text{Ta}_{29.6}\text{V}_{17}\text{W}_{27.7}$  under isothermal uniaxial fatigue.

The initial structure was a cubic box of  $21.1 \times 21.1 \times 21.1 \text{ nm}^3$ , containing 10 grains with an average size of approximately 9.8 nm and a total of 574 278 atoms. After equilibration at 300 K for 20 ps under the NPT ensemble, yield strain during compression and failure strain

during tension were determined. Based on these values, the maximum strain amplitude during cyclic loading was set to 6%.

A complete loading cycle involved stretching along the  $x$ -direction to a strain of 6%, restoring back and then compressing to a strain of -6%, and restoring back to the original length. Each cycle lasted 240 ps. Simulations were conducted for over 10 cycles, and the first 10 cycles were analyzed. Figure 28(a) illustrates the strain variations during two cycles. Figure 28(b) compares stress-strain curves for the 1st, 5th, and 10th cycles. The stress-strain curve of the 1st cycle starts at the origin, indicating that the structure was equilibrated. By the 10th cycle, the curve exhibited a slight clockwise rotation around the origin, indicating mechanical responses induced by cyclic loading. Figure 28(c) shows that  $1/2\langle 111 \rangle$  dislocations dominated dislocation density, consistent with observations from uniaxial and impact compression simulations.

Common neighbor analysis in Fig. 28(d-f) revealed minimal structural changes, with no significant alterations in body-centered cubic structures, grain boundary atoms, or dislocation core atoms. Moreover, no cracks or visible structural failures occurred. However, dislocation analysis in Fig. 28(g-i) showed noticeable defect fragmentation in grain boundary regions and increased dislocation density, while changes within grains remained minor. These results suggest localized atomic reconstructions at grain boundaries to accommodate stress during cyclic loading, while the grains maintained stability. Importantly, no cracks or significant structural failures were observed throughout the loading process.

### D. Summary

This section first reviewed the applications of the NEP approach in simulating mechanical properties of 2D materials, including monolayer quasi-hexagonal-phase fullerene<sup>21</sup> and hexagonal boron nitride.<sup>36</sup> Next, we demonstrated the applicability of the NEP approach in

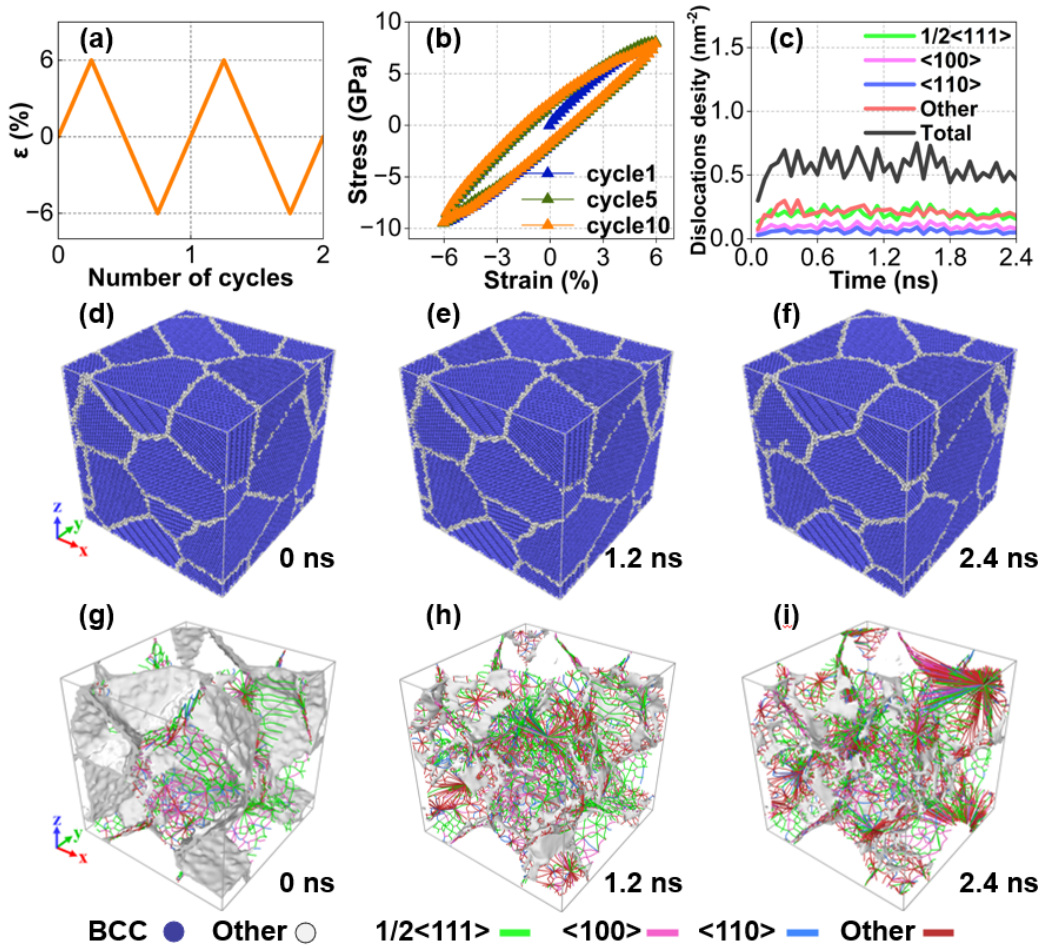


FIG. 28. Uniaxial fatigue simulation of the  $\text{Cu}_{0.7}\text{Mo}_{25}\text{Ta}_{29.6}\text{V}_{17}\text{W}_{27.7}$  alloy. (a) Strain-controlled cyclic loading along the  $x$ -axis, with a period of 240 ps and a maximum strain of 6%. (b) Stress-strain curves during cyclic loading for cycles 1, 5, and 10. (c) Variation in the density of typical dislocation types over 2.4 ns (10 cycles). (d-f) Atomic structures identified using the common neighbor analysis (CNA) method at 0, 1.2, and 2.4 ns, respectively. (g-i) Defects (gray regions) and dislocation lines identified using the dislocation extraction analysis (DXA) method at 0, 1.2, and 2.4 ns, respectively.

studying nanoscale tribology, utilizing a new NEP model for bilayer hexagonal boron nitride (Sec. II B 7). Finally, we investigated the mechanical behavior of compositionally complex alloys under various loading conditions, using the UNEP-v1 model.<sup>33</sup>

These applications demonstrate the effectiveness and accuracy of the NEP approach in determining the mechanical properties of diverse materials under realistic mechanical conditions, providing valuable insights. Notably, the UNEP-v1 model,<sup>33</sup> trained exclusively on elemental and binary metal structures, was successfully applied to a compositionally complex quinary alloy without any fine-tuning. This demonstrates its robustness and versatility as a ready-to-use model.

## VII. SUMMARY AND PERSPECTIVES

In this article, we comprehensively reviewed the neuroevolution potential (NEP) approach,<sup>9,33,61,62</sup> focusing on its applications in studying the structural, phase transitional, and mechanical properties of complex materials.

We began by discussing the foundational principles of general MLPs. Subsequently, we delved into both the theoretical foundations and practical implementations of the NEP approach. To provide a broader context for its performance, we compared NEP with various representative MLP approaches, including GAP,<sup>63</sup> DP,<sup>64</sup> NequIP,<sup>65</sup> and MACE.<sup>66</sup>, in terms of accuracy and speed. While some approaches achieve higher training accuracy, the NEP approach delivers competitive results for diverse physical properties and offers significantly higher computational efficiency, a crucial advantage for large-scale atomistic simulations. Thanks to its near-first-principle accuracy and empirical potential-like efficiency,



the NEP approach has been rapidly employed across a wide range of applications that require extensive spatiotemporal scales.

We have categorized the applications into three major topics: structural properties, phase transitions and related processes, and mechanical properties. Although these topics are often interconnected, this categorization helps in providing a clear structure for our discussion. For structural properties, NEP models have been developed to facilitate large-scale MD simulations or hybrid MC and MD simulations of various complex materials, including disordered carbon,<sup>44</sup> liquid water,<sup>45</sup> GeSn alloys,<sup>23</sup> compositionally complex alloys,<sup>33,43</sup> and many others. For phase transition and related processes, NEP models have played an important role in elucidating the temperature-driven phase transitions<sup>11–13</sup> and growth processes<sup>40</sup> in perovskite crystals and defect generation processes in tungsten<sup>15</sup> and tungsten-based alloys<sup>42</sup> under irradiation. For mechanical properties, the NEP approach has been used to study elastic constants in covalent organic frameworks<sup>35</sup> and fracture behaviour of fullerene-based monolayers<sup>21</sup> and hexagonal boron nitride<sup>36</sup> at finite temperatures.

Beyond reviewing existing applications enabled by NEP models, we have also provided several new examples to illustrate their applicability to a wider range of problems, showcasing the versatility of the NEP approach. By constructing NEP models utilizing prior training datasets in literature,<sup>170,171</sup> we demonstrated that consistent results can be obtained using the NEP approach for simulations like surface reconstruction in Pt(100) surfaces and CNT growth on iron clusters, much more efficient than previous studies<sup>170,171</sup> using the DP approach.<sup>64</sup>

Additionally, using a NEP model developed in this work, we also showcased the applicability of the NEP approach in studying nanoscale tribology, revealing the superlubric nature of twisted bilayer hexagonal boron nitride.

Lastly, using the UNEP-v1 model, we conducted a series of MD simulations to showcase applications in studying mechanical properties of compositionally complex alloys, under the conditions of quasi-static compression, shock compression, and cyclic loading.

All these existing and new studies have demonstrated the promising accuracy, efficiency, capability and versatility of the NEP approach in modeling complex materials. While we have only discussed structural, phase-transitional, and mechanical properties, the applicability range of the NEP approach is not limited to these. In particular, the NEP approach has been extensively applied to study heat transport<sup>59</sup> and has also started to find applications in ion transport.<sup>234</sup>

Despite that many successful applications have been achieved, the current NEP approach also has its limitations. For example, it does not have explicit charge degree of freedom, which could limit its usage in modeling physical properties and processes involving nontrivial (i.e., truly long-ranged) electrostatic interactions or

charge equilibrium. While message-passing constructions may effectively extend the interaction range, they cannot handle material interfaces with gaps wider than the cut-off radius within one message-passing layer. Constructions based on charge equilibrium, such as the fourth-generation high-dimensional neural network potential,<sup>74</sup> have been shown to be predictive. Recently, there are also proposals of incorporating long-range electrostatics without target atomic charges.<sup>235,236</sup> These are promising approaches that are worth exploring within the NEP formalism.

Another limitation of the NEP approach is the lack of a readily usable model for most materials. Such a model is usually called a large-atom model, or a foundation model. Currently, foundation models incorporating the major elements in the periodic table have been developed using several MLP approaches.<sup>149,237–239</sup> For the NEP approach, the development of the UNEP-v1 model,<sup>33</sup> applicable to 16 metals and their arbitrary alloys,<sup>33</sup> represents a significant step towards overcoming this limitation. Although the UNEP-v1 model currently considers a relatively small number of elements, focusing on elemental and binary systems for training data generation has proven to be a promising, data-efficient strategy. We expect that this approach, by generalizing to the entire periodic table, has the potential to significantly accelerate the development of a highly efficient large-atom model, enabling more accurate and cost-effective modeling of complex materials.

**Data availability:** All the training and test datasets, trained machine-learned potential models, and exemplary molecular dynamics input scripts are freely available at a zenodo repository.<sup>240</sup>

## ACKNOWLEDGMENTS

This work was supported by the National Science and Technology Innovation 2030 Major Program (No. 2024ZD0606900). PY was supported by the Israel Academy of Sciences and Humanities & Council for Higher Education Excellence Fellowship Program for International Postdoctoral Researchers.

## DECLARATION OF CONFLICT OF INTEREST

The authors have no conflicts to disclose.

## REFERENCES

- <sup>1</sup>J. A. Harrison, J. D. Schall, S. Maskey, P. T. Mikulski, M. T. Knippenberg, and B. H. Morrow, “Review of force fields and intermolecular potentials used in

- atomistic computational materials research,” *Applied Physics Reviews* **5**, 031104 (2018).
- <sup>2</sup>M. S. Daw and M. I. Baskes, “Embedded-atom method: Derivation and application to impurities, surfaces, and other defects in metals,” *Phys. Rev. B* **29**, 6443–6453 (1984).
  - <sup>3</sup>M. W. Finnis and J. E. Sinclair, “A simple empirical n-body potential for transition metals,” *Philosophical Magazine A* **50**, 45–55 (1984).
  - <sup>4</sup>F. H. Stillinger and T. A. Weber, “Computer simulation of local order in condensed phases of silicon,” *Phys. Rev. B* **31**, 5262–5271 (1985).
  - <sup>5</sup>J. Tersoff, “Empirical interatomic potential for carbon, with applications to amorphous carbon,” *Physical Review Letters* **61**, 2879 (1988).
  - <sup>6</sup>D. W. Brenner, O. A. Shenderova, J. A. Harrison, S. J. Stuart, B. Ni, and S. B. Sinnott, “A second-generation reactive empirical bond order (rebo) potential energy expression for hydrocarbons,” *Journal of Physics: Condensed Matter* **14**, 783 (2002).
  - <sup>7</sup>A. C. Van Duin, S. Dasgupta, F. Lorant, and W. A. Goddard, “ReaxFF: a reactive force field for hydrocarbons,” *The Journal of Physical Chemistry A* **105**, 9396–9409 (2001).
  - <sup>8</sup>J. Behler and M. Parrinello, “Generalized neural-network representation of high-dimensional potential-energy surfaces,” *Phys. Rev. Lett.* **98**, 146401 (2007).
  - <sup>9</sup>Z. Fan, Z. Zeng, C. Zhang, Y. Wang, K. Song, H. Dong, Y. Chen, and T. Ala-Nissila, “Neuroevolution machine learning potentials: Combining high accuracy and low cost in atomistic simulations and application to heat transport,” *Physical Review B* **104**, 104309 (2021).
  - <sup>10</sup>Z. Fan, W. Chen, V. Vierimaa, and A. Harju, “Efficient molecular dynamics simulations with many-body potentials on graphics processing units,” *Computer Physics Communications* **218**, 10–16 (2017).
  - <sup>11</sup>E. Fransson, P. Rosander, F. Eriksson, J. M. Rahm, T. Tadano, and P. Erhart, “Limits of the phonon quasi-particle picture at the cubic-to-tetragonal phase transition in halide perovskites,” *Communications Physics* **6**, 173 (2023).
  - <sup>12</sup>E. Fransson, J. Wiktor, and P. Erhart, “Phase transitions in inorganic halide perovskites from machine-learned potentials,” *The Journal of Physical Chemistry C* **127**, 13773–13781 (2023).
  - <sup>13</sup>E. Fransson, J. M. Rahm, J. Wiktor, and P. Erhart, “Revealing the free energy landscape of halide perovskites: Metastability and transition characters in cspbbr3 and mapbi3,” *Chemistry of Materials* **35**, 8229–8238 (2023).
  - <sup>14</sup>Y. Li and J.-W. Jiang, “Vacancy defects impede the transition from peapods to diamond: a neuroevolution machine learning study,” *Physical Chemistry Chemical Physics* **25**, 25629–25638 (2023).
  - <sup>15</sup>J. Liu, J. Byggmästar, Z. Fan, P. Qian, and Y. Su, “Large-scale machine-learning molecular dynamics simulation of primary radiation damage in tungsten,” *Phys. Rev. B* **108**, 054312 (2023).
  - <sup>16</sup>J. Shi, Z. Liang, J. Wang, S. Pan, C. Ding, Y. Wang, H.-T. Wang, D. Xing, and J. Sun, “Double-shock compression pathways from diamond to bc8 carbon,” *Physical review letters* **131**, 146101 (2023).
  - <sup>17</sup>Y.-B. Shi, Y.-Y. Chen, H. Wang, S. Cao, Y.-X. Zhu, M.-F. Chu, Z.-F. Shao, H.-K. Dong, and P. Qian, “Investigation of the mechanical and transport properties of InGeX<sub>3</sub> (X = S, Se and Te) monolayers using density functional theory and machine learning,” *Physical Chemistry Chemical Physics* **25**, 13864–13876 (2023).
  - <sup>18</sup>Y. Shi, Y. Chen, H. Dong, H. Wang, and P. Qian, “Investigation of phase transition, mechanical behavior and lattice thermal conductivity of halogen perovskites using machine learning interatomic potentials,” *Physical Chemistry Chemical Physics* **25**, 30644–30655 (2023).
  - <sup>19</sup>Y. Wang, Z. Fan, P. Qian, M. A. Caro, and T. Ala-Nissila, “Quantum-corrected thickness-dependent thermal conductivity in amorphous silicon predicted by machine learning molecular dynamics simulations,” *Phys. Rev. B* **107**, 054303 (2023).
  - <sup>20</sup>J. Wiktor, E. Fransson, D. Kubicki, and P. Erhart, “Quantifying dynamic tilting in halide perovskites: Chemical trends and local correlations,” *Chemistry of Materials* **35**, 6737–6744 (2023).
  - <sup>21</sup>P. Ying, H. Dong, T. Liang, Z. Fan, Z. Zhong, and J. Zhang, “Atomistic insights into the mechanical anisotropy and fragility of monolayer fullerene networks using quantum mechanical calculations and machine-learning molecular dynamics simulations,” *Extreme Mechanics Letters* **58**, 101929 (2023).
  - <sup>22</sup>R. Zhao, S. Wang, Z. Kong, Y. Xu, K. Fu, P. Peng, and C. Wu, “Development of a neuroevolution machine learning potential of Pd-Cu-Ni-P alloys,” *Materials & Design* **231**, 112012 (2023).
  - <sup>23</sup>S. Chen, X. Jin, W. Zhao, and T. Li, “Intricate short-range order in GeSn alloys revealed by atomistic simulations with highly accurate and efficient machine-learning potentials,” *Phys. Rev. Mater.* **8**, 043805 (2024).
  - <sup>24</sup>E. Fransson, J. Wiktor, and P. Erhart, “Impact of organic spacers and dimensionality on templating of halide perovskites,” *ACS Energy Letters* **9**, 3947–3954 (2024).
  - <sup>25</sup>G. Huang, L. Zhang, S. Chu, Y. Xie, and Y. Chen, “A highly ductile carbon material made of triangle rings: A study of machine learning,” *Applied Physics Letters* **124**, 043103 (2024).
  - <sup>26</sup>X. Huang, C. Li, M. Yuan, J. Shuai, X.-G. Li, and Y. Hou, “Unphysical grain size dependence of lattice thermal conductivity in Mg<sub>3</sub>(Sb, Bi)<sub>2</sub>: An atomistic view of concentration dependent segregation effects,” *Materials Today Physics* **43**, 101386 (2024).
  - <sup>27</sup>K. Li, B. Liu, J. Zhou, and Z. Sun, “Revealing the crystallization dynamics of Sb–Te phase change materials by large-scale simulations,” *J. Mater. Chem. C* **12**, 3897–3906 (2024).



- <sup>28</sup>Y. Liu, H. Meng, Z. Zhu, H. Yu, L. Zhuang, and Y. Chu, “Predicting mechanical and thermal properties of high-entropy ceramics via transferable machine-learning-potential-based molecular dynamics,” *Advanced Functional Materials* **n/a**, 2418802 (2024).
- <sup>29</sup>S. Lyu, R. Cheng, H. Li, and Y. Chen, “Effects of local chemical ordering on the thermal transport in entropy-regulated pbse-based thermoelectric materials,” *Applied Physics Letters* **124**, 232202 (2024).
- <sup>30</sup>S. Pan, J. Shi, Z. Liang, C. Liu, J. Wang, Y. Wang, H.-T. Wang, D. Xing, and J. Sun, “Shock compression pathways to pyrite silica from machine learning simulations,” *Phys. Rev. B* **110**, 224101 (2024).
- <sup>31</sup>Z. Qi, X. Sun, Z. Sun, Q. Wang, D. Zhang, K. Liang, R. Li, D. Zou, L. Li, G. Wu, *et al.*, “Interfacial optimization for AlN/diamond heterostructures via machine learning potential molecular dynamics investigation of the mechanical properties,” *ACS Applied Materials & Interfaces* **16**, 27998–28007 (2024).
- <sup>32</sup>G. Ru, W. Qi, S. Sun, K. Tang, C. Du, and W. Liu, “Interlayer friction and adhesion effects in Penta-PdSe<sub>2</sub>-based van der waals heterostructures,” *Advanced Science* **11**, 2400395 (2024).
- <sup>33</sup>K. Song, R. Zhao, J. Liu, Y. Wang, E. Lindgren, Y. Wang, S. Chen, K. Xu, T. Liang, P. Ying, N. Xu, Z. Zhao, J. Shi, J. Wang, S. Lyu, Z. Zeng, S. Liang, H. Dong, L. Sun, Y. Chen, Z. Zhang, W. Guo, P. Qian, J. Sun, P. Erhart, T. Ala-Nissila, Y. Su, and Z. Fan, “General-purpose machine-learned potential for 16 elemental metals and their alloys,” *Nature Communications* **15**, 10208 (2024).
- <sup>34</sup>B. Timalina, H. G. Nguyen, and K. Esfarjani, “Neuroevolution machine learning potential to study high temperature deformation of entropy-stabilized oxide MgNiCoCuZnO<sub>5</sub>,” *Journal of Applied Physics* **136**, 155109 (2024).
- <sup>35</sup>B. Wang, P. Ying, and J. Zhang, “The thermoelastic properties of monolayer covalent organic frameworks studied by machine-learning molecular dynamics,” *Nanoscale* **16**, 237–248 (2024).
- <sup>36</sup>M. Yu, Z. Zhao, W. Guo, and Z. Zhang, “Fracture toughness of two-dimensional materials dominated by edge energy anisotropy,” *Journal of the Mechanics and Physics of Solids* **186**, 105579 (2024).
- <sup>37</sup>L. Yu, K. Dong, Q. Yang, Y. Zhang, Z. Fan, X. Zheng, H. Wang, Z. Qin, and G. Qin, “Dynamic mesophase transition induces anomalous suppressed and anisotropic phonon thermal transport,” *NPJ Computational Materials* **10**, 1–10 (2024).
- <sup>38</sup>Z. Zhao, M. Yi, W. Guo, and Z. Zhang, “General-purpose neural network potential for Ti-Al-Nb alloys towards large-scale molecular dynamics with ab initio accuracy,” *Phys. Rev. B* **110**, 184115 (2024).
- <sup>39</sup>Y.-Q. Liu, H.-K. Dong, Y. Ren, W.-G. Zhang, and W. Chen, “Crystallization of h-bn by molecular dynamics simulation using a machine learning interatomic potential,” *Computational Materials Science* **249**, 113621 (2025).
- <sup>40</sup>P. Ahlawat, “Size dependent solid-solid crystallization of halide perovskites,” (2024), arXiv:2404.05644 [cond-mat.mtrl-sci].
- <sup>41</sup>S. Liu, S. Chen, X. Jin, J.-H. Bae, I. Bikmukhmetov, D. Jaeger, O. Concepcion, A. Covian, X. Wang, C. Cline, A. Akey, L. Vogl, H. Zhao, Y. Zeng, A. Minor, S.-Q. Yu, D. Buca, T. Li, and J. Liu, “Atomic short-range order in SiGeSn alloys,” (2024), Research Square, ISSN: 2693-5015.
- <sup>42</sup>J. Liu, J. Byggmatar, Z. Fan, B. Bai, P. Qian, and Y. Su, “Utilizing a machine-learned potential to explore enhanced radiation tolerance in the monbtavv high-entropy alloy,” (2024), arXiv:2411.02834 [cond-mat.mtrl-sci].
- <sup>43</sup>K. Song, J. Liu, S. Chen, Z. Fan, Y. Su, and P. Qian, “Solute segregation in polycrystalline aluminum from hybrid monte carlo and molecular dynamics simulations with a unified neuroevolution potential,” (2024), arXiv:2404.13694 [cond-mat.mtrl-sci].
- <sup>44</sup>Y. Wang, Z. Fan, P. Qian, M. A. Caro, and T. Ala-Nissila, “Density dependence of thermal conductivity in nanoporous and amorphous carbon with machine-learned molecular dynamics,” (2024), arXiv:2408.12390 [cond-mat.mtrl-sci].
- <sup>45</sup>K. Xu, T. Liang, N. Xu, P. Ying, S. Chen, N. Wei, J. Xu, and Z. Fan, “Nep-mb-pol: A unified machine-learned framework for fast and accurate prediction of water’s thermodynamic and transport properties,” (2024), arXiv:2411.09631 [physics.chem-ph].
- <sup>46</sup>L. Zhang, W. Luo, R. Liu, M. Chen, Z. Yan, and K. Cao, “Exploring the energy landscape of aluminas through machine learning interatomic potential,” (2024), arXiv:2412.02191 [cond-mat.mtrl-sci].
- <sup>47</sup>V. L. Deringer, M. A. Caro, and G. Csányi, “Machine learning interatomic potentials as emerging tools for materials science,” *Advanced Materials* **31**, 1902765 (2019).
- <sup>48</sup>J. Behler, “Four generations of high-dimensional neural network potentials,” *Chemical Reviews* **121**, 10037–10072 (2021).
- <sup>49</sup>A. M. Miksch, T. Morawietz, J. Kästner, A. Urban, and N. Artrith, “Strategies for the construction of machine-learning potentials for accurate and efficient atomic-scale simulations,” *Machine Learning: Science and Technology* **2**, 031001 (2021).
- <sup>50</sup>O. T. Unke, S. Chmiela, H. E. Sauceda, M. Gastegger, I. Poltavsky, K. T. Schütt, A. Tkatchenko, and K.-R. Müller, “Machine learning force fields,” *Chemical Reviews* **121**, 10142–10186 (2021).
- <sup>51</sup>P. Friederich, F. Häse, J. Proppe, and A. Aspuru-Guzik, “Machine-learned potentials for next-generation matter simulations,” *Nature Materials* **20**, 750–761 (2021).
- <sup>52</sup>Y. Mishin, “Machine-learning interatomic potentials for materials science,” *Acta Materialia* **214**, 116980 (2021).
- <sup>53</sup>T. Wen, L. Zhang, H. Wang, W. E, and D. J. Srolovitz, “Deep potentials for materials science,” *Ma-*

- terials Futures **1**, 022601 (2022).
- <sup>54</sup>A. M. Tokita and J. Behler, “How to train a neural network potential,” *The Journal of Chemical Physics* **159**, 121501 (2023).
- <sup>55</sup>S. Klawohn, J. P. Darby, J. R. Kermode, G. Csányi, M. A. Caro, and A. P. Bartók, “Gaussian approximation potentials: Theory, software implementation and application examples,” *The Journal of Chemical Physics* **159**, 174108 (2023).
- <sup>56</sup>S. Y. Willow, A. Hajibabaei, M. Ha, D. C. Yang, C. W. Myung, S. K. Min, G. Lee, and K. S. Kim, “Sparse gaussian process based machine learning first principles potentials for materials simulations: Application to batteries, solar cells, catalysts, and macromolecular systems,” *Chemical Physics Reviews* **5**, 041307 (2024).
- <sup>57</sup>G. Wang, C. Wang, X. Zhang, Z. Li, J. Zhou, and Z. Sun, “Machine learning interatomic potential: Bridge the gap between small-scale models and realistic device-scale simulations,” *iScience* **27**, 109673 (2024).
- <sup>58</sup>F. L. Thiemann, N. O’Neill, V. Kapil, A. Michaelides, and C. Schran, “Introduction to machine learning potentials for atomistic simulations,” *Journal of Physics: Condensed Matter* **37**, 073002 (2024).
- <sup>59</sup>H. Dong, Y. Shi, P. Ying, K. Xu, T. Liang, Y. Wang, Z. Zeng, X. Wu, W. Zhou, S. Xiong, S. Chen, and Z. Fan, “Molecular dynamics simulations of heat transport using machine-learned potentials: A mini-review and tutorial on gpumd with neuroevolution potentials,” *Journal of Applied Physics* **135**, 161101 (2024).
- <sup>60</sup>N. Xu, P. Rosander, C. Schäfer, E. Lindgren, N. Österbacka, M. Fang, W. Chen, Y. He, Z. Fan, and P. Erhart, “Tensorial properties via the neuroevolution potential framework: Fast simulation of infrared and raman spectra,” *Journal of Chemical Theory and Computation* **20**, 3273–3284 (2024).
- <sup>61</sup>Z. Fan, “Improving the accuracy of the neuroevolution machine learning potential for multi-component systems,” *Journal of Physics: Condensed Matter* **34**, 125902 (2022).
- <sup>62</sup>Z. Fan, Y. Wang, P. Ying, K. Song, J. Wang, Y. Wang, Z. Zeng, K. Xu, E. Lindgren, J. M. Rahm, *et al.*, “GPUMD: A package for constructing accurate machine-learned potentials and performing highly efficient atomistic simulations,” *The Journal of Chemical Physics* **157**, 114801 (2022).
- <sup>63</sup>A. P. Bartók, M. C. Payne, R. Kondor, and G. Csányi, “Gaussian approximation potentials: The accuracy of quantum mechanics, without the electrons,” *Physical Review Letters* **104**, 136403 (2010).
- <sup>64</sup>H. Wang, L. Zhang, J. Han, and E. Weinan, “DeepPMD-kit: A deep learning package for many-body potential energy representation and molecular dynamics,” *Computer Physics Communications* **228**, 178–184 (2018).
- <sup>65</sup>S. Batzner, A. Musaelian, L. Sun, M. Geiger, J. P. Mailoa, M. Kornbluth, N. Molinari, T. E. Smidt, and B. Kozinsky, “E(3)-equivariant graph neural networks for data-efficient and accurate interatomic potentials,” *Nature Communications* **13**, 2453 (2022).
- <sup>66</sup>I. Batatia, D. P. Kovacs, G. Simm, C. Ortner, and G. Csányi, “MACE: Higher order equivariant message passing neural networks for fast and accurate force fields,” *Advances in Neural Information Processing Systems* **35**, 11423–11436 (2022).
- <sup>67</sup>P. Rowe, V. L. Deringer, P. Gasparotto, G. Csányi, and A. Michaelides, “An accurate and transferable machine learning potential for carbon,” *The Journal of Chemical Physics* **153**, 034702 (2020).
- <sup>68</sup>J. Behler, “Atom-centered symmetry functions for constructing high-dimensional neural network potentials,” *The Journal of Chemical Physics* **134**, 074106 (2011).
- <sup>69</sup>A. P. Bartók, R. Kondor, and G. Csányi, “On representing chemical environments,” *Phys. Rev. B* **87**, 184115 (2013).
- <sup>70</sup>M. A. Caro, “Optimizing many-body atomic descriptors for enhanced computational performance of machine learning based interatomic potentials,” *Phys. Rev. B* **100**, 024112 (2019).
- <sup>71</sup>A. Thompson, L. Swiler, C. Trott, S. Foiles, and G. Tucker, “Spectral neighbor analysis method for automated generation of quantum-accurate interatomic potentials,” *Journal of Computational Physics* **285**, 316–330 (2015).
- <sup>72</sup>A. V. Shapeev, “Moment tensor potentials: A class of systematically improvable interatomic potentials,” *Multiscale Modeling & Simulation* **14**, 1153–1173 (2016).
- <sup>73</sup>R. Drautz, “Atomic cluster expansion for accurate and transferable interatomic potentials,” *Phys. Rev. B* **99**, 014104 (2019).
- <sup>74</sup>T. W. Ko, J. A. Finkler, S. Goedecker, and J. Behler, “A fourth-generation high-dimensional neural network potential with accurate electrostatics including non-local charge transfer,” *Nature Communications* **12**, 398 (2021).
- <sup>75</sup>K. T. Schütt, H. E. Sauceda, P.-J. Kindermans, A. Tkatchenko, and K.-R. Müller, “SchNet – A deep learning architecture for molecules and materials,” *The Journal of Chemical Physics* **148**, 241722 (2018).
- <sup>76</sup>Y. Zhang, J. Xia, and B. Jiang, “Physically motivated recursively embedded atom neural networks: Incorporating local completeness and nonlocality,” *Phys. Rev. Lett.* **127**, 156002 (2021).
- <sup>77</sup>J. Wang, Y. Wang, H. Zhang, Z. Yang, Z. Liang, J. Shi, H.-T. Wang, D. Xing, and J. Sun, “E(n)-equivariant cartesian tensor message passing interatomic potential,” *Nature Communications* **15**, 7607 (2024).
- <sup>78</sup>B. Cheng, “Cartesian atomic cluster expansion for machine learning interatomic potentials,” *npj Computational Materials* **10**, 157 (2024).
- <sup>79</sup>A. Bochkarev, Y. Lysogorskiy, and R. Drautz, “Graph atomic cluster expansion for semilocal interactions be-

- yond equivariant message passing,” *Phys. Rev. X* **14**, 021036 (2024).
- <sup>80</sup>F. Musil, A. Grisafi, A. P. Bartók, C. Ortner, G. Csányi, and M. Ceriotti, “Physics-inspired structural representations for molecules and materials,” *Chemical Reviews* **121**, 9759–9815 (2021).
- <sup>81</sup>M. F. Langer, A. Goeßmann, and M. Rupp, “Representations of molecules and materials for interpolation of quantum-mechanical simulations via machine learning,” *npj Computational Materials* **8**, 41 (2022).
- <sup>82</sup>T. Schaul, T. Glasmachers, and J. Schmidhuber, “High Dimensions and Heavy Tails for Natural Evolution Strategies,” in *Proceedings of the 13th Annual Conference on Genetic and Evolutionary Computation*, GECCO ’11 (Association for Computing Machinery, New York, NY, USA, 2011) pp. 845–852.
- <sup>83</sup>Z. Fan, L. F. C. Pereira, H.-Q. Wang, J.-C. Zheng, D. Donadio, and A. Harju, “Force and heat current formulas for many-body potentials in molecular dynamics simulations with applications to thermal conductivity calculations,” *Phys. Rev. B* **92**, 094301 (2015).
- <sup>84</sup>E. Lindgren, M. Rahm, E. Fransson, F. Eriksson, N. Österbacka, Z. Fan, and P. Erhart, “calorine: A Python package for constructing and sampling neuroevolution potential models,” *Journal of Open Source Software* **9**, 6264 (2024).
- <sup>85</sup>A. P. Thompson, H. M. Aktulga, R. Berger, D. S. Bolintineanu, W. M. Brown, P. S. Crozier, P. J. In’t Veld, A. Kohlmeyer, S. G. Moore, T. D. Nguyen, *et al.*, “LAMMPS—a flexible simulation tool for particle-based materials modeling at the atomic, meso, and continuum scales,” *Computer Physics Communications* **271**, 108171 (2022).
- <sup>86</sup>A. H. Larsen, J. J. Mortensen, J. Blomqvist, I. E. Castelli, R. Christensen, M. Dułak, J. Friis, M. N. Groves, B. Hammer, C. Hargus, *et al.*, “The atomic simulation environment—a python library for working with atoms,” *Journal of Physics: Condensed Matter* **29**, 273002 (2017).
- <sup>87</sup>W. Ouyang, D. Mandelli, M. Urbakh, and O. Hod, “Nanoserpents: Graphene nanoribbon motion on two-dimensional hexagonal materials,” *Nano letters* **18**, 6009–6016 (2018).
- <sup>88</sup>G. Kresse and J. Furthmüller, “Efficient iterative schemes for ab initio total-energy calculations using a plane-wave basis set,” *Physical review B* **54**, 11169 (1996).
- <sup>89</sup>G. Kresse and D. Joubert, “From ultrasoft pseudopotentials to the projector augmented-wave method,” *Physical review b* **59**, 1758 (1999).
- <sup>90</sup>J. P. Perdew, K. Burke, and M. Ernzerhof, “Generalized gradient approximation made simple,” *Physical review letters* **77**, 3865 (1996).
- <sup>91</sup>S. Grimme, S. Ehrlich, and L. Goerigk, “Effect of the damping function in dispersion corrected density functional theory,” *Journal of computational chemistry* **32**, 1456–1465 (2011).
- <sup>92</sup>Z. Fan, Y. Xiao, Y. Wang, P. Ying, S. Chen, and H. Dong, “Combining linear-scaling quantum transport and machine-learning molecular dynamics to study thermal and electronic transports in complex materials,” *Journal of Physics: Condensed Matter* **36**, 245901 (2024).
- <sup>93</sup>C. Qian, B. McLean, D. Hedman, and F. Ding, “A comprehensive assessment of empirical potentials for carbon materials,” *APL Materials* **9**, 061102 (2021).
- <sup>94</sup>P. Ying, A. Natan, O. Hod, and M. Urbakh, “Effect of interlayer bonding on superlubric sliding of graphene contacts: A machine-learning potential study,” *ACS nano* **18**, 10133–10141 (2024).
- <sup>95</sup>V. L. Deringer and G. Csányi, “Machine learning based interatomic potential for amorphous carbon,” *Physical Review B* **95**, 094203 (2017).
- <sup>96</sup>H. Muhli, X. Chen, A. P. Bartók, P. Hernández-León, G. Csányi, T. Ala-Nissila, and M. A. Caro, “Machine learning force fields based on local parametrization of dispersion interactions: Application to the phase diagram of C60,” *Physical Review B* **104**, 054106 (2021).
- <sup>97</sup>P. Fallon, V. Veerasamy, C. Davis, J. Robertson, G. Amaratunga, W. Milne, and J. Koskinen, “Properties of filtered-ion-beam-deposited diamondlike carbon as a function of ion energy,” *Physical Review B* **48**, 4777 (1993).
- <sup>98</sup>A. Ferrari, A. Libassi, B. Tanner, V. Stolojan, J. Yuan, L. Brown, S. Rodil, B. Kleinsorge, and J. Robertson, “Density,  $sp^3$  fraction, and cross-sectional structure of amorphous carbon films determined by X-ray reflectivity and electron energy-loss spectroscopy,” *Physical Review B* **62**, 11089 (2000).
- <sup>99</sup>G. Bussi and M. Parrinello, “Accurate sampling using Langevin dynamics,” *Physical Review E* **75**, 056707 (2007).
- <sup>100</sup>M. A. Caro, V. L. Deringer, J. Koskinen, T. Laurila, and G. Csányi, “Growth mechanism and origin of high  $sp^3$  content in tetrahedral amorphous carbon,” *Phys. Rev. Lett.* **120**, 166101 (2018).
- <sup>101</sup>X. Zhou, Y. Liu, B. Tang, J. Wang, H. Dong, X. Xiu, S. Chen, and Z. Fan, “Million-atom heat transport simulations of polycrystalline graphene approaching first-principles accuracy enabled by neuroevolution potential on desktop gpus,” *Journal of Applied Physics* **137**, 014305 (2025).
- <sup>102</sup>J. Liu, Q. Yin, M. He, and J. Zhou, “Constructing accurate machine-learned potentials and performing highly efficient atomistic simulations to predict structural and thermal properties,” (2024), [arXiv:2411.10911 \[cond-mat.mtrl-sci\]](https://arxiv.org/abs/2411.10911).
- <sup>103</sup>M. A. Caro, “Machine learning based modeling of disordered elemental semiconductors: understanding the atomic structure of a-Si and a-C,” *Semiconductor Science and Technology* **38**, 043001 (2023).
- <sup>104</sup>Y. Wang, Z. Fan, P. Qian, T. Ala-Nissila, and M. A. Caro, “Structure and pore size distribution in nanoporous carbon,” *Chemistry of Materials* **34**, 617–628 (2022).

- <sup>105</sup>Y. Lifshitz, “Diamond-like carbon – present status,” *Diamond and Related Materials* **8**, 1659–1676 (1999).
- <sup>106</sup>J. W. Martin, C. de Tomas, I. Suarez-Martinez, M. Kraft, and N. A. Marks, “Topology of disordered 3d graphene networks,” *Phys. Rev. Lett.* **123**, 116105 (2019).
- <sup>107</sup>L. B. Skinner, C. Huang, D. Schlesinger, L. G. M. Pettersson, A. Nilsson, and C. J. Benmore, “Benchmark oxygen-oxygen pair-distribution function of ambient water from x-ray diffraction measurements with a wide Q-range,” *The Journal of Chemical Physics* **138**, 074506 (2013).
- <sup>108</sup>A. Soper, “The radial distribution functions of water and ice from 220 to 673 K and at pressures up to 400 MPa,” *Chemical Physics* **258**, 121–137 (2000).
- <sup>109</sup>T. Morawietz, A. Singraber, C. Dellago, and J. Behler, “How van der Waals interactions determine the unique properties of water,” *Proceedings of the National Academy of Sciences* **113**, 8368–8373 (2016).
- <sup>110</sup>B. Cheng, J. Behler, and M. Ceriotti, “Nuclear quantum effects in water at the triple point: Using theory as a link between experiments,” *The Journal of Physical Chemistry Letters* **7**, 2210–2215 (2016).
- <sup>111</sup>B. Cheng, E. A. Engel, J. Behler, C. Dellago, and M. Ceriotti, “Ab initio thermodynamics of liquid and solid water,” *Proceedings of the National Academy of Sciences* **116**, 1110–1115 (2019).
- <sup>112</sup>L. Zhang, H. Wang, R. Car, and W. E, “Phase diagram of a deep potential water model,” *Phys. Rev. Lett.* **126**, 236001 (2021).
- <sup>113</sup>S. L. Bore and F. Paesani, “Realistic phase diagram of water from “first principles” data-driven quantum simulations,” *Nature Communications* **14**, 3349 (2023).
- <sup>114</sup>K. Xu, Y. Hao, T. Liang, P. Ying, J. Xu, J. Wu, and Z. Fan, “Accurate prediction of heat conductivity of water by a neuroevolution potential,” *The Journal of Chemical Physics* **158**, 204114 (2023).
- <sup>115</sup>Z. Chen, M. L. Berrens, K.-T. Chan, Z. Fan, and D. Donadio, “Thermodynamics of water and ice from a fast and scalable first-principles neuroevolution potential,” *Journal of Chemical & Engineering Data* **69**, 128–140 (2024).
- <sup>116</sup>M. L. Berrens, A. Kundu, M. F. Calegari Andrade, T. A. Pham, G. Galli, and D. Donadio, “Nuclear quantum effects on the electronic structure of water and ice,” *The Journal of Physical Chemistry Letters* **15**, 6818–6825 (2024).
- <sup>117</sup>C. Wang, W. Tian, and K. Zhou, “Ab initio simulation of liquid water without artificial high temperature,” *Journal of Chemical Theory and Computation* **20**, 8202–8213 (2024).
- <sup>118</sup>Y. Zhai, A. Caruso, S. L. Bore, Z. Luo, and F. Paesani, “A “short blanket” dilemma for a state-of-the-art neural network potential for water: Reproducing experimental properties or the physics of the underlying many-body interactions?” *The Journal of Chemical Physics* **158**, 084111 (2023).
- <sup>119</sup>V. Babin, C. Leforestier, and F. Paesani, “Development of a “first principles” water potential with flexible monomers: Dimer potential energy surface, VRT spectrum, and second virial coefficient,” *Journal of Chemical Theory and Computation* **9**, 5395–5403 (2013).
- <sup>120</sup>V. Babin, G. R. Medders, and F. Paesani, “Development of a “first principles” water potential with flexible monomers. II: Trimer potential energy surface, third virial coefficient, and small clusters,” *Journal of Chemical Theory and Computation* **10**, 1599–1607 (2014).
- <sup>121</sup>G. R. Medders, V. Babin, and F. Paesani, “Development of a “first-principles” water potential with flexible monomers. III. liquid phase properties,” *Journal of Chemical Theory and Computation* **10**, 2906–2910 (2014).
- <sup>122</sup>M. L. Huber, R. A. Perkins, A. Laesecke, D. G. Friend, J. V. Sengers, M. J. Assael, I. N. Metaxa, E. Vogel, R. Mareš, and K. Miyagawa, “New international formulation for the viscosity of H<sub>2</sub>O,” *Journal of Physical and Chemical Reference Data* **38**, 101–125 (2009).
- <sup>123</sup>R. A. Soref and C. H. Perry, “Predicted band gap of the new semiconductor SiGeSn,” *Journal of Applied Physics* **69**, 539–541 (1991).
- <sup>124</sup>S. Wirths, R. Geiger, N. von den Driesch, G. Mussler, T. Stoica, S. Mantl, Z. Ikonc, M. Luysberg, S. Chiussi, J. M. Hartmann, H. Sigg, J. Faist, D. Buca, and D. Grützmacher, “Lasing in direct-bandgap GeSn alloy grown on Si,” *Nature Photonics* **9**, 88–92 (2015).
- <sup>125</sup>J. Margetis, S. Al-Kabi, W. Du, W. Dou, Y. Zhou, T. Pham, P. Grant, S. Ghetmiri, A. Mosleh, B. Li, J. Liu, G. Sun, R. Soref, J. Tolle, M. Mortazavi, and S.-Q. Yu, “Si-Based GeSn Lasers with Wavelength Coverage of 2–3  $\mu\text{m}$  and Operating Temperatures up to 180 K,” *ACS Photonics* **5**, 827–833 (2018).
- <sup>126</sup>O. Moutanabbir, S. Assali, X. Gong, E. O’Reilly, C. A. Broderick, B. Marzban, J. Witzens, W. Du, S.-Q. Yu, A. Chelnokov, D. Buca, and D. Nam, “Monolithic infrared silicon photonics: The rise of (Si)GeSn semiconductors,” *Applied Physics Letters* **118**, 110502 (2021).
- <sup>127</sup>B. Cao, S. Chen, X. Jin, J. Liu, and T. Li, “Short-range order in GeSn alloy,” *ACS Applied Materials & Interfaces* **12**, 57245–57253 (2020).
- <sup>128</sup>X. Jin, S. Chen, and T. Li, “Short-range order in SiSn alloy enriched by second-nearest-neighbor repulsion,” *Physical Review Materials* **5**, 104606 (2021).
- <sup>129</sup>X. Jin, S. Chen, and T. Li, “Coexistence of two types of short-range order in Si–Ge–Sn medium-entropy alloys,” *Communications Materials* **3**, 66 (2022).
- <sup>130</sup>X. Jin, S. Chen, C. Lemkan, and T. Li, “Role of local atomic short-range order distribution in alloys: Why it matters in Si-Ge-Sn alloys,” *Phys. Rev. Mater.* **7**, L111601 (2023).
- <sup>131</sup>Y. Liang, S. Chen, X. Jin, D. West, S.-Q. Yu, T. Li, and S. Zhang, “Group IV topological quantum alloy and the role of short-range order: the case of Ge-rich Ge<sub>1-x</sub>Pb<sub>x</sub>,” *npj Computational Materials* **10**, 82



- (2024).
- <sup>132</sup>S. Liu, A. C. Covian, X. Wang, C. T. Cline, A. Akey, W. Dong, S. Yu, and J. Liu, “3D Nanoscale Mapping of Short-Range Order in GeSn Alloys,” *Small Methods*, 2200029 (2022).
- <sup>133</sup>J. Z. Lentz, J. C. Woicik, M. Bergschneider, R. Davis, A. Mehta, K. Cho, and P. C. McIntyre, “Local ordering in Ge/Ge–Sn semiconductor alloy core/shell nanowires revealed by extended x-ray absorption fine structure (EXAFS),” *Applied Physics Letters* **122**, 062103 (2023).
- <sup>134</sup>A. A. Corley-Wiciak, S. Chen, O. Concepción, M. H. Zoellner, D. Grützmacher, D. Buca, T. Li, G. Capellini, and D. Spirito, “Local alloy order in a  $\text{Ge}_{1-x}\text{Sn}_x/\text{Ge}$  epitaxial layer,” *Phys. Rev. Appl.* **20**, 024021 (2023).
- <sup>135</sup>R. Zhang, S. Zhao, J. Ding, Y. Chong, T. Jia, C. Ophus, M. Asta, R. O. Ritchie, and A. M. Minor, “Short-range order and its impact on the CrCoNi medium-entropy alloy,” *Nature* **581**, 283–287 (2020).
- <sup>136</sup>G. Kresse and J. Hafner, “Ab initio molecular dynamics for liquid metals,” *Phys. Rev. B* **47**, 558–561 (1993).
- <sup>137</sup>G. Kresse and J. Furthmüller, “Efficiency of ab-initio total energy calculations for metals and semiconductors using a plane-wave basis set,” *Computational Materials Science* **6**, 15–50 (1996).
- <sup>138</sup>D. M. Ceperley and B. J. Alder, “Ground State of the Electron Gas by a Stochastic Method,” *Phys. Rev. Lett.* **45**, 566–569 (1980).
- <sup>139</sup>C. Eckhardt, K. Hummer, and G. Kresse, “Indirect-to-direct gap transition in strained and unstrained  $\text{sn}_x\text{ge}_{1-x}$  alloys,” *Phys. Rev. B* **89**, 165201 (2014).
- <sup>140</sup>M. P. Polak, P. Scharoch, and R. Kudrawiec, “The electronic band structure of  $\text{Ge}_{1-x}\text{Sn}_x$  in the full composition range: Indirect, direct, and inverted gaps regimes, band offsets, and the Burstein–Moss effect,” *J. Phys. D: Appl. Phys.* **50**, 195103 (2017).
- <sup>141</sup>P. Haas, F. Tran, and P. Blaha, “Calculation of the lattice constant of solids with semilocal functionals,” *Phys. Rev. B* **79**, 085104 (2009).
- <sup>142</sup>F. Tran and P. Blaha, “Accurate Band Gaps of Semiconductors and Insulators with a Semilocal Exchange-Correlation Potential,” *Phys. Rev. Lett.* **102**, 226401 (2009).
- <sup>143</sup>H. J. Monkhorst and J. D. Pack, “Special points for Brillouin-zone integrations,” *Physical Review B* **13**, 5188 (1976).
- <sup>144</sup>X. Jin, S. Chen, and T. Li, “Enabling type I lattice-matched heterostructures in gesn alloys through engineering composition and short-range order: A first-principles perspective,” *IEEE Journal of Selected Topics in Quantum Electronics* (2024), 10.1109/JSTQE.2024.3419713.
- <sup>145</sup>S. Liu, Y. Liang, H. Zhao, N. M. Eldose, J.-H. Bae, O. Concepcion, X. Jin, S. Chen, I. Bikmukhamev, A. Akey, C. T. Cline, A. C. Covian, X. Wang, T. Li, Y. Zeng, D. Buca, S.-Q. Yu, G. J. Salamo, S. Zhang, and J. Liu, “Comparison of short-range order in gesn grown by molecular beam epitaxy and chemical vapor deposition,” (2024), arXiv:2407.02767 [cond-mat.mtrl-sci].
- <sup>146</sup>L. M. Vogl, P. Schweizer, S. Chen, X. Jin, S.-Q. Yu, D. O. Byrne, F. I. Allen, J. Liu, T. Li, and A. M. Minor, “Exploring Short-Range Ordering in Semiconducting Materials,” *Microscopy and Microanalysis* **30**, ozae044.565 (2024).
- <sup>147</sup>N. Lopanitsyna, G. Fraux, M. A. Springer, S. De, and M. Ceriotti, “Modeling high-entropy transition metal alloys with alchemical compression,” *Phys. Rev. Mater.* **7**, 045802 (2023).
- <sup>148</sup>J. Byggmästar, K. Nordlund, and F. Djurabekova, “Simple machine-learned interatomic potentials for complex alloys,” *Phys. Rev. Mater.* **6**, 083801 (2022).
- <sup>149</sup>I. Batatia, P. Benner, Y. Chiang, A. M. Elena, D. P. Kovács, J. Riebesell, X. R. Advincula, M. Asta, M. Avaylon, W. J. Baldwin, F. Berger, N. Bernstein, A. Bhowmik, S. M. Blau, V. Cărare, J. P. Darby, S. De, F. D. Pia, V. L. Deringer, R. Elijošius, Z. El-Machachi, F. Falcioni, E. Fako, A. C. Ferrari, A. Genreith-Schriever, J. George, R. E. A. Goodall, C. P. Grey, P. Grigorev, S. Han, W. Handley, H. H. Heenen, K. Hermansson, C. Holm, J. Jaafar, S. Hofmann, K. S. Jakob, H. Jung, V. Kapil, A. D. Kaplan, N. Karimitari, J. R. Kermode, N. Kroupa, J. Kullgren, M. C. Kuner, D. Kuryla, G. Liepuoniute, J. T. Margraf, I.-B. Magdău, A. Michaelides, J. H. Moore, A. A. Naik, S. P. Niblett, S. W. Norwood, N. O’Neill, C. Ortner, K. A. Persson, K. Reuter, A. S. Rosen, L. L. Schaaf, C. Schran, B. X. Shi, E. Sivonxay, T. K. Stenczel, V. Svahn, C. Sutton, T. D. Swinburne, J. Tilly, C. van der Oord, E. Varga-Umbrich, T. Vegge, M. Vondrák, Y. Wang, W. C. Witt, F. Zills, and G. Csányi, “A foundation model for atomistic materials chemistry,” (2024), arXiv:2401.00096 [physics.chem-ph].
- <sup>150</sup>X. W. Zhou, R. A. Johnson, and H. N. G. Wadley, “Misfit-energy-increasing dislocations in vapor-deposited CoFe/NiFe multilayers,” *Phys. Rev. B* **69**, 144113 (2004).
- <sup>151</sup>A. Jain, S. P. Ong, G. Hautier, W. Chen, W. D. Richards, S. Dacek, S. Cholia, D. Gunter, D. Skinner, G. Ceder, and K. A. Persson, “The Materials Project: A materials genome approach to accelerating materials innovation,” *APL Materials* **1**, 011002 (2013).
- <sup>152</sup>A. Merchant, S. Batzner, S. S. Schoenholz, M. Aykol, G. Cheon, and E. D. Cubuk, “Scaling deep learning for materials discovery,” *Nature* **624**, 80–85 (2023).
- <sup>153</sup>S. Kirklin, J. E. Saal, B. Meredig, A. Thompson, J. W. Doak, M. Aykol, S. Rühl, and C. Wolverton, “The Open Quantum Materials Database (OQMD): assessing the accuracy of DFT formation energies,” *npj Computational Materials* **1**, 15010 (2015).
- <sup>154</sup>Y. Tu, Z. Mao, and D. N. Seidman, “Phase-partitioning and site-substitution patterns of molyb-

- denum in a model Ni-Al-Mo superalloy: An atom-probe tomographic and first-principles study,” *Applied Physics Letters* **101**, 121910 (2012).
- <sup>155</sup>C. Jia, K. Ishida, and T. Nishizawa, “Partition of alloying elements between  $\gamma$ (Al),  $\gamma'$ (L12), and  $\beta$ (B2) phases in Ni-Al base systems,” *Metallurgical and Materials Transactions A* **25**, 473–485 (1994).
- <sup>156</sup>J. Yi, S. Tang, M. Xu, L. Yang, L. Wang, and L. Zeng, “A novel Al<sub>0.5</sub>CrCuNiV 3d transition metal high-entropy alloy: Phase analysis, microstructure and compressive properties,” *Journal of Alloys and Compounds* **846**, 156466 (2020).
- <sup>157</sup>G. Binnig, H. Rohrer, C. Gerber, and E. Weibel, “ $7 \times 7$  reconstruction on Si(111) resolved in real space,” *Phys. Rev. Lett.* **50**, 120–123 (1983).
- <sup>158</sup>G. Binnig, H. Rohrer, F. Salvan, C. Gerber, and A. Baro, “Revisiting the  $7 \times 7$  reconstruction of Si(111),” *Surface Science* **157**, L373–L378 (1985).
- <sup>159</sup>R. M. Tromp, R. J. Hamers, and J. E. Demuth, “Si(001) dimer structure observed with scanning tunneling microscopy,” *Phys. Rev. Lett.* **55**, 1303–1306 (1985).
- <sup>160</sup>K. D. Brommer, M. Needels, B. Larson, and J. D. Joannopoulos, “Ab initio theory of the Si(111)-( $7 \times 7$ ) surface reconstruction: A challenge for massively parallel computation,” *Phys. Rev. Lett.* **68**, 1355–1358 (1992).
- <sup>161</sup>A. P. Bartók, J. Kermode, N. Bernstein, and G. Csányi, “Machine learning a general-purpose interatomic potential for silicon,” *Phys. Rev. X* **8**, 041048 (2018).
- <sup>162</sup>L. Hu, B. Huang, and F. Liu, “Atomistic mechanism underlying the Si(111)-( $7 \times 7$ ) surface reconstruction revealed by artificial neural-network potential,” *Phys. Rev. Lett.* **126**, 176101 (2021).
- <sup>163</sup>Y. Shen, S. I. Morozov, K. Luo, Q. An, and W. A. Goddard III, “Deciphering the atomistic mechanism of Si(111)- $7 \times 7$  surface reconstruction using a machine-learning force field,” *Journal of the American Chemical Society* **145**, 20511–20520 (2023).
- <sup>164</sup>J. V. Barth, H. Brune, G. Ertl, and R. J. Behm, “Scanning tunneling microscopy observations on the reconstructed Au(111) surface: Atomic structure, long-range superstructure, rotational domains, and surface defects,” *Phys. Rev. B* **42**, 9307–9318 (1990).
- <sup>165</sup>Y. Hasegawa and P. Avouris, “Manipulation of the reconstruction of the Au(111) surface with the stm,” *Science* **258**, 1763–1765 (1992).
- <sup>166</sup>C.-M. Chan, M. A. Van Hove, W. H. Weinberg, and E. Williams, “Structural study of the reconstructed Ir(110)-(1  $\times$  2) surface by low-energy electron diffraction,” *Solid State Communications* **30**, 47–49 (1979).
- <sup>167</sup>C.-M. Chan, M. A. Van Hove, W. H. Weinberg, and E. Williams, “An r-factor analysis of several models of the reconstructed Ir(110)-(1  $\times$  2) surface a,” *Surface Science* **91**, 440–448 (1980).
- <sup>168</sup>D. Adams, H. Nielsen, M. Van Hove, and A. Ignatiev, “Leed study of the Pt(110)-(1  $\times$  2) surface,” *Surface Science* **104**, 47–62 (1981).
- <sup>169</sup>P. Li and F. Ding, “Origin of the herringbone reconstruction of au(111) surface at the atomic scale,” *Science advances* **8**, eabq2900 (2022).
- <sup>170</sup>C. Qian, D. Hedman, P. Li, S. Y. Kim, and F. Ding, “The reconstruction of Pt(001) surface and the shell-like reconstruction of the vicinal Pt(001) surfaces revealed by neural network potential,” *Small* **20**, 2404274 (2024).
- <sup>171</sup>D. Hedman, B. McLean, C. Bichara, S. Maruyama, J. A. Larsson, and F. Ding, “Dynamics of growing carbon nanotube interfaces probed by machine learning-enabled molecular simulations,” *Nature Communications* **15**, 4076 (2024).
- <sup>172</sup>K. Yeo and S. Jeong, “Machine learning insight into h-bn growth on pt(111) from atomic states,” *Applied Surface Science* **621**, 156893 (2023).
- <sup>173</sup>M. F. L. D. Volder, S. H. Tawfick, R. H. Baughman, and A. J. Hart, “Carbon nanotubes: Present and future commercial applications,” *Science* **339**, 535–539 (2013).
- <sup>174</sup>K. C. Sivaganga and T. Varughese, “Physical Properties of Carbon Nanotubes,” in *Handbook of Carbon Nanotubes*, edited by J. Abraham, S. Thomas, and N. Kalarikkal (Springer International Publishing, Cham, 2022) pp. 283–297.
- <sup>175</sup>R. Rao, D. Liptak, T. Cherukuri, B. I. Yakobson, and B. Maruyama, “In situ evidence for chirality-dependent growth rates of individual carbon nanotubes,” *Nature materials* **11**, 213–216 (2012).
- <sup>176</sup>C. Liu and H.-M. Cheng, “Controlled growth of semiconducting and metallic single-wall carbon nanotubes,” *Journal of the American Chemical Society* **138**, 6690–6698 (2016).
- <sup>177</sup>Z. Zhu, N. Wei, W. Cheng, B. Shen, S. Sun, J. Gao, Q. Wen, R. Zhang, J. Xu, Y. Wang, *et al.*, “Rate-selected growth of ultrapure semiconducting carbon nanotube arrays,” *Nature communications* **10**, 4467 (2019).
- <sup>178</sup>H. Amara and C. Bichara, “Modeling the growth of single-wall carbon nanotubes,” *Single-Walled Carbon Nanotubes: Preparation, Properties and Applications*, 1–23 (2019).
- <sup>179</sup>L. P. Ding, B. McLean, Z. Xu, X. Kong, D. Hedman, L. Qiu, A. J. Page, and F. Ding, “Why carbon nanotubes grow,” *Journal of the American Chemical Society* **144**, 5606–5613 (2022).
- <sup>180</sup>F. Ding, A. R. Harutyunyan, and B. I. Yakobson, “Dislocation theory of chirality-controlled nanotube growth,” *Proceedings of the National Academy of Sciences* **106**, 2506–2509 (2009).
- <sup>181</sup>A. J. Page, Y. Ohta, S. Irlé, and K. Morokuma, “Mechanisms of Single-Walled Carbon Nanotube Nucleation, Growth, and Healing Determined Using QM/MD Methods,” *Accounts of Chemical Research* **43**, 1375–1385 (2010).
- <sup>182</sup>L. Qiu and F. Ding, “Contact-induced phase separation of alloy catalyst to promote carbon nanotube

- growth,” *Phys. Rev. Lett.* **123**, 256101 (2019).
- <sup>183</sup>J. F. Ziegler and J. P. Biersack, “The stopping and range of ions in matter,” in *Treatise on Heavy-Ion Science: Volume 6: Astrophysics, Chemistry, and Condensed Matter*, edited by D. A. Bromley (Springer US, Boston, MA, 1985) pp. 93–129.
- <sup>184</sup>G. Wei, J. Byggmästar, J. Cui, K. Nordlund, J. Ren, and F. Djurabekova, “Revealing the critical role of vanadium in radiation damage of tungsten-based alloys,” *Acta Materialia* **274**, 119991 (2024).
- <sup>185</sup>O. El-Atwani, N. Li, M. Li, A. Devaraj, J. K. S. Baldwin, M. M. Schneider, D. Sobieraj, J. S. Wróbel, D. Nguyen-Manh, S. A. Maloy, and E. Martinez, “Outstanding radiation resistance of tungsten-based high-entropy alloys,” *Science Advances* **5**, eaav2002 (2019).
- <sup>186</sup>D. Akinwande, C. J. Brennan, J. S. Bunch, P. Egberts, J. R. Felts, H. Gao, R. Huang, J.-S. Kim, T. Li, Y. Li, *et al.*, “A review on mechanics and mechanical properties of 2D materials—Graphene and beyond,” *Extreme Mechanics Letters* **13**, 42–77 (2017).
- <sup>187</sup>B. Mortazavi, X. Zhuang, T. Rabczuk, and A. V. Shapeev, “Atomistic modeling of the mechanical properties: the rise of machine learning interatomic potentials,” *Materials Horizons* **10**, 1956–1968 (2023).
- <sup>188</sup>M. Parrinello and A. Rahman, “Strain fluctuations and elastic constants,” *The Journal of Chemical Physics* **76**, 2662–2666 (1982).
- <sup>189</sup>Y. Yang, Z. Song, G. Lu, Q. Zhang, B. Zhang, B. Ni, C. Wang, X. Li, L. Gu, X. Xie, *et al.*, “Intrinsic toughening and stable crack propagation in hexagonal boron nitride,” *Nature* **594**, 57–61 (2021).
- <sup>190</sup>L. R. Junior, M. P. Junior, W. Giazza, R. Tromer, and D. S. Galvão, “Thermal stability and fracture patterns of a recently synthesized monolayer fullerene network: A reactive molecular dynamics study,” *Chemical Physics Letters* **807**, 140075 (2022).
- <sup>191</sup>G. I. Giannopoulos, “Thermomechanical fracture of fullerene nanosheets based on reactive molecular dynamics simulations,” *Computational Materials Science* **244**, 113242 (2024).
- <sup>192</sup>G. I. Giannopoulos, S. K. Georgantzinou, and E. Ghanavloo, “Tensile behavior of fullerene nanosheets utilizing targeted reactive force fields,” *Advanced Theory and Simulations* **7**, 2400566 (2024).
- <sup>193</sup>M. Han, T. Yu, Y. Zhang, X. Chen, X.-J. Chen, Q. Peng, and H.-K. Tang, “Molecular dynamics assessment of mechanical properties of fullerene and fullerene/graphene composite,” *Journal of Composites Science* **8**, 310 (2024).
- <sup>194</sup>T. Yu, J. Li, M. Han, Y. Zhang, H. Li, Q. Peng, and H.-K. Tang, “Enhancing the mechanical stability of 2d fullerene with a graphene substrate and encapsulation,” *Nanomaterials* **13**, 1936 (2023).
- <sup>195</sup>D. Alekseev, M. Logunov, M. Lazarev, S. Zhukov, and N. Orekhov, “Thermal stability of monolayer fullerene networks: A molecular dynamics study with machine-learning potential,” *Computational Materials Science* **248**, 113572 (2025).
- <sup>196</sup>Hou, Lingxiang and Cui, Xueping and Guan, Bo and Wang, Shaozhi and Li, Ruian and Liu, Yunqi and Zhu, Daoben and Zheng, Jian, “Synthesis of a monolayer fullerene network,” *Nature* **606**, 507–510 (2022).
- <sup>197</sup>B. Peng, “Stability and strength of monolayer polymeric c60,” *Nano Letters* **23**, 652–658 (2023).
- <sup>198</sup>P. Shi, S. Feng, and Z. Xu, “Non-equilibrium nature of fracture determines the crack paths,” *Extreme Mechanics Letters* **68**, 102151 (2024).
- <sup>199</sup>P. Shi and Z. Xu, “Strength of 2d glasses explored by machine-learning force fields,” *Journal of Applied Physics* **136**, 064304 (2024).
- <sup>200</sup>G. E. Dieter and D. Bacon, *Mechanical metallurgy*, Vol. 3 (McGraw-hill New York, 1976).
- <sup>201</sup>K. Shinjo and M. Hirano, “Dynamics of friction: superlubric state,” *Surface Science* **283**, 473–478 (1993).
- <sup>202</sup>O. Hod, E. Meyer, Q. Zheng, and M. Urbakh, “Structural superlubricity and ultralow friction across the length scales,” *Nature* **563**, 485–492 (2018).
- <sup>203</sup>M. H. Müser, “Structural lubricity: Role of dimension and symmetry,” *Europhysics Letters* **66**, 97 (2004).
- <sup>204</sup>Y. Song, D. Mandelli, O. Hod, M. Urbakh, M. Ma, and Q. Zheng, “Robust microscale superlubricity in graphite/hexagonal boron nitride layered heterojunctions,” *Nature materials* **17**, 894–899 (2018).
- <sup>205</sup>A. E. Filippov, M. Dienwiebel, J. W. Frenken, J. Klafter, and M. Urbakh, “Torque and twist against superlubricity,” *Physical Review Letters* **100**, 046102 (2008).
- <sup>206</sup>I. Leven, T. Maaravi, I. Azuri, L. Kronik, and O. Hod, “Interlayer potential for graphene/h-BN heterostructures,” *Journal of chemical theory and computation* **12**, 2896–2905 (2016).
- <sup>207</sup>D. Miracle and O. Senkov, “A critical review of high entropy alloys and related concepts,” *Acta Materialia* **122**, 448–511 (2017).
- <sup>208</sup>A. S. Sharma, S. Yadav, K. Biswas, and B. Basu, “High-entropy alloys and metallic nanocomposites: Processing challenges, microstructure development and property enhancement,” *Materials Science and Engineering: R: Reports* **131**, 1–42 (2018).
- <sup>209</sup>P. Sathiyamoorthi and H. S. Kim, “High-entropy alloys with heterogeneous microstructure: Processing and mechanical properties,” *Progress in Materials Science* **123**, 100709 (2022).
- <sup>210</sup>E. Ma and C. Liu, “Chemical inhomogeneities in high-entropy alloys help mitigate the strength-ductility trade-off,” *Progress in Materials Science* **143**, 101252 (2024).
- <sup>211</sup>X. Liu, J. Zhang, and Z. Pei, “Machine learning for high-entropy alloys: Progress, challenges and opportunities,” *Progress in Materials Science* **131**, 101018 (2023).
- <sup>212</sup>C. Wen, Y. Zhang, C. Wang, D. Xue, Y. Bai, S. Antonov, L. Dai, T. Lookman, and Y. Su, “Machine learning assisted design of high entropy alloys with desired property,” *Acta Materialia* **170**, 109–117



- (2019).
- <sup>213</sup>X. Liu, Z. Long, and L. Peng, “Prediction of vickers hardness of amorphous alloys based on interpretable machine learning,” *Journal of Non-Crystalline Solids* **602**, 122095 (2023).
- <sup>214</sup>J. Li, Q. Fang, B. Liu, and Y. Liu, “Transformation induced softening and plasticity in high entropy alloys,” *Acta Materialia* **147**, 35–41 (2018).
- <sup>215</sup>Y. Wang, J. Li, J. Li, and S. Chen, “On the strain delocalization mechanism of Cu/Nb nanolayered composites with amorphous interfacial layers,” *International Journal of Plasticity* **172**, 103856 (2024).
- <sup>216</sup>S. Z. Chavoshi and S. Xu, “Nanoindentation/scratching at finite temperatures: Insights from atomistic-based modeling,” *Progress in Materials Science* **100**, 1–20 (2019).
- <sup>217</sup>A. AlMotasem, N. Daghbouj, H. Sen, S. Mirzaei, M. Callisti, and T. Polcar, “Influence of HCP/BCC interface orientation on the tribological behavior of Zr/Nb multilayer during nanoscratch: A combined experimental and atomistic study,” *Acta Materialia* **249**, 118832 (2023).
- <sup>218</sup>W. Li, S. Chen, Z. Aitken, and Y.-W. Zhang, “Shock-induced deformation and spallation in cocrfemnni high-entropy alloys at high strain-rates,” *International Journal of Plasticity* **168**, 103691 (2023).
- <sup>219</sup>N. V. Priezjev, “Fatigue failure of amorphous alloys under cyclic shear deformation,” *Computational Materials Science* **226**, 112230 (2023).
- <sup>220</sup>W.-P. Wu, Z.-J. Ding, Y.-L. Li, C. Yu, and G. Kang, “Molecular dynamics simulation of thermomechanical fatigue properties of Ni-based single crystal superalloys,” *International Journal of Fatigue* **173**, 107667 (2023).
- <sup>221</sup>S. Alvi, D. M. Jarzabek, M. G. Kohan, D. Hedman, P. Jencyk, M. M. Natile, A. Vomiero, and F. Akhtar, “Synthesis and mechanical characterization of a cumotawv high-entropy film by magnetron sputtering,” *ACS Applied Materials & Interfaces* **12**, 21070–21079 (2020).
- <sup>222</sup>P. Hirel, “Atomsk: A tool for manipulating and converting atomic data files,” *Computer Physics Communications* **197**, 212–219 (2015).
- <sup>223</sup>M. Bernetti and G. Bussi, “Pressure control using stochastic cell rescaling,” *The Journal of Chemical Physics* **153**, 114107 (2020).
- <sup>224</sup>G. Bussi, D. Donadio, and M. Parrinello, “Canonical sampling through velocity rescaling,” *The Journal of Chemical Physics* **126**, 014101 (2007).
- <sup>225</sup>D. Faken and H. Jónsson, “Systematic analysis of local atomic structure combined with 3D computer graphics,” *Computational Materials Science* **2**, 279–286 (1994).
- <sup>226</sup>A. Stukowski, “Visualization and analysis of atomistic simulation data with OVITO - the open visualization tool,” *Modelling and Simulation in Materials Science and Engineering* **18**, 015012 (2010).
- <sup>227</sup>A. Stukowski, V. V. Bulatov, and A. Arsenlis, “Automated identification and indexing of dislocations in crystal interfaces,” *Modelling and Simulation in Materials Science and Engineering* **20** (2012).
- <sup>228</sup>L. Zhao, H. Zong, X. Ding, and T. Lookman, “Anomalous dislocation core structure in shock compressed bcc high-entropy alloys,” *Acta Materialia* **209**, 116801 (2021).
- <sup>229</sup>W. Li, M. Xiang, Z. H. Aitken, S. Chen, Y. Xu, X. Yang, Q. Pei, J. Wang, X. Li, G. Vastola, H. Gao, and Y.-W. Zhang, “Unraveling the hall-petch to inverse hall-petch transition in nanocrystalline high entropy alloys under shock loading,” *International Journal of Plasticity* **178**, 104010 (2024).
- <sup>230</sup>Z. Pei, S. Zhang, Y. Lei, F. Zhang, and M. Chen, “Decoupling between shockley partials and stacking faults strengthens multiprincipal element alloys,” *Proceedings of the National Academy of Sciences* **118**, e2114167118 (2021).
- <sup>231</sup>S. Zhao, S. Yin, X. Liang, F. Cao, Q. Yu, R. Zhang, L. Dai, C. J. Ruestes, R. O. Ritchie, and A. M. Minor, “Deformation and failure of the crconi medium-entropy alloy subjected to extreme shock loading,” *Science Advances* **9**, eadf8602 (2023).
- <sup>232</sup>H. Zong, Y. Luo, X. Ding, T. Lookman, and G. J. Ackland, “hcp  $\rightarrow$   $\omega$  phase transition mechanisms in shocked zirconium: A machine learning based atomic simulation study,” *Acta Materialia* **162**, 126–135 (2019).
- <sup>233</sup>W. Li, D. Xie, D. Li, Y. Zhang, Y. Gao, and P. K. Liaw, “Mechanical behavior of high-entropy alloys,” *Progress in Materials Science* **118**, 100777 (2021).
- <sup>234</sup>Z. Yan and Y. Zhu, “Impact of lithium nonstoichiometry on ionic diffusion in tetragonal garnet-type  $\text{Li}_7\text{La}_3\text{Zr}_2\text{O}_{12}$ ,” *Chemistry of Materials* **36**, 11551–11557 (2024).
- <sup>235</sup>Z. Song, J. Han, G. Henkelman, and L. Li, “Charge-optimized electrostatic interaction atom-centered neural network algorithm,” *Journal of Chemical Theory and Computation* **20**, 2088–2097 (2024).
- <sup>236</sup>Y. Shaidu, F. Pellegrini, E. Küçükbenli, R. Lot, and S. de Gironcoli, “Incorporating long-range electrostatics in neural network potentials via variational charge equilibration from shortsighted ingredients,” *npj Computational Materials* **10**, 47 (2024).
- <sup>237</sup>C. Chen and S. P. Ong, “A universal graph deep learning interatomic potential for the periodic table,” *Nature Computational Science* **2**, 718–728 (2022).
- <sup>238</sup>B. Deng, P. Zhong, K. Jun, J. Riebesell, K. Han, C. J. Bartel, and G. Ceder, “CHGNet as a pretrained universal neural network potential for charge-informed atomistic modeling,” *Nature Machine Intelligence* **5**, 1031–1041 (2023).
- <sup>239</sup>D. Zhang, X. Liu, X. Zhang, C. Zhang, C. Cai, H. Bi, Y. Du, X. Qin, A. Peng, J. Huang, *et al.*, “Dpa-2: a large atomic model as a multi-task learner,” *npj Computational Materials* **10**, 293 (2024).



<sup>240</sup>P. Ying, C. Qian, and R. Zhao, “Support materials for ”advances in modeling complex materials: The rise of neuroevolution potentials”,” (2025).